Theoretical Study of Metal-Nitrogen Co-Doped Graphene Catalysts for Electrochemical Nitrogen Reduction Reaction

by

Weitao Shan

B.E., Huazhong University of Science and Technology, 2014

M.S., Binghamton University, SUNY, 2016

Submitted to the Graduate Faculty of the

Swanson School of Engineering in partial fulfillment

of the requirements for the degree of

Doctor of Philosophy

University of Pittsburgh
2021

UNIVERSITY OF PITTSBURGH

SWANSON SCHOOL OF ENGINEERING

This dissertation was presented

by

Weitao Shan

It was defended on

October 13, 2021

and approved by

Scott Mao, Ph.D., Professor, Department of Mechanical Engineering and Materials Science

Paul Ohodnicki, Ph.D., Associate Professor, Department of Mechanical Engineering and Materials Science

Sangyeop Lee, Ph.D., Assistant Professor, Department of Mechanical Engineering and Materials Science

Paul Leu, Ph.D., Associate Professor, Department of Industrial Engineering

Dissertation Director: **Guofeng Wang**, Ph.D., Professor, Department of Mechanical Engineering and Materials Science

Theoretical Study of Metal-Nitrogen Co-Doped Graphene Catalysts for Electrochemical Nitrogen Reduction Reaction

Weitao Shan, PhD

University of Pittsburgh, 2021

A primary challenge of electrochemically synthesizing NH_3 from N_2 is to find efficient catalysts to break inert N≡N bond under ambient conditions. Metal-nitrogen co-doped carbon (M-N-C) catalysts have exhibited encouraging performance for electrochemical nitrogen reduction reaction (NRR). Fundamental understandings related to the mechanism underlying the NRR performance on M-N-C catalysts are critically needed to further improve the activity and selectivity of these electrocatalysts.

In this study, density functional theory (DFT) calculations were performed to predict the NRR activity and selectivity of Fe-N-C, Co-N-C, and Ni-N-C catalysts. Specifically, forty-five types of MN_xC_y (M = Fe, Co, and Ni, x varies from 1 to 4, y varies from 1 to 3) moieties were modeled to relate the predicted NRR activity and selectivity with the chemical environment of active sites. The FeN_3C_1 site was predicted to have the best NRR activity and selectivity among all the sites examined. In particular, the limiting potential for NRR on the NiN_3 site was predicted to be -0.83 V, which is in good agreement with the experimentally observed optimal potential of -0.80 V for NRR on Ni-N-C catalysts. For the first time, the influence of structural distortion on the NRR catalytic performance of Fe-N-C catalysts was computationally investigated. Both the NRR activity and selectivity were found to be enhanced on compressively strained FeN_3 and FeN_4 sites. The chemical bonding analysis revealed that the stronger binding of *NNH on the strained active sites contributed to the enhanced NRR activity. Furthermore, the electrochemical stability of FeN_3 and FeN_4 sites was evaluated by computing the free energy changes of NRR intermediate species as a function of pH value and applied potential. The calculated Pourbaix diagrams were demonstrated to explain the experimentally observed optimal condition for NRR. This study produces new knowledge of the relation between chemical environment and catalytic performance of NRR active sites, the beneficial effect of structural distortion in M-N-C catalysts for NRR, and a computational approach to predict the electrochemical stability of M-N-C catalysts. Therefore, this study provides guidance to the rational design and synthesis of high-performance M-N-C catalysts for electrochemical NRR.

Table of Contents

List of Tables

List of Figures

Preface

Pursuing my Ph.D. degree at University of Pittsburgh is the most challenging and memorable experience in my life so far. This journey starts from my interests and enthusiasm for scientific research, and earning my degree puts a perfect end to it. I met mentors, friends, and partners here, and their impacts will stay with me for my entire life.

First, I would like to give my most sincere acknowledgement to my advisor Prof. Guofeng Wang. His expertise, kindness, and patient guide encourage me to move so far on my path to the Ph.D. degree. It is my fortune to have him as my academic advisor and life mentor in such an important period of my life.

I am grateful to my committee members Prof. Scott X Mao, Prof. Paul Richard Ohodnicki, Prof. Sangyeop Lee, and Prof. Paul W Leu for their insightful comments and suggestions on my research.

I would like to give my thanks to all the group members I worked with: Dr. Kexi Liu, Dr. Zhenyu Liu, Boyang Li, Siming Zhang, and Ying Fang. Their help and valuable discussions are indispensable in my study life. I also owe my thanks to all my friends I meet here, the happy time we had is unforgettable. Especially, I want to give my thanks to my girlfriend, who accompanies me every day in this period.

Finally, I want to thank my parents for their unconditional love and support for me. Their encouragement and warm care give me strength in all these years.

1.0 Introduction

The global population has been swiftly increasing for many decades which brings large demands of food and energy supply. As one of the most important chemicals in agricultural industries, ammonia (NH_3) plays a fundamental role in producing fertilizers to support more than half of the population in the world.[1, 2] Ammonia is also a great candidate for clean and sustainable energy resources as it stores 17.6% hydrogen by mass and with no CO_2 emission.[3, 4] The consumption of ammonia in fertilizer production and energy storage is very huge, thus there's no surprise the annual ammonia production reaches more than 140 million tons.[5] As shown in **Figure 1.1**, the ammonia industry includes the generation of needed energy resources and reactants, synthesis of ammonia, and the transport and consumption.[6, 7] The key part that determines ammonia production is the synthesis reaction in the ammonia reactor. The most common method used now in the ammonia production industry is still the high-cost Haber-Bosch process, which requires both high pressure (>150 atm) and high temperature (>300 °C) during the reaction.[8, 9, 10] The additional process that generates the required large quantities of H_2 for the Haber-Bosch process also consumes a huge amount of energy and generates tons of CO_2.[7, 11] Such production strategy consumes nearly 1~2% of the totally annual energy generation from fossil fuel and emits 300 metric tons of CO_2.[2, 3, 4]

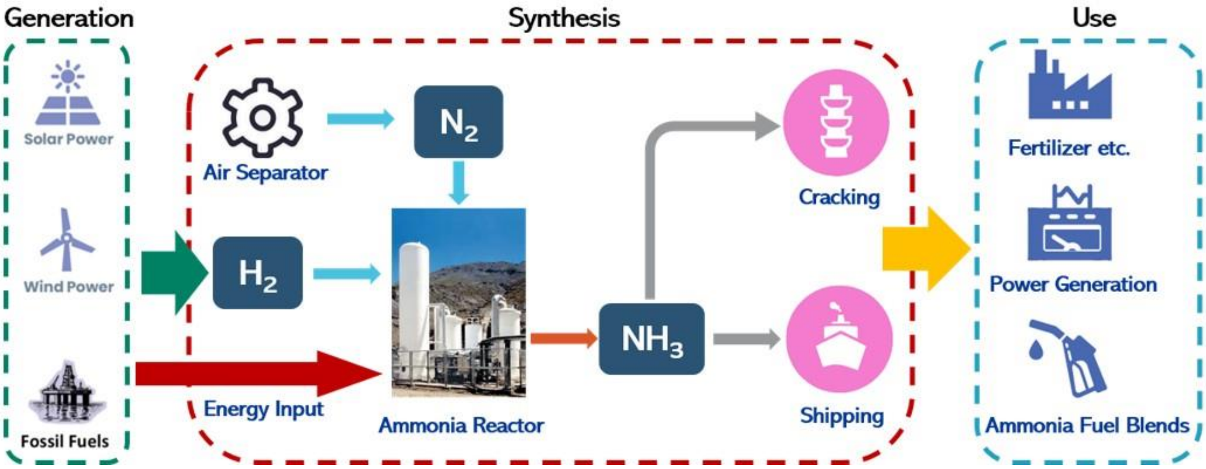

Figure 1.1. Schematic for the industrial process from power and reactants generation to usages of synthesized ammonia in modern ammonia industries.[6]

The most challenging part of fixing nitrogen and converting it to ammonia is to break the very stable triple bond between N atoms. Due to the absence of a permanent dipole, the N≡N bond is so strong that requires large energy input to activate.[12] Owing to such reason, even though the whole process of converting dinitrogen to ammonia is exergonic, harsh conditions are still necessary for activating the triple bond in the process, for which huge amounts of resources are wasted. Using catalysts are the well-known effective method for promoting the bond activation process. To date, numerous efforts have been made to search for effective low-cost methods to synthesize ammonia with clean and renewable energy sources under mild conditions.

Metal catalysts were mainly used for promoting the Haber-Bosch process, as the stepped Ru surface were acknowledged as most active metal catalyst during the process.[13, 14, 15, 16] But when taking the cost into consideration, Fe-based metal catalysts were widely used instead in ammonia industries because of the much lower price.[15] Although being catalyzed, the Haber-Bosch process still requires high temperature and pressure to occur. In fact, N_2 fixation under ambient condition with the action of enzyme nitrogenase is not a rare phenomenon in nature. However, many restrictions such as requiring 16 ATP molecules for one nitrogen molecule reduction and low reaction speed prevent its industrial application.[17, 18, 19] Molecular catalysts based on the structure and mechanism of natural nitrogenases were developed to promote the reduction of nitrogen. An early catalytic mechanism on molybdenum phosphine complex was proposed by Chatt *et al.* in seventies of last century.[20] More complex molecular catalysts such as trisamidoamine molybdenum systems was used by Yandulov and Schrock to conduct the catalytic reactions that based on proton and electron transfer to yield ammonia, which has higher production rate than natural system.[21, 22, 23] Then another molecular catalysts system shows in natural nitrogenases FeMo cofactor was proposed as dinitrogen fixation catalysts.[24]

Electrochemical methods (**Figure 1.2**) are now one of the most attractive approaches for the future industrial N_2 fixation and NH_3 production under ambient conditions. It is not only economic friendly, but also considered environment benign when acting with clean renewable energy.[25, 26, 27] Ideally the electrocatalytic reduction of N_2 to synthesize NH_3 should be similar to the hydrogen evolution reaction (HER), which is thermodynamically favored under ambient conditions with proper applied voltage.[9, 28, 29] The catalysts used in the electrochemical NRR are the key components in determining electrocatalytic activity. There are three major types of catalysts widely used now, which are noble metal catalysts, non-noble metal catalysts and polymer-complex-based or carbon-based catalysts.[30] The metal catalysts used in NRR include both noble (i.e. Au[31], Pt[32], Ru[33]) and non-noble (i.e. Fe[34], Ni[35], Cu[36]) metal, but most of them either require high reaction voltage or only have very low production rate. In addition, the usage of noble metals makes the cost of catalysts unaffordable.[9, 30, 37, 38]

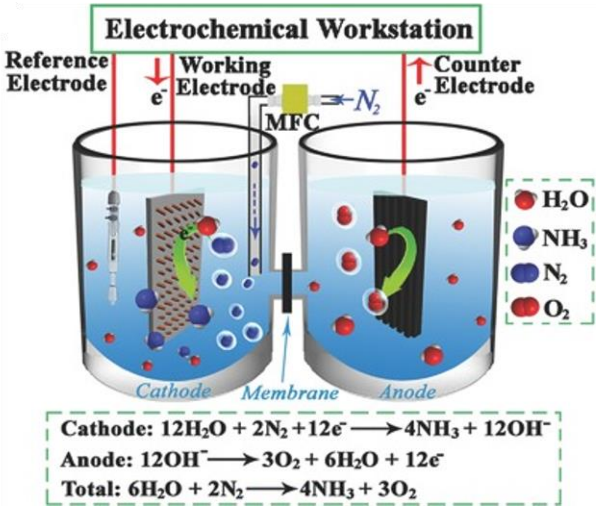

Figure 1.2. Electrochemical workstation for NRR with KOH electrolyte.[31]

Now NRR electrocatalysts based on conductive polymers or carbon membranes attracted numerous attentions because of their electronic and mechanical advances. Instead of metal-based catalysts, the conductive polymer and carbon membrane catalysts have more advances such as the higher conductivity after doping and mechanical flexibility when deposited onto the electrode.[30] The early stage of studies on the carbon-based metal-free electrochemical NRR catalysts revealed two conductive polymer catalysts based on polyaniline and polypyrrole which can be acted under ambient conditions.[39, 40] However, due to the poor stability of these two organic catalysts[39, 40], more NRR catalysts that introducing doping elements into carbon-based membrane were developed. The carbon-based catalysts, such as the metal-free catalysts that carbon-based membranes doped with N, B or P and the metal-phthalocyanine complexes catalysts with co-doped metal and N atoms, have been shown with relatively low cost and better stability.[30, 41, 42, 43, 44] Despite the advances of carbon-based catalysts, the major challenges now we facing are to improve the ammonia production rate and efficiency, as well as the reaction stability, for promoting the NRR catalytic performance on these catalysts.[2, 3, 29]

Over past decades, huge efforts and progress were made in both promoting and understanding the underlying mechanism of the catalytic performance of NRR electrocatalysts. In conjunction with experimental studies, the application of theoretical investigations with first-principles calculations has been proven as a powerful complement and fruitful strategy in many electrocatalysis studies.[45] The experimental studies so far have shown no catalyst has good enough catalytic performance to replace the Haber-Bosch method for NRR under ambient conditions.[17] Theoretical studies, especially the results from density functional theory (DFT) calculations, can help with providing a better understanding for the catalytic mechanism and catalyst design for NRR catalysts.[2, 30, 37, 38, 46] Therefore, the improvement of theoretical understandings for electrochemical NRR is urgent for the high-performance electrocatalyst design and synthesis.

In this thesis, the first-principles density functional theory calculations were conducted to investigate the NRR activity and selectivity on the metal-nitrogen co-doped graphene (M-N-C) catalysts. The relation between chemical environment and NRR activity and selectivity of active sites affects was revealed. The influence of structural distortion in M-N-C catalysts under an elevated temperature on the NRR performance was computationally investigated. A computational method was developed to predict the electrochemical stability of M-N-C catalysts for NRR. As a result, more fundamental understandings were provided for the NRR performance and further guidance for rational design of M-N-C catalysts.

2.0 Background

2.1 Nitrogen Reduction Reaction (NRR) Mechanism

In the natural nitrogen fixation process, reduction reactions occur on enzymes, which are called nitrogenases, under ambient conditions. One effective nitrogenase contains the FeMo cofactor that consists of two fused iron-sulfur clusters linked by a carbon atom with a molybdenum atom takes the apical position.[47, 48] Such natural reduction process is not efficient enough and requires a minimum of 16 ATP (adenosine triphosphate) molecules to reduce a N_2 molecule into two NH_3 molecules as shown in following

$$\mathrm{N_2 + 8H^+ + 8e^- + 16ATP \rightarrow 2NH_3 + H_2 + 16ADP + 16P_i} \tag{2.1}$$

where ADP and P_i represent adenosine diphosphate and inorganic phosphate, respectively. An equivalent of 244 kJ energy for generating one mole NH_3 molecules in the above reaction which makes it more efficient than Haber-Bosch process.[49] However, due to the generation of hydrogen shown in the above reaction as the inhibitor to the ammonia generation, normally more energy input can be expected to reach a certain NH_3 production rate.[17, 50]

In aspect of electrochemical, the general process of electrocatalytic reduction of nitrogen on the cathode can be expressed as

$$\mathrm{N_2 + 6H^+ + 6e^- \rightleftarrows 2NH_3} \tag{2.2}$$

which is a proton-electron transfer reaction, where the protons and electrons can be generated directly from water. The total energy input needed for the cleavage of triple bond between N atoms is as high as 941 $kJ \cdot mol^{-1}$ which makes whole process very difficult under ambient conditions. One should be noted that the first bond cleavage in N_2 molecule is an endergonic reaction with large energy requirement (410 $kJ\cdot mol^{-1}$), which makes the first hydrogenation step in NRR need large applied voltage to overcome the energy barrier.[9] The competing hydrogen evolution reaction (HER) that performs as the major side effect to NRR catalytic performance of catalysts is another drawback to the application of solid NRR catalysts. In the reference of reversible hydrogen electrode (RHE), the equilibrium potential of electrocatalytic NRR is comparable to HER.[9] Recent study has shown that HER can be suppressed by limiting the concentration and transfer rate of protons or electrons on the catalysts surface.[51]

Intense efforts were put into the theoretical investigations to discover the electrochemical NRR mechanisms. There are two types of possible mechanism for NRR which are associative and dissociative mechanisms. In associative mechanism, the nitrogen molecule adsorbed on the reduction active site on catalysts will be hydrogenated first, and then yield two ammonia molecules after breaking the weakened triple bond. In contrast, the nitrogen reduction occurs in dissociative mechanism will have the triple bond cleavage in prior to the hydrogenation and ammonia desorption process.

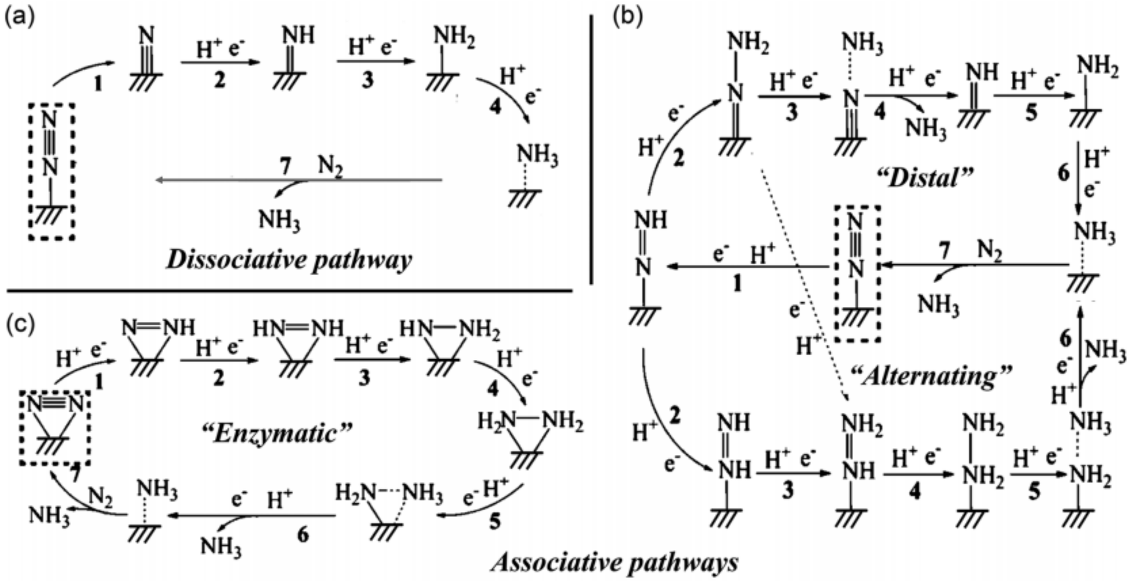

Figure 2.1. Schematic for four NRR pathways of associative and dissociative mechanisms shown as (a) dissociative, (b-c) distal, alternating and enzymatic pathways.[9, 52]

The dissociative mechanism shows in **Figure 2.1(a)** involves the triple bond between two N atoms cleavage before adsorbed on the catalytic active site. Two isolated N atoms are adsorbed on the surface and undergo hydrogenation process to yield two ammonia molecules respectively. For the NRR occurs in the Haber-Bosch process, the whole reaction was believed following a dissociative pathway.[17] There are three well-known reaction pathways for associative mechanism, which are distal, alternating and enzymatic pathways.[9, 25, 30, 53, 54] As shown in **Figure 2.1(b)**, the end-on adsorption of N_2 molecule results in two separate NRR pathways in associating mechanism due to different hydrogenation sequence. The distal[25] (upper pathway in **Figure 2.1(b)**) and alternating[53] (lower pathway in **Figure 2.1(b)**) both starts from the hydrogenated *NNH adsorption on the active site where a proton combined on the distal N atom. In distal pathway, the adsorbed N_2 molecule is simultaneously hydrogenated from the distal N atom to the proximal one. The first ammonia molecule is generated after the distal N atom reacts with three H atoms and the cleavage of triple bond, and the second ammonia molecule is desorbed from the surface of catalyst after reacting with other three H atoms. Whereas in the alternating pathway, N atoms in the adsorbed nitrogen molecule are hydrogenated alternatively before the triple bond cleavage. Before yielding ammonia molecules, a $*NH_2NH_2$ adsorption specie will be formed on the catalyst surface, and two ammonia molecules will be desorbed after two sequentially hydrogenation steps. In the enzymatic pathway (**Figure 2.1(c)**), different with above two associative pathways, the N_2 molecule is adsorbed on the catalyst surface in a side-on geometry and get hydrogenated in an alternative order for two N atoms. But not the same as the alternating pathway, the first ammonia molecule will not be desorbed until the final hydrogenation step and the second one will be released from the surface just following another N_2 adsorption.

Using the discovered mechanism shown above, studies were conducted for NRR catalytic performance of multiple catalysts candidates. In heterogeneous catalysis, one important concept is the linear relation between the activity and reaction energy of catalysts which results in a volcano curve that guides to search for new catalysts.[55, 56, 57] In the previous theoretical studies, as well as many experimental results, the volcano curve was also established that derived from linear Bronsted-Evans-Polanyi (BEP) relation for NRR catalysts.[29, 38, 46, 58, 59, 60] Such findings show that catalysts that with too strong or too weak adsorption of nitrogen on the active site will result in difficulties in desorption or dissociation step in hydrogenation process, which will lead to a weak NRR catalytic activity. The volcano plot gives a well visualized trend of performance for NRR catalysts and provides helpful guidance for effective strategy of catalysts designing.

2.2 Experimental Investigations for Electrochemical NRR

2.2.1 Experimental Reactors

Since recent decades, more and more interests were concentrated to the electrochemical reduction of nitrogen under ambient or mild conditions. One important milestone in developing NRR catalysts under ambient conditions is the synthesis of ammonia from hydrogen and nitrogen at room temperature that demonstrated by Furuya and Yoshiba twenty years ago by screening 26 types of electrode materials. They applied these electrodes in a back-to-back cell and found ZnSe as the most effective catalysts with applied potential of -1 V *vs.* RHE to reach a FE of 1.3 % and ammonia production rate of 0.23 mol·h^{-1}·m^{-2}.[61] Many pioneering experimental studies were conducted for exploring new catalysts of NRR and improving the catalytic performance. There are four major types of electrochemical reactors divided based on the different cell configurations (**Figure 2.2**).[9] The back-to-back cell (**Figure 2.2(a)**) is normally consists with solid-state electrolyte and two porous electrodes, which can be applied in a very large range of temperature (25~800 °C). The polymer electrolyte membrane type cell (**Figure 2.2(b)**) has the aqueous electrolyte filled in the anode chamber with a membrane that separate two electrode chambers. The additional reference electrode in anode chamber enables the measurement of potential of working electrode and the sufficient wetting of membrane promotes the conductivity. The H-type cell (**Figure 2.2(c)**) is made by two electrode chambers filled with liquid electrolyte and separated by Nafion membrane. As the working electrode and reference electrode were placed in the same chamber, a more accurate measurement of applied potential can be obtained. The single chamber cell (**Figure 2.2(d)**) with much easier configuration has all three electrodes in one chamber that filled with liquid electrolyte, such reactor can be operated under high pressure. However, one big problem for the single chamber cell is that the productions from cathode are likely oxidized on the anode.

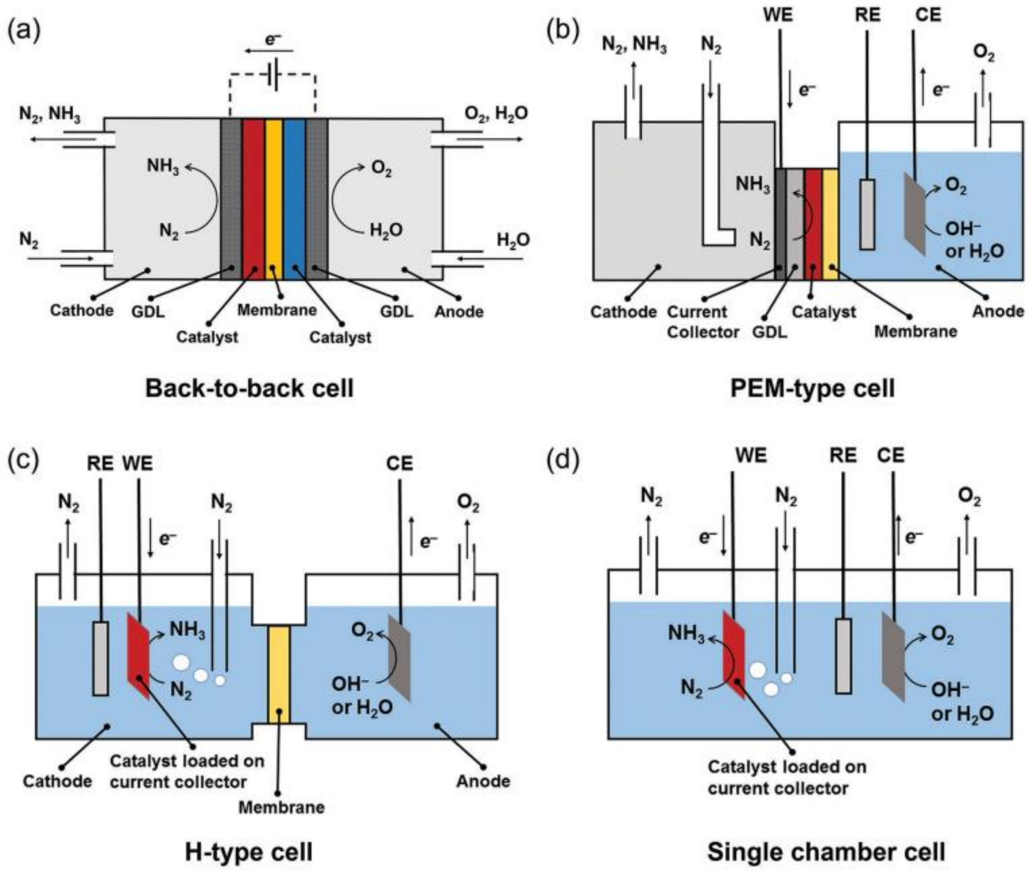

Figure 2.2. Four types of electrochemical reactors for NRR at ambient conditions.[9]

2.2.2 Electrocatalyst Materials

When considering the core component in electrosynthesis of ammonia from nitrogen, most of the efforts from previous studies were contribute to the development of catalysts. Three main types of catalysts are now widely used which are noble-metal-based catalysts, non-noble-metal-based catalysts, and conductive-polymer-complex-based catalysts.[30] For the factors that could affect catalytic activity including the particle size, morphology, crystallinity, reaction facet, active site and doping elements of catalysts.[3] Aiming to discover and design more powerful catalysts for NRR, numerous studies were conducted to investigate the factors above for all types of catalysts.

2.2.2.1 Noble Metal Catalysts

Noble metal catalysts made by well know noble materials such as Au, Pt, Ru, Rh and Pt have good conductivity and strong adsorption of reactants. Such kind of catalysts were widely used and studied in recent NRR studies under ambient conditions. For NRR occurs with employing Ru catalysts, different facets will result in performance discrepancy. The nitrogen dissociative adsorption energy barrier on flat Ru(0001) surface was determined lies in the range between 170 and 280 $kJ\cdot mol^{-1}$ depending on the surface N contents.[62] While the stepped surface of Ru was found more active than flat Ru(0001) surface as the nitrogen dissociative adsorption only has an energy barrier of 60 $kJ\cdot mol^{-1}$.[28] On both surfaces, the dissociative mechanism was found more favorable than associative mechanism.[17] Kordali et al. used a Ru cathode for NRR under relatively low temperature and pressure in a three-electrode set up with solid polymer electrolyte to obtain 0.92 % faradaic efficiency (FE) at -0.96 V applied potential and 90 °C.[33] Such study is the first one that report the electrochemical ammonia production under mild conditions. However, the problem is also obvious as the production rate was very low and the competing HER at the cathode.

Pt is one of the most commercial noble metals and widely applied in catalysts. Lan et al. used both Pt electrodes in conjunction with Nafion 211 membrane in a membrane electrode assembly to reach 0.55 % FE when applying 1.6 V electrode voltage.[32] This is the first report that electrochemically synthesis ammonia from air and water under ambient conditions. Another study done by the same group shows change the NH_4^+/H^+ Nafion membrane to $H^+/Li^+/NH_4^+$ membrane can increase the FE to 0.83 % at 1.2 V applied potential.[63] Although intense applications of Pt are already well used in many fields, the usage of Pt should be limited in electrochemical ammonia production because of the active HER.

As the most well-known noble metal, Au was also adopted as catalysts for electrocatalytic reduction of nitrogen to synthesis ammonia. Recently, a study on the tetrahexahedral Au nanorods with stepped 730 surface and composed with (210) & (310) sub-surfaces shows a high ammonia production rate of 9.68×10^{-8} $mol\cdot h^{-1}\cdot cm^{-2}$ at -0.2 V applied potential.[31] Side product $N_2H_4\cdot H_2O$ was also detected in their measurement and following theoretical investigations. The shape and crystallinity of Au nanoparticles were further studied as important factors that could affect the NRR catalytic activity. A study on amorphous Au nanoparticles on reduced graphene oxide with presence of CeO_x shows much higher FE than the crystalline Au nanoparticles on reduced graphene oxide with presence of CeO_x.[64] Another recent study that used Au sub-nanoclusters (~0.5 nm) embedded TiO_2 substrate as electrocatalyst for NRR reached a high ammonia yield rate of 21.4 $\mu g\cdot h^{-1}\cdot mg^{-1}$ and FE of 8.11 % under ambient conditions without detected N_2H_4.[65]

2.2.2.2 Non-noble Metal Catalysts

Considering the cost of noble metal, earth abundant non-noble metal elements are preferable for electrocatalysts design than noble metals. The non-noble elements, which are mostly transition metals, normally including Ti, V, Fe, Co, Ni, Cu, Mo and their oxides, chalcogenides, nitrides and carbides materials.[3, 30] Porous Ni foam and Ni wire were studied as potential electrocatalysts for NRR. The porous Ni foam was used as catalysts with aqueous electrolyte gave a FE of 0.89 % and 1.54×10^{-11} $mol\cdot s^{-1}\cdot cm^{-2}$ production rate under ambient conditions.[66] Another study from the same group on Ni wire as NRR catalysts in ethylenediamine electrolyte obtained a much higher FE of 17.2 % and ammonia production rate of 3.58×10^{-11} $mol\cdot s^{-1}\cdot cm^{-2}$ under ambient conditions.[35] Mo was studied by Wang *et al.* as electrocatalysts by comparing two oriented surface.[67] The NRR occurred on the (110)-oriented surface of Mo nanofilm presented a higher FE of 0.72 % with ammonia production rate of 3.09×10^{-11} $mol\cdot s^{-1}\cdot cm^{-2}$ at -0.49 V applied potential.

Though most previous studies on transition-metal-based catalysts discovered poor catalytic activity, many efforts were made on compounds complexes to obtain better performance. A systematic study was conducted by Furuya *et al.* to investigate the catalytic performance of several non-noble-metal-based catalysts.[61] The current efficiency and ammonia production rate were compared under ambient conditions with -1.0 V applied potential. Among their candidates, the metal chalcogenides and borides (ZeSe, TiB_2, ZnS, NiS, CdS and CuS) exhibits better catalytic activity comparing to other metal and metal oxide catalysts (PbO-TiO_2, Sb-SbO_2 and ZnO). However, some important factors such as shape and active site density were not specified in the discussion, more efforts are needed for detailed investigation. Some studies conducted on the oxides, nitrides and chalcogenides on Mo (MoO_3, MoN and MoS_2) has shown different activity trends among these three types of compounds which indicates the performance comparison excluding other extrinsic and intrinsic factors is not very meaningful.[68, 69, 70] Similar to the noble-metal-based catalysts, better performance can also be expected on amorphous non-noble-metal-based catalysts. A study on the $Bi_4V_2O_{11}/CeO_2$ as electrocatalysts for NRR found the amorphous one has much better catalytic activity than the one with crystalline structure.[71]

2.2.2.3 Carbon-based Catalysts

As a promising alternative to the noble-metal and non-noble meta catalysts, electrocatalysts that based on conductive polymers and carbon membranes not only have much lower cost, but also very stable and flexible. Two types of conductive polymers, which are polyaniline and polypyrrole, were investigated as metal-free electrocatalysts that based on conductive polymer complex, but they both have stability problem when operating under ambient conditions.[39, 40] For instance, the first metal-free catalysts that reported for electrocatalytic synthesis of ammonia from nitrogen was conducted in a single chamber cell with polyaniline film coated on Pt plate as working electrode.[39] Under mild conditions, the production rate was 2.25×10^{-7} $mol\cdot h^{-1}\cdot cm^{-2}$ at -0.12 V *vs.* NHE but with 16 % current efficiency only for 5 hours and then decreased to 7 %. As nearly no positive result has been reported previously on pure carbon-based materials, such as graphene, introducing co-doping heteroatoms is adopted to improve the stability and efficiency of metal-free NRR electrocatalysts. Recently N-doped graphene membrane materials play a very attractive role in NRR electrochemical synthesis.[72, 73, 74] Carbon-based membrane with nitrogen doping that synthesized from pyrolyzing the zeolite imidazolate framework (ZIF) under 750 °C was found has higher ammonia production rate of 0.84 $\mu mol\cdot cm^{-2}\cdot h^{-1}$ than many metal-based catalysts.[74] Another study that also conducted on the N-doped porous carbon-based membrane found that KOH electrolyte can promote the efficiency as less competing HER occurring comparing to the HCl electrolyte.[73] Besides doping N atoms in carbon membrane, the introducing of other heteroatoms (*e.g.* B, S, P) was also studied. A recent study reported using N,P co-doped hierarchical porous carbon as electrocatalyst for NRR under ambient conditions which results in a FE of 4.2 % and ammonia production rate of 0.97 $\mu g\cdot h^{-1}\cdot mg^{-1}$ in aqueous electrolyte.[27]

Another kind of carbon-based catalyst is the transition metal and nitrogen co-doped carbon catalysts (M-N-C). The study on Fe-phthalocyanine catalysts show that such metal-phthalocyanine complex has a FE of 0.35 % and production rate of 5.57×10^{-10} mol·s^{-1}·cm^{-2} but only last for very short period.[75] A systematic study on the metal-phthalocyanine catalysts by the same group show the best candidate was Sn-phthalocyanine, but the stability is still problematic.[76] Another study on Fe-N co-doped membrane revealed a more efficient catalyst with 34.83 μg·h^{-1}·mg^{-1} production rate and 9.28 % FE at -0.2 V applied potential, and the primary active site configuration was discovered to be FeN_3.[77] A recording high production rate of 120.9 μg· h^{-1}·mg^{-1} with 29.6 % FE of electrocatalytic NRR was reported by using a Ru single atom nitrogen-doped carbon.[78] Later another study on Ru single site at porous N-doped carbon catalysts was reported to reach a stable ammonia production rate as high as 3.665 mg· h^{-1}·mg$_{Ru}^{-1}$ at -0.21 V applied electrode potential under ambient conditions.[79] The addition of ZrO_2 was also found be able to suppress the competing HER in electrocatalytic reduction, thus can promote the FE to 21% at -0.11 V with low overpotential of 0.17 V. A previous study on Ni-N-C catalysts for NRR showed a high faradaic efficiency (FE) of 21 ± 1.9 %, and NH_3 production rate of $115\,\mu g\cdot h^{-1}\cdot cm^{-2}$ under ambient conditions.[80] A very recent study on the tetraphenylporphyrin iron chloride (FeTPPCl) showed a promising NRR activity with FE of 16.76 ± 0.9 % and NH_3 production rate of $18.28\ \pm 1.6\,\mu g\cdot h^{-1}\cdot mg_{cat.}^{-1}$ in neutral electrolytes.[81] Zhang et al. showed a high-active iron porphyrin-based catalysts (Fe-TCPP) with $44.77\,\mu g\cdot h^{-1}\cdot mg_{cat.}^{-1}$ NH_3 production rate and 16.23 % FE.[82] A rational designed and synthesized single iron and N,O-doped carbon (Fe-NO-C) catalysts was studied by Hou *et al*..[83] Their catalysts reached a high NH_3 production rate of $31.9\,\mu g\cdot h^{-1}\cdot mg_{cat.}^{-1}$ and FE of 11.8 %.

Table 2.1. Summary of electrocatalytic systems used for NRR in previous studies.

Electrocatalyst	Electrolyte	Conditions	NH_3 yield	FE
ZnSe[61]	KOH	-1 V *vs.* RHE	0.23 $mol\cdot h^{-1}\cdot m^{-2}$	1.3
Pt/C[32]	Solid state electrolyte	-1.6 V *vs.* RHE	4.1×10^{-6} $mol\cdot h^{-1}\cdot cm^{-2}$	0.55
THH Au nanorod[31]	KOH	-0.2 V *vs.* RHE	9.68×10^{-8} $mol\cdot h^{-1}\cdot cm^{-2}$	4.0
PANI@Pt[39]	Methanol/$LiClO_4$/H_2SO_4	-0.12 V *vs.* NHE	2.25×10^{-7} $mol\cdot h^{-1}\cdot cm^{-2}$	16
Ni wire[35]	Ethylenediamine	-1.8 V *vs.* RHE	3.58×10^{-11} $mol\cdot s^{-1}\cdot cm^{-2}$	17.2
O-MoC@NC[84]	HCl+Li_2SO_4	-0.35 V *vs.* RHE	22.5 $\mu g\cdot h^{-1}\cdot mg^{-1}$	25.1
$Bi_4V_2O_{11}/CeO_2$[71]	HCl	-0.2 V *vs.* RHE	23.21 $\mu g\cdot h^{-1}\cdot mg^{-1}$	10.16
NCM[85]	HCl	-0.3 V, -0.2 V	0.08 $g\cdot h^{-1}\cdot m^{-2}$	5.2
Au_NPs@NCM[85]	HCl	-0.2 V, -0.1 V	0.36 $g\cdot h^{-1}\cdot m^{-2}$	22
Au@TiO_2[65]	HCl	-0.2 V *vs.* RHE	21.4 $\mu g\cdot h^{-1}\cdot mg^{-1}$	8.11
B-doped graphene[86]	H_2SO_4	-0.5 V *vs.* RHE	1.6×10^{-10} $mol\cdot s^{-1}\cdot cm^{-2}$	10.8
B-N/C[87]	HCl	-0.3 V *vs.* RHE	7.75 $\mu g\cdot h^{-1}\cdot mg^{-1}$	13.79
S-doped graphene[88]	HCl	-0.6 V, -0.5 V	27.3 $\mu g\cdot h^{-1}\cdot mg^{-1}$	11.5
NPC[27]	HCl	-0.2 V *vs.* RHE	0.97 $\mu g\cdot h^{-1}\cdot mg^{-1}$	4.2
NPC[74]	H_2SO_4	-0.9 V *vs.* RHE	1.40 $mmol\cdot h^{-1}\cdot g^{-1}$	1.42
NP-C-MOF-5[43]	HCl	-0.1 V *vs.* RHE	1.08 $\mu g\cdot h^{-1}\cdot mg^{-1}$	0.08
Fe-N/C-CNT[77]	KOH	-0.2 V *vs.* RHE	34.83 $\mu g\cdot h^{-1}\cdot mg^{-1}$	9.28
Ru SAs/N-C[78]	H_2SO_4	-0.2 V *vs.* RHE	120.9 $\mu g\cdot h^{-1}\cdot mg^{-1}$	29.6
Ru/NC[79]	HCl	-0.21 V *vs.* RHE	3.66 $mg\cdot h^{-1}\cdot mg_{Ru}^{-1}$	
Ru@ZrO_2/NC[79]	HCl	-0.11 V *vs.* RHE		21
BiNC[89]	K_2SO_4	-0.6 V *vs.* RHE	200 $mmol\cdot h^{-1}\cdot g^{-1}$	66

2.3 Theoretical Investigations for Electrocatalytic NRR

The rapid development of computer technology leads to a wide application of computational methods as a powerful complement to experimental investigations. With the help of theoretical investigations, one can more efficiently interpret experimental phenomenon and mechanisms, explore and design new catalysts.[9] Recent years, many first-principles studies have been conducted on mechanism investigation and activity trend prediction. Most of them are concentrated on the energy evolution that based on intermediates adsorption, and the suppression of competing side effects on the reaction surface which are related to the most two fundamental challenges in promoting the performance of NRR electrocatalysts.[29, 90]

2.3.1 DFT Studies of NRR on Pure Metal Catalysts

The first-principles methods, especially the density functional theory (DFT) calculations, are very useful when applied for materials screening. A remarkable study that previously done by Logadottir *et al.* using the DFT calculations investigated the NRR performance on several transition metal surfaces.[60] A linear relationship was revealed between the activation energy for N_2 dissociation and the adsorption energy of atomic nitrogen on the surface. Furthermore, a landmark work was reported by Skularson *et al.* in 2012 as they used the first-principles methods to analyze the possibility of electrochemically formation of ammonia on multiple pure transition metal surfaces.[38] Firstly, for NRR on Ru(0001) surface, which was considered as most active catalyst, the distal pathway was found more favored than the alternating pathway and the applied potential needs to be -1.08 V to tune the whole reduction process thermodynamically favored.

Regarding the associative mechanism of NRR on the stepped surface of Ru, the distal pathway is also favored on stepped surface with lower limiting potential of -0.43 V. They further investigated the adsorption of different intermediate species on other metal surfaces, and then concluded a volcano plot (**Figure 2.3(a)**) for ammonia formation on the catalysts that can be used to predict the catalytic activity against the adsorption energy of dissociated N atom. The two determining steps that key to the catalytic activity were identified as the first hydrogenation step of adsorbed N_2 molecule and the last hydrogenation step for adsorbed $*NH_2$ fragment. As indicated in the volcano plot, too strong binding of N_2 results in difficulty on the last hydrogenation and desorption step, while too weak binding of N_2 leads to difficulty on the first hydrogenation step and nitrogen bond breaking. The linear relationship that between the adsorption of H atom and N atom on the catalysts surface (**Figure 2.3(b)**) can also be used for the selectivity prediction for NRR. Their remarkable study motivated more following efforts on using DFT calculations as helpful tool or complement for new catalysts screening and mechanism exploring.

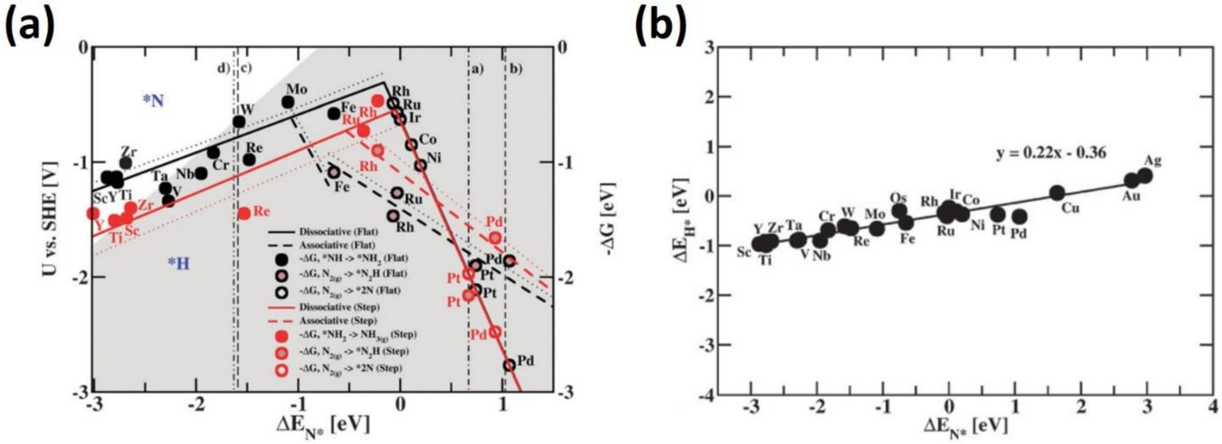

Figure 2.3. (a) Volcano diagram (solid lines) for NRR on both flat (black) and stepped (red) surfaces of transition metals. The stabilization effect from hydrogen bonding on different species was also included (dotted lines). (b) The adsorption energy of H atom on transition metal surfaces against the adsorption energy of dissociated N atom.[38]

Another study was conducted to quantitatively demonstrate that the rate limiting steps in NRR on transition metal surfaces were in the linear relation with the energy of two key species hydrogenation, which are the hydrogenation of the adsorbed N_2 molecule and the adsorbed $*NH_2$ fragment.[29] As shown in **Figure 2.4**, except the very active Re surface that was limited by the reduction step from *NH to $*NH_2$, potential determining steps for other transition metal surfaces are both the first hydrogenation step of adsorbed N_2 molecule and the last hydrogenation step for adsorbed $*NH_2$ fragment. Their findings confirmed the previous study[38] and show that the adsorption and hydrogenation of key species can be the limitation of NRR on transition metal surface. They also considered the competing HER on these transition metal surfaces and found that none of their candidates show a difference that less than 0.4 eV between the limiting potential of NRR and HER, for which the NRR could be hindered by HER.

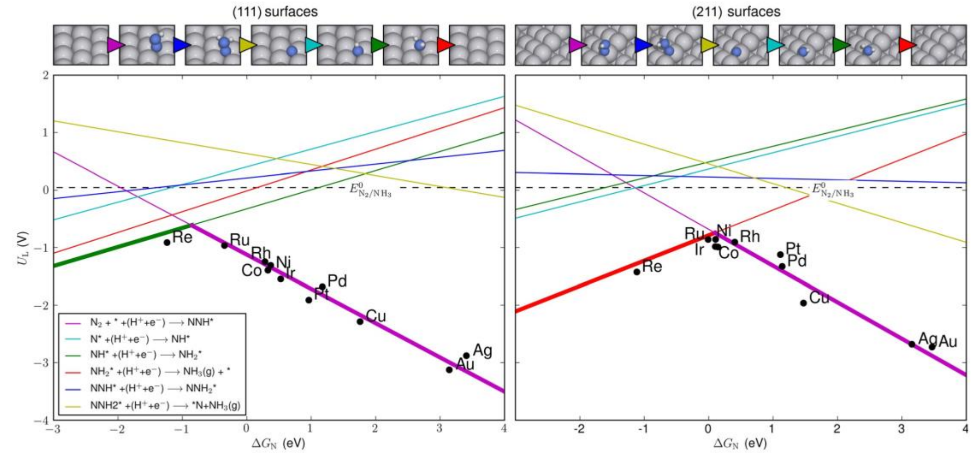

Figure 2.4. The volcano plot of limiting potential as a function of adsorption energy of dissociated N atom on the surface of transition metals. The schematic of reduction reaction pathway on different surface is shown above each subplot.[29]

Computational methods were also used to explore the approaches to improve the selectivity of pure metal catalysts. As already suggested in an early study, restricting the ability of protons and electrons to reach the surface of electrocatalysts can effectively hinder the competing HER.[51] A theoretical study show that use the 2,6-lutidinium as the non-aqueous proton donor for NRR would lead to a suppressed HER on Pt(111) surface.[91] The protons provided by $LutH^+$ was found difficult to for a *H adsorption on the Pt surface as such process holds a very high energy barrier. Thus, the subsequent reaction leads to the production of hydrogen molecules are also hindered. Another computational study from the same group also suggested the usage of non-aqueous electrolyte for selective NRR from a more general kinetic view.[92] They also found that the change from associative to dissociative mechanism for electrochemical NRR on transition metal surfaces can improve the NRR activity and selectivity.

2.3.2 DFT studies of NRR on Metal-Nitrogen Co-Doped Graphene Catalysts

Many theoretical studies were also conducted on carbon-based catalysts for NRR, especially on the transition metal and nitrogen co-doped graphene catalysts (M-N-C). Since the M-N-C model was already well studied in oxygen reduction reaction (ORR),[93, 94, 95, 96, 97, 98] it is reasonable to explore its potential application on NRR. For example, the FeN_4 sites were well studied by many studies as the NRR active sites.[77, 99, 100] Besides the widely studied MN_4 sites that commonly discussed, different cases of chemical coordination in active sites in M-N-C catalysts were also investigated. A study conducted by Li *et al.* proposed a FeN_3 embedded graphene as potential catalysts for NRR under ambient conditions.[52] Their theoretical study show that the high-spin-polarized FeN_3 moiety promoted the adsorption of nitrogen molecules and activated the triple bond between N atoms. The Ru single-atom catalysts that contains RuN_3 and RuN_1 sites were also proposed by Zeng *et al.* and Sun *et al.* as the potential NRR electrocatalysts, respectively.[78, 79] Another theoretical study by Yang *et al.* proposed a novel aspect for NRR mechanism on SAC catalysts.[101] In their investigations, the active site will firstly be saturated by capturing as many as possible nitrogen molecules to suppress the competing HER. The MoN_3 and CrN_3 active sites embedded graphene layers were identified as very promising catalysts that with low overpotential and high selectivity.

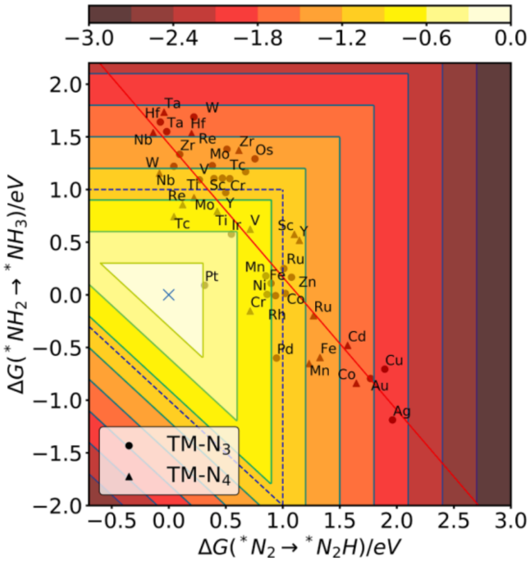

Figure 2.5. 2-D volcanic plot of NRR limiting potential determined by the free energy change of two key hydrogenation steps on various MN_3 and MN_4 active sites. The doped central metal atom is mark for each site.[102]

A systematic study from Jung *et al.* was conducted on the single atom catalysts that formed by different doped central transition metals, and also with different chemical coordination.[90] They investigated four different chemical environmental conditions for central doped transition metals which are the MN_4, MN_3, MC_4 and MC_3, with several transition metal candidates, there are total

120 different SAC structures. The TiN_4 and VN_4 were defined as the promising candidates for NRR under ambient conditions with good NRR activity and selectivity. Their further electronic investigations show the positive charged central metal not only promoted the N_2 adsorption, but also provided enough suppression of competing HER. Another more detailed study on coordination environment of doped central transition metal was done on FeN_x ($x = 0 \sim 4$) active sites for NRR.[103] It was shown that the chemical coordination around central transition metal is very important for the catalytic activity of SAC catalysts. In their findings, the doped Fe with two coordinated N atoms located at opposite doping sites show best reaction activity and selectivity for NRR. A recent screening study for NRR on MN_3 and MN_4 sites revealed the linear correlations between the NRR activity and the adsorption strength of two key intermediate species.[102] Their 2-D volcano plot (**Figure 2.5**) indicates a negative relation between two key hydrogenation steps, which are $*N_2 \rightarrow *NNH$ and $*NH_2 \rightarrow *NH_3$, indicating a restriction for improving the NRR activity on the M-N-C catalysts. An active catalyst for electrochemical NRR need to have a strong adsorption of *NNH and a weak adsorption of $*NH_2$ at the same time which was proved impossible. Their predictions indicate the VN_4 site exhibit the best NRR performance and active site stability. Moreover, theoretical predictions were also made recently for NRR on catalysts metal dimers embedded in nitrogen doped carbon.[104] Among all the studied twelve combinations of metal dimer active sites, the binary FeRh was found to have a superior NRR activity with a limiting potential of -0.22 V, which is even better than the current most active stepped Ru(0001) surface. There are also many theoretical screening studies for carbon based NRR catalysts,[100, 105, 106, 107] which all provided either a better understanding for the mechanism of NRR performance on the catalysts, or a good guidance for better strategy to synthesizing high-performance NRR catalysts.

3.0 Hypotheses

In this thesis, the following hypotheses are proposed:

1. *The number of doped N atoms in the* MN_xC_y *(M = Fe, Co, and Ni, x varies from 1 to 4, y varies from 1 to 3) active site are important for its NRR catalytic performance.* Active sites with different numbers of doped N atoms would have impact on the stability of active sites and the electronic distribution on the central metal atoms. Consequently, the binding strength of intermediate species would be changed, and the NRR activity and selectivity would be affected.
2. *The type of central metal atom plays a significant role in determining the NRR activity and selectivity of M-N-C catalysts.* The unique electron configuration of the central metal atom would have significant impact to the formed chemical bonds with adsorbed intermediate species. A proper degree of bonding strength of intermediate species plays a primary role for NRR activity and selectivity.
3. *The compressive strain in structurally distorted* MN_xC_y *active sites would enhance the NRR activity and selectivity.* The graphene layer under elevated temperature exhibits a non-planar configuration which would result in a distorted active site configuration. The binding strength of intermediate species on the distorted active site would also be changed, which is critical for determining the NRR activity and selectivity on the MN_xC_y site.
4. *The enhanced binding of intermediate species on strained active sites is attributed to the modified electronic structure on the active sites.* The distorted configuration and shortened metal-nitrogen bond would result in a modified electronic structure on the active site.

Therefore, the chemical bond formation between the adsorbed species and central metal atom would also be changed.

5. *The electrochemical stability of M-N-C catalysts for NRR could be predicted via computational methods.* With the implemented implicit solvation model in DFT calculations, the relative electrochemical stability of NRR intermediate species could be predicted by free energy change calculations. The free energy would be calculated as a function of pH value and applied potential, which would be used to generate the Pourbaix diagram to predict the stability of intermediate species. The predicted Pourbaix diagram would be compared with experimental observations of optimal conditions for NRR to validate such computational method.

4.0 Objectives

To examine all the listed hypotheses, a systematic computational study is needed for NRR on the M-N-C catalysts. Specifically, the following objects are accomplished:

1. Investigate all fourty-five possible MN_xC_y active site structures for Fe-N-C, Co-N-C, and Ni-N-C catalysts. Calculate the free energy changes of NRR and HER intermediate species to obtain the free energy evolution profile for all relatively stable MN_xC_y sites.
2. Analyze the results of calculated electron distribution and free energy change of NRR intermediate species to relate the chemical environment of active sites to the NRR activity and selectivity.
3. Investigate the effect of structural distortion on compressively strained FeN_3 and FeN_4 site models. Calculate the free energy evolutions for NRR and HER on both unstrained and strained active sites to exhibit the changes in NRR activity and selectivity of strained active sites.
4. Analyze the change of electronic distribution on the strained active sites. Analyze the change of the chemical bond formation for *NNH and *H adsorption on the strained active sites compared to on unstrained ones.
5. Calculate the free energy changes for NRR intermediate species as a function of pH and applied potential using the implicit solvation model and constant potential method.
6. Use the calculated Pourbaix diagram to explain the optimal electrolyte pH and electrode potential observed in experiments and predict the electrochemical stability of MN_xC_y sites.

5.0 Computational Methods

5.1 Density Functional Theory

In solid state physics, many approaches were developed to obtain the ground state properties of materials by solving the time-independent Schrödinger equation $\hat{\mathrm{H}}\Psi = E\Psi$. In the Born-Oppenheimer approximation[108], the nuclei are treated as fixed as the mass of a nucleus is about two thousand times of the mass of an electron. Thus, the kinetic energy term of nuclei in the Schrödinger equation is neglected and the potential energy term of nuclei is merely a constant. Then the electronic Hamiltonian for the case of N electrons interact with M nuclei can be expressed as follow:

$$\hat{\mathrm{H}}_{electron} = \left[-\frac{\hbar^2}{2m_e}\sum_{i=1}^{N}\nabla_i^2 - \frac{1}{4\pi\varepsilon_0}\sum_{i=1}^{N}\sum_{A=1}^{M}\frac{Z_A e^2}{\left|\vec{r}_i - \vec{R}_A\right|} + \frac{1}{8\pi\varepsilon_0}\sum_{i=1}^{N}\sum_{j=1}^{N}\frac{e^2}{\left|\vec{r}_i - \vec{r}_j\right|} \right] \tag{5.1}$$

where $-\frac{\hbar^2}{2m_e}\sum_{i=1}^{N}\nabla_i^2$ term represents the kinetic energy of electrons, $-\frac{1}{4\pi\varepsilon_0}\sum_{i=1}^{N}\sum_{A=1}^{M}\frac{Z_A e^2}{|\vec{r}_i-\vec{R}_A|}$ is the potential energy of nuclei-electron interaction, and $\frac{1}{8\pi\varepsilon_0}\sum_{i=1}^{N}\sum_{j=1}^{N}\frac{e^2}{|\vec{r}_i-\vec{r}_j|}$ is the potential energy of electron-electron interaction. The solution of the Schrödinger equation with this electronic Hamiltonian is the wavefunction ψ and electronic energy E. However, solving the above equation for all electrons is unaffordable.

The density functional theory (DFT) [109, 110, 111] was proposed by Hohenberg, Kohn and Sham in 1964 and 1965[109, 110] to simplify the many-body problem. Since established, DFT has been proved to be an efficient and the most successful method to computationally describe the ground state properties of a wide range of materials. DFT stands on two fundamental theorems: (1) the ground state energy from the Schrödinger equation is a unique functional of the ground state electron density; (2) the electron density that minimizes the energy of the overall functional is the true electron density corresponding to the full solution of the Schrödinger equation. Such theorems are valid in any system. In such theory, the interaction between electrons is assumed as the effect of one electron on the average density of all electrons. Therefore, the many-body problem is simplified to be a one-body problem. The Kohn-Sham equation based on the electron density $n(\vec{r})$ can be expressed as:

$$\varepsilon_i \psi_i(\vec{r}) = \left[-\frac{\hbar^2}{2m_e} \nabla^2 + V(\vec{r}) + V_H(\vec{r}) + V_{XC}(\vec{r}) \right] \psi_i(\vec{r}) \tag{5.2}$$

where $-\frac{\hbar^2}{2m_e}\nabla^2$ is the electron kinetic energy term, $V(\vec{r})$ is the Coulomb potential between an electron and nuclei, $V_H(\vec{r})$ is the Hartree potential between an electron and the electron density by other electrons which can be calculated as $e^2 \int \frac{n(\vec{r}')}{|\vec{r}-\vec{r}'|} d^3\vec{r}'$. $V_{XC}(\vec{r})$ is the exchange-correlation potential which can be calculated as the functional derivative of E_{XC} with respect to $n(\vec{r})$, i.e., $V_{XC}(\vec{r}) = \frac{\delta E_{XC}}{\delta n(\vec{r})}$. The electron density $n(\vec{r})$ used in the Kohn-Sham is derived as $n(\vec{r}) = \sum_{i=1}^{N} |\psi_i(\vec{r})|^2$, in which $\psi_i(\vec{r})$ is the wavefunction of i-th electron.

For the Kohn-Sham energy partition $E_{[n(\vec{r})]}$, which is the combination of the known part and unknown part. The known part is the summation of the electron kinetic energy, the Coulomb potential between electrons and nuclei, and the Hartree potential between an electron and the electron density. The unknown part is the exchange-correlation energy E_{XC}. If the exact exchange-correlation energy can be calculated, the exact energy can be obtained using the Kohn-Sham equation. However, the exchange-correlation energy is too complex to directly derive its formula.

To obtain a reliable value of the exchange-correlation energy, several approximation functionals were developed. The first and simplest one is the local density approximation (LDA)[110, 112, 113], in which the exchange-correlation energy is set at each position to be the known exchange-correlation potential from the uniform electron gas with the $n(\vec{r})$ at that position, i.e.,

$$V_{XC}(\vec{r}) = V_{XC}[n(\vec{r})] \tag{5.3}$$

Consequently, the exchange energy is now a functional of the electron density:

$$E_X^{LDA}[n(\vec{r})] = -\frac{3}{4}\left(\frac{3}{\pi}\right)^{\frac{1}{3}} \int n\left(\vec{r}^{\frac{4}{3}}\right) d\vec{r} \tag{5.4}$$

and the correlation energy E_C^{LDA} is parametrized from the quantum Monte Carlo simulations[114]. Though the theory basis of LDA is quite simple, it surprisingly works well when predicting the lattice parameter in metallic systems. However, LDA often overestimates the cohesive energy in molecules and crystals. The second one is the generalized gradient approximation (GGA)[115] which has a similar form as LDA but complicated the formula of exchange-correlation potential to have both the electron density $n(\vec{r})$ and the gradient of electron density $\nabla n(\vec{r})$.

$$V_{XC}(\vec{r}) = V_{XC}[n(\vec{r}), \nabla n(\vec{r})\ ] \tag{5.5}$$

Various forms of GGA were proposed, including Becke-Lee-Yang-Parr (BLYP)[116, 117], Perdew-Wang 91 (PW91)[115, 118], Perdew-Burke-Ernzerhof (PBE)[119], and Perdew-Burke-Ernzerhof revised for solids (PBEsol)[120]. GGA is more accurate than LDA in energy calculations as it considers the inhomogeneous effects in electron density. It should be noted that both LDA and GGA always underestimate the bandgap of semiconductors and insulators.

A self-consistent approach is needed when solving the Kohn-Sham equation with uncertain electron density. First, an initial trial electron density $n(\vec{r})$ is defined by an initial stochastic value. Then the Kohn-Sham equation will be solved to obtain a new wavefunction $\psi_i(\vec{r})$ based on this initial electron density. Subsequently, a new electron density can be refined using the calculated wavefunction $\psi_i(\vec{r})$:

$$n_{KS}(\vec{r}) = \int \psi\psi^* dv \tag{5.6}$$

If the obtained $n_{KS}(\vec{r})$ is close enough to the previous $n(\vec{r})$, calculations are considered converged. Otherwise, the new $n_{KS}(\vec{r})$ will be used to solve the Kohn-Sham equation again to repeat the self-consistent approach until reach convergency.

In this work, all the spin-polarized DFT[109, 110, 111] calculations were performed using Vienna Ab Initio Simulation package (VASP)[121, 122, 123, 124]. The Perdew-Burke-Ernzerhof (PBE)[119] generalized gradient approximation (GGA)[115] was used in our calculations to estimate the exchange-correlation functionals. The projector augmented wave (PAW)[125] pseudopotential was employed to describe the core electrons. A plane wave basis set with a kinetic energy cutoff of 400 eV was used to expand the wave functions. The energy convergence of geometry optimization was set to be 1×10^{-5} eV. The atomic structures used in DFT calculations were allowed to relax to the tolerance of atomic force at 0.01 eV/Å. The van der Waals correction was included using the Tkatchenko-Scheffler method.[126, 127]

In the DFT calculations, the fully embedded sites of M-N-C catalyst models were simulated by a 9.84×8.52 Å periodic unit cell in a graphene layer. There are two types of fully embedded site, one is the metal atom in a single-vacancy site coordinated with three atoms and the other one is the metal atom in a double-vacancy site coordinated with four atoms. Both types of fully embedded active sites have the same size of modelling unit cell. The edge-to-edge sites of M-N-C catalyst models were simulated by bridging two N atoms doped graphene edges by the central transition metal atom. The unit cell used in the edge-to-edge site model was built with the size of

9.84×12.79 Å. A space of 14 Å vacuum space was added perpendicular to the surface of all simulation models to avoid the interaction between periodic images. The Brillouin zone for the fully embedded site model was sampled by a 4×4×1 Monkhorst-Pack grid[128]. The Brillouin zone used for the edge-to-edge site configuration was sampled by a 4×3×1 *k*-point grid.

5.2 Energy Calculations

Active sites on M-N-C catalysts are named as MN_xC_y sites, in which M denotes the doped metal atom (Fe, Co, and Ni), x is the number of coordinated N atoms which is from 1 to 4, and y is the number of C atoms that coordinated with the metal atom which varies from 1 to 3. For active sites that coordinated with no C atom (y has value of 0), the suffix C_0 was neglected. The value of $x+y$ equals 4 for the fully embedded double-vacancy site and the edge-to-edge site, whereas such value equals 3 for the fully embedded single-vacancy site. The x value was denoted as the summation of the number of N atoms on each edge in the edge-to-edge active sites, e.g., $MN_{2+0}C_2$ and MN_{2+2} sites are the active sites with doped N atoms on only one edge and both edges of a pore in graphene, respectively.

The formation energy of MN_xC_y sites were calculated by

$$E_{form} = E_{MN_xC_y} + n\mu_C - E_{graphene} - (x\mu_N + E_M) \tag{5.7}$$

Where $E_{MN_xC_y}$ is the calculated energy of the MN_xC_y site model and $E_{graphene}$ is the calculated energy of a pristine graphene layer with the same size before doping. $n\mu_C$ is the energy of carbon atoms removed from the graphene layer during doping. n denotes the number of removed carbon atoms, which equals x+2 in fully embedded double-vacancy sites and edge-to-edge sites, and x+1 for fully embedded single-vacancy sites. μ_C is the chemical potential of a single carbon atom in graphene. μ_N is the chemical potential of a nitrogen atom which was defined as the half energy of a nitrogen molecule. E_M is the energy of a single M (i.e., Fe, Co, and Ni) atom isolated in vacuum. Consequently, a more stable active site should exhibit a more negative formation energy E_{form}.

The free energy of the adsorbed intermediate species was calculated using the reversible hydrogen electrode (RHE) as the reference which was developed by Nørskov et al.[129] The free energy of a pair of proton and electron ($H^{+}+e^{-}$) can be calculated as the free energy of ½ H_2, i.e., $G(H^+) + G(e^-) = \frac{1}{2}G(H_2)$ at pH=0.[38, 129] The free energy change ΔG of intermediate species can be calculated as:

$$\Delta G = \Delta E_{ads} + \Delta E_{ZPE} - T\Delta S \tag{5.8}$$

where ΔE_{ads} denotes the adsorption energy of intermediate species on the active site, ΔE_{ZPE} represents the difference of zero-point-energy correction. The zero-point energy for each specie was calculated by the summation of each vibrational mode of binding molecules and adatoms as $E_{ZPE} = \sum \frac{1}{2} h v_i$, where v_i is the *i*-th vibrational mode. The temperature was set to be 298 K. The entropy change ΔS from vibrational contribution of adsorbates is also evaluated by the harmonic vibrational mode[130, 131]

$$S_{vib} = k_B \sum_{i=1}^{3N} \left[\frac{h v_i}{k_B T} \left(e^{\frac{h v_i}{k_B T}} - 1 \right)^{-1} - \ln \left(1 - e^{-\frac{h v_i}{k_B T}} \right) \right] \tag{5.9}$$

and the contribution from membrane is neglected. The entropy change of free molecules under standard condition is taken from the NIST database. [132]

When applying a bias U on the electrode and pH-values of electrolyte differ from 0, extra correction terms are added to the free energy calculation equation 5.8,

$$\Delta G = \Delta E_{ads} + \Delta E_{ZPE} - T\Delta S + \Delta G_U + \Delta G_{pH} \tag{5.10}$$

where the energy shift from the applied electrode potential is evaluated as $\Delta G_U = -neU$, in which n is the number of electrons transferred in the reaction and the electrode potential U is given with the reference to RHE. In the theoretical RHE, the correction of free energy change from H^+ concentration can be evaluated by the effects from pH-values as $\Delta G_{pH} = -kT \times pH \times ln10$.

In the aforementioned periodic boundary condition DFT calculations, the overall charge in a unit cell is always treated as neutral (i.e., constant charge method). The potential effect is only evaluated via the energy shift in electron transfer steps, but the change of electric field on the interface is ignored.[133] The constant potential method was proposed by Head-Gordon et al.[134], Goddard et al.[135, 136, 137], and Sautet et al.[138] In this method, the Fermi-level can be tuned by changing the number of electrons in the system. Thus, the work function Φ and applied potential U can be fixed to a desired value during each relaxation step.[139, 140] The actual applied potential on the electrode can be calculated by linking the work function of the system to the standard hydrogen electrode (SHE),

$$U = \frac{\Phi - \Phi_{SHE}}{e} \tag{5.11}$$

The experimental work function of SHE was adopted 4.3 eV here.

Since the number of electrons is changed in the system, a correction is needed to when calculating the free energy,

$$G_{correct} = G - N_e \mu_e \tag{5.12}$$

where G is the free energy calculated under the constant potential U, N_e is the number of electrons that changed in the system to reach the target potential, μ_e is the chemical potential of electrons under U which is the calculated Fermi energy.

5.3 Implicit Solvation Model

The physics of the solid-liquid interface plays a critical role in the electrochemical reactions. Despite the resource-consuming explicit solvation model, the implicit solvation model was used in this study. The implicit solvation model uses the continuum dielectric description of solvent surrounding the solute, for which the solute is immersed in a solvent bath.[141] In this model, the solute is described using DFT, the electrolyte is described using linearized Poisson-Boltzmann equation, and the interface between solute and electrolyte is described by electrostatically coupling of DFT and Poisson-Boltzmann equation.[142] The total free energy of the solute and electrolyte system can be calculated based on the net electrostatic potential ϕ and electronic charge density $n(\vec{r})$. After calculating the stationary point of the total free energy, the solvation potential and Poisson-Boltzmann equation can be obtained with respect to the electronic charge density $n(\vec{r})$ and electrostatic potential ϕ, respectively. The obtained solvation potential is an additional term to the Hamiltonian to the Kohn-Sham equation. The additional term in the local potential part can be calculated with the shape function, the electrolyte charge density, and the entropy for mixing ions in the electrolyte. The linearized Poisson-Boltzmann equation can be described by the relative permittivity of solvent and Debye length which is used to neutralize the non-zero charge in the simulation cell.[142]

The implicit solvation model was already implemented in VASPsol.[141, 142] which was employed in this work for investigating the electrochemical stability of M-N-C catalysts. Solving the linearized Poisson-Boltzmann equation which is described as:

$$\vec{\nabla} \cdot \epsilon \vec{\nabla} \phi - \kappa^2 \phi = -\rho_s \tag{5.13}$$

where ϵ is the relative permittivity of solvent, and ρ_s represents the total solute charge density. κ^2 in the equation 5.13 can be described as:

$$\kappa^2 = \zeta[n(\vec{r})]\frac{1}{\lambda_D^2} \tag{5.14}$$

in which ζ is the shape function as a function of the electronic charge density $n(\vec{r})$, and λ_D is the Debye length. In this dissertation, the dielectric constant of water of 78.4 was used for the relative permittivity of solvent, and the Debye screening length was set to be 9.61 Å for simulating the monovalent electrolyte at the concentration of 0.1 M. The default values were used for other parameters in solving the linearized Poisson-Boltzmann equation.

The implicit solvation model conjunct with the constant potential method were used in the calculations for systems with solvation effects. The unit cells of fully embedded and edge-to-edge MN_xC_y site models used for implicit solvation model calculations are 9.84×8.52 Å and 9.84×12.79 Å. A large separation of 50 Å was added perpendicular to the graphene layer as suggested by former studies.[139, 140, 143] In order to fix the potential on the charged interface between the electrode and electrolyte, the net charge in the simulation cell was changed from -0.6e to 0.6e with increments of 0.2e. The targeted potential U was fixed in each step calculations using the equation 5.11. The energy correction that shown in equation 5.12 was used in free energy calculation for NRR intermediate species.

6.0 Results and Discussions

6.1 Chemical Environment and NRR Performance of MN_xC_y Active Sites

The carbon based electrocatalysts with heteroatoms doping have already been proved to exhibit superior catalytic performance as compared to traditional pure metal catalysts, especially the metal-nitrogen doped carbon (M-N-C) catalysts.[71, 78, 144, 145] In a metal-nitrogen doped carbon catalyst, isolated metal atoms dispersed on the N-doped carbon supporters and coordinated with doped N atoms.[146, 147, 148] Such catalysts were well synthesized through coordinative pyrolysis using metal-organic frameworks (MOFs) as precursors, especially the zeolitic imidazolate frameworks (ZIFs), which has high surface area, good mechanical flexibility and facile functionalization at the molecule level.[148] The sufficient anchoring sites and various amine sites on MOFs provide a precondition for stabilizing dispersed metal atoms with relatively strong metal-nitrogen bonding. The pyrolyzed M-N-C catalysts consist of co-doped nitrogen and earth-abundant transition metals (e.g., Fe, Co, and Ni) were already defined as promising electrocatalysts for NRR.[73, 80, 81, 99, 144, 149] In such M-N-C catalysts, the chemical environment, including the local carbon structure and active site configuration, plays a significant role in determining the NRR performance of catalysts. The atomic structures of MN_xC_y active sites in M-N-C catalysts reported in previous NRR experimental results are mainly fully embedded MN_3 and MN_4 sites[77, 78, 80, 81, 99, 150], while very limited results for other active site configurations were reported[79]. In contrast, theoretical screening studies for NRR active sites have shown other possible configurations for MN_xC_y sites with various rations of *x* and *y*.[90, 102, 105, 151] However, the stability of active sites and the local carbon structure were ignored. In this section, the thermodynamic stability of MN_xC_y sites was examined through formation energy calculations, the NRR activity of MN_xC_y sites was predicted through the free energy calculations for NRR intermediate species, and the selectivity toward NRR was evaluated through the comparison between NRR and competing hydrogen evolution reaction (HER).

6.1.1 Atomic Models of MN_xC_y Sites

In this thesis, two types of local carbon structure of active sites, which are the fully embedded and edge-to-edge active sites, were investigated with three types of doped metal atoms (Fe, Co, and Ni). For the fully embedded structure of MN_xC_y sites (**Figure 6.1**), all the models used in the DFT calculations share the same unit cell size of 9.84×8.52 Å. Two types of central vacancy site of fully embedded active sites were considered, namely the single vacancy site and double vacancy site. Regarding single or double vacancy site, it indicates the vacancy site was generated by removing one or two C atoms from the graphene layer, respectively. In the single vacancy MN_xC_y site, the summation of x and y values in its name should equal three which is also the coordination number of a C atom in the graphene layer. For the double vacancy MN_xC_y site, the summation of x and y values equals four as it forms a porphyrin-like structure with four neighboring pyridinic N atoms in the graphene layer.

There are totally nine different types of active site configurations were investigated for fully embedded MN_xC_y sites, which are MN_1C_2, MN_1C_3, MN_2C_1, $MN_2C_{2\text{-hex}}$, $MN_2C_{2\text{-opp}}$, $MN_2C_{2\text{-pen}}$, MN_3, MN_3C_1, and MN_4 sites as shown in **Figure 6.1**. Consequently, there would be totally twenty-seven models of the fully embedded structure included in the DFT calculations. The

MN_1C_2, MN_2C_1, and MN_3 sites are the fully embedded single vacancy sites, whereas the MN_1C_3, $MN_2C_{2\text{-hex}}$, $MN_2C_{2\text{-opp}}$, $MN_2C_{2\text{-pen}}$, MN_3C_1, and MN_4 sites are the fully embedded double vacancy sites. The structures of MN_1C_2 (**Figure 6.1a**) and MN_2C_1 (**Figure 6.1c**) site exhibit a mirror symmetry in the active site moiety, hence there is only one unique structure for each configuration. The MN_3 (**Figure 6.1g**) site possesses a C_{3v} symmetry in the active site moiety, which also leads to only one unique active site configuration. In fully embedded double vacancy sites, the MN_1C_3 (**Figure 6.1b**), MN_3C_1 (**Figure 6.1h**), and MN_4 (**Figure 6.1i**) sites also only have one unique structure for each configuration. However, the fully embedded double vacancy sites with the central metal atom coordinated with two N atoms have a more complex condition of the active site symmetry. As shown in **Figure 6.1d-f**, the surrounding local carbon structure is only two-fold symmetry for the active site, which leads to three unique structures for the MN_2C_2 site configuration. The first one is the $MN_2C_{2\text{-hex}}$ site (**Figure 6.1d**) which has both pyridinic N atoms on the same side of the metal atom and in one hexagonal ring. The second one is the $MN_2C_{2\text{-opp}}$ site (**Figure 6.1e**) which consists of two pyridinic N atoms on different sides of the metal atom and in opposite direction. The third one is the $MN_2C_{2\text{-pen}}$ site (**Figure 6.1f**) with two pyridinic N atoms on the same side of the metal atom and the same pentagonal ring.

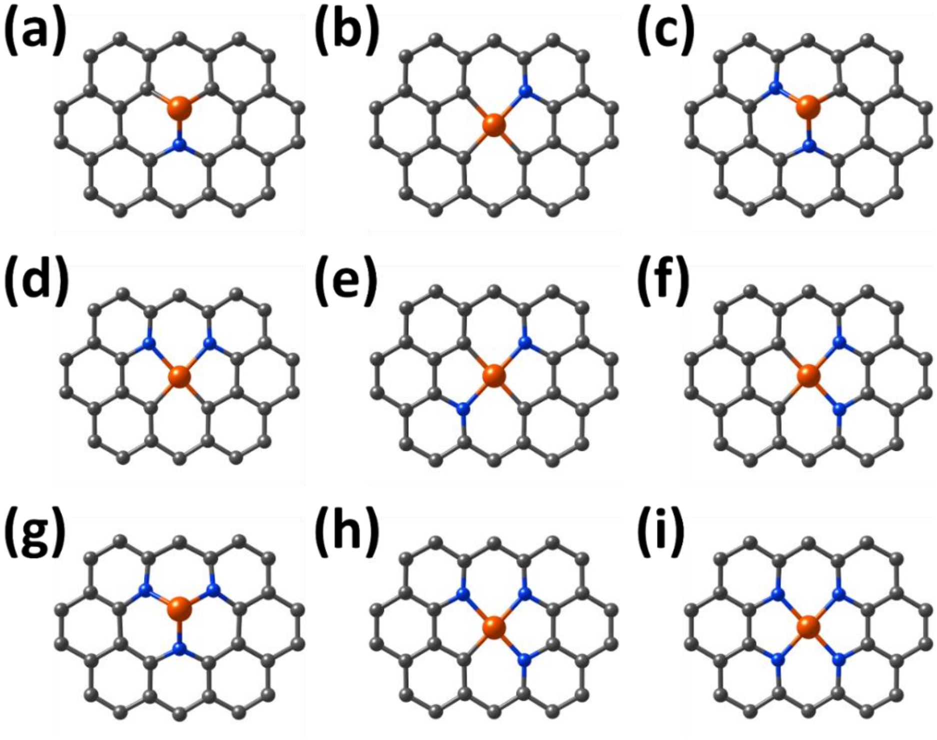

Figure 6.1. Atomic structures of fully embedded (a) MN_1C_2, (b) MN_1C_3, (c) MN_2C_1, (d) $MN_2C_{2\text{-hex}}$, (e) $MN_2C_{2\text{-opp}}$, (f) $MN_2C_{2\text{-pen}}$, (g) MN_3, (h) MN_3C_1, and (i) MN_4 sites. The gray, blue and orange balls represent C, N and metal atoms, respectively.

The edge-to-edge local carbon structure in which two N-doped edges of a pore bridged by the central metal atom was studied as the active site for both oxygen reduction reaction (ORR)[94, 98, 152] and carbon dioxide reduction reaction (CO2RR)[153, 154] with various types of doped metal atom. However, active sites with such local carbon structure were not included in previous NRR studies. Here, six different types of edge-to-edge structure which leads to totally eighteen configurations were considered in the DFT calculations with the same size of unit cell of 9.84×12.79 Å (**Figure 6.2**). The MN_xC_y site with edge-to-edge local carbon structure also exhibits a porphyrin-like configuration for the active site moiety, but with pores on both sides of the active site. The number of coordinated N atoms, which is the value of *x* in MN_xC_y, is shown as the summation of the number of doped N atoms on each edge. In the $MN_{1+0}C_3$ site (**Figure 6.2a**), there is only one N atom doped on one of the bridged edges. For the $MN_{1+1}C_2$ site, three unique configurations were considered for the edge-to-edge structure because of the symmetry. In the $MN_{1+1}C_{2\text{-opp}}$ site (**Figure 6.2b**), two doped N atoms are on the different edges with opposite direction, whereas two doped N atoms are on symmetric on each edge in the $MN_{1+1}C_{2\text{-sym}}$ site (**Figure 6.2c**). In the $MN_{2+0}C_2$ site (**Figure 6.2d**), two N atoms are on the same edge of the pore. There is one N atom doped on one of the edges of pore and two N atoms on the other edge in the $MN_{2+1}C_1$ site (**Figure 6.2e**), while there are two N atoms on both edges in the MN_{2+2} site (**Figure 6.2f**).

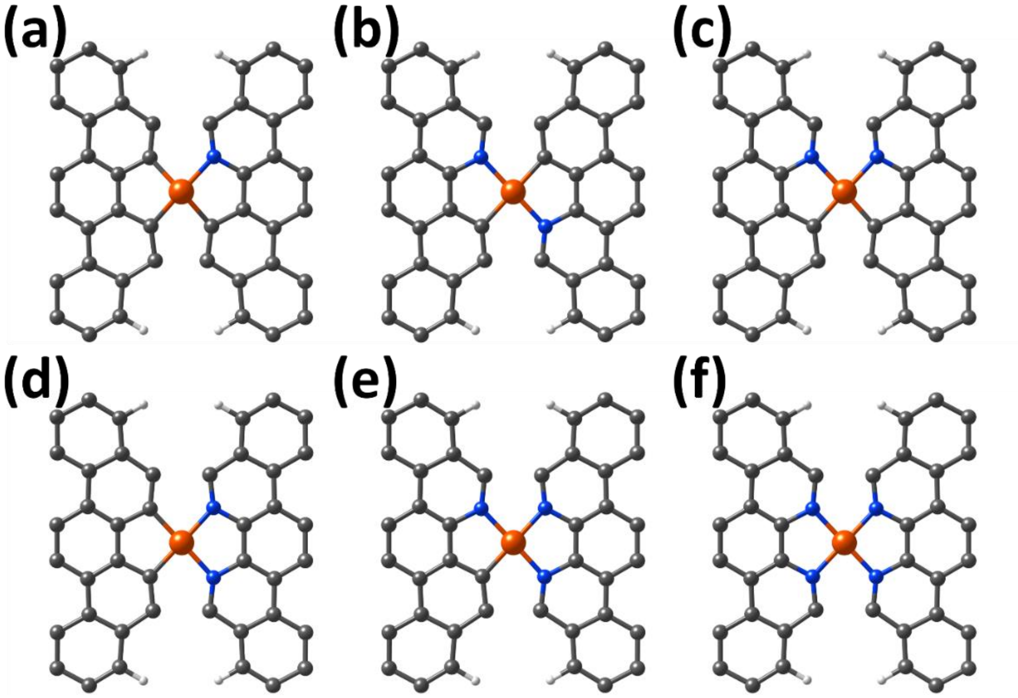

Figure 6.2. Atomic structures of edge-to-edge (a) $MN_{1+0}C_3$, (b) $MN_{1+1}C_{2\text{-opp}}$, (c) $MN_{1+1}C_{2\text{-sym}}$, (d) $MN_{2+0}C_2$, (e) $MN_{2+1}C_1$, and (f) MN_{2+2} sites. The gray, blue, white and orange balls represent C, N, H, and metal atoms, respectively.

6.1.2 Stability of MN_xC_y sites

In the pyrolyzed M-N-C catalysts, the thermodynamic stability of MN_xC_y sites is related to the formation and density of the active sits in the catalysts. The stability of MN_xC_y sites was examined with the calculation of the active site formation energy E_{form}. As discussed in section 5.2, the formation energy E_{form} of active sites was obtained by comparing the calculated electronic energy between reactants and products during the formation of active sites. Hence, the preliminary task in active site formation energy calculations was to determine the reactants and products during the MN_xC_y site formation. For the fully embedded MN_xC_y sites, a pristine graphene layer with the same unit cell size, the isolated nitrogen molecule and isolated single metal atom were used as the reactants. The fully embedded MN_xC_y site model and single C atoms from graphene were treated as the products. A one-step process was used here for the formation of fully embedded MN_xC_y site directly from the corresponding graphene. For the formation of single vacancy and double vacancy sites, the only difference in this procedure is the number of removed C atoms and doped N atoms. For instance, a fully embedded MN_4 site was generated through six C atoms in graphene substituted by four doped pyridinic N atoms and one metal atom (**Figure 6.3a**). In contrast, the formation process of a fully embedded MN_3 site contains removing four C atoms from graphene and doping three N atoms and one metal atom (**Figure 6.3b**).

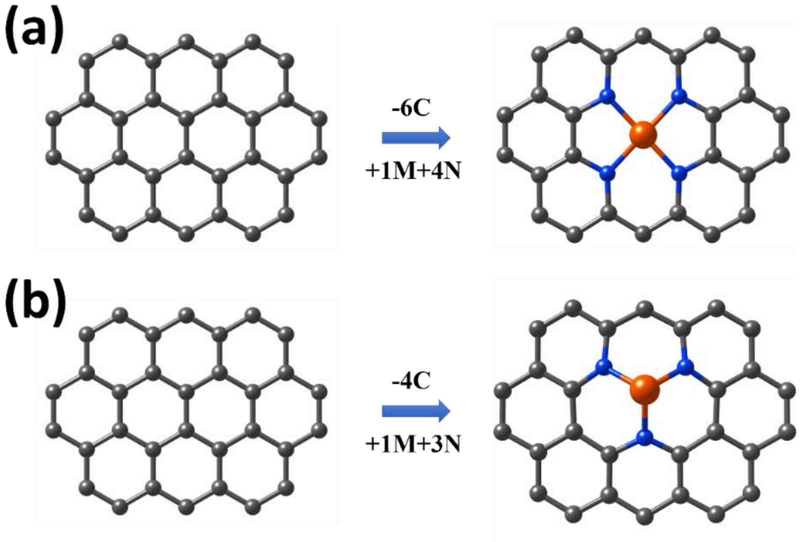

Figure 6.3. Schematics for the formation of fully embedded (a) double vacancy MN_4 and (b) single vacancy MN_3 sites. The gray, blue and orange balls represent C, N and metal atoms, respectively.

The results of calculated E_{form} for all the fully embedded MN_xC_y sites are shown in **Table 6.1**. Generally, the more N atoms coordinated with the central metal atom in the active site, the more stable active sites would be. The FeN_1C_3, CoN_1C_3, and NiN_1C_2 sites exhibit a positive value for the active site formation energy, indicating a very poor thermodynamic stability in graphene. For all three types of doped metal atoms (i.e., Fe, Co, and Ni), the MN_4 site is always the most stable configuration among all the fully embedded sites. Among the MN_2C_2 sites with three types of doped metal atoms, the $MN_2C_{2\text{-opp}}$ sites were predicted to be the most unstable one, while the $MN_2C_{2\text{-hex}}$ site always exhibited the lowest formation energy. It should be noted that the calculated formation energy is only a theoretical estimation for the actual stability of each active site, hence the relative stability of MN_xC_y sites is also very important. Using the most stable FeN_4, CoN_4, and NiN_4 sites as the reference, MN_xC_y sites that exhibit formation energy difference less than 3.00 eV as compared with corresponding MN_4 sites were considered relatively stable in graphene.

Consequently, the FeN_1C_2, CoN_1C_2, NiN_1C_3, and NiN_2C_1 sites were also identified not thermodynamically stable in pyrolyzed M-N-C catalysts. Such procedure for identifying stable MN_xC_y sites was also proved by previous experimental results. The $FeN_2C_{2\text{-opp}}$,[155] $CoN_2C_{2\text{-opp}}$,[156] and $NiN_2C_{2\text{-opp}}$[157, 158] sites were found stable in M-N-C catalysts, which can be used as the reference. FeN_xC_y sites that exhibit lower formation energy than $FeN_2C_{2\text{-opp}}$ sites were considered thermodynamically stable. Same method was also used for CoN_xC_y and NiN_xC_y sites to compare with $CoN_2C_{2\text{-opp}}$, and $NiN_2C_{2\text{-opp}}$ sites, respectively. Specially, the FeN_2C_1 and CoN_2C_1 sites show very close value of formation energy with the $FeN_2C_{2\text{-opp}}$ and $CoN_2C_{2\text{-opp}}$ sites, respectively. Hence, the FeN_2C_1 and CoN_2C_1 sites were also considered as stable active sites. Similar results of active site stability were also obtained in a previous theoretical study for Fe-N-C catalysts.[151]

Table 6.1. Calculated active site formation energy (eV) of fully embedded MN_xC_y (M = Fe, Co, and Ni) sites.

Configuration	Fe	Co	Ni
MN_1C_3	0.41	0.23	-0.06
MN_1C_2	-0.18	-0.61	0.27
MN_2C_1	-0.55	-1.11	-0.37
$MN_2C_{2\text{-opp}}$	-0.70	-1.15	-1.48
$MN_2C_{2\text{-hex}}$	-1.20	-1.68	-2.10
$MN_2C_{2\text{-pen}}$	-0.83	-1.29	-1.64
MN_3	-1.18	-1.69	-1.14
MN_3C_1	-2.07	-2.70	-2.80
MN_4	-3.33	-3.91	-3.73

For the formation of edge-to-edge MN_xC_y sites, the same method was used to identify the reactants and products. The same-size graphene layer, isolated hydrogen and nitrogen molecules, and a single metal atom were used as the reactants. The edge-to-edge MN_xC_y site model and removed single C atoms were considered as products, which is similar to the formation of fully embedded sites. However, the formation process of edge-to-edge MN_xC_y sites is different from the fully embedded MN_xC_y sites as it included the pore formation. A two-step procedure was used for the formation of edge-to-edge MN_xC_y site, in which an intermediate step of pore formation in the graphene layer was added. As the formation of MN_{2+2} site shown in **Figure 6.4**, eight C atoms were removed from the pristine graphene layer for pore formation while four H atoms were added to the pore edges for termination in the first step. In the second step, the central two C atoms were replaced by the doped metal atom, and the neighboring four C atoms on the edges were substituted by doped N atoms. Consequently, there were totally fourteen C atoms removed from the system, whereas four N and H atoms along with one metal atom were introduced into the system.

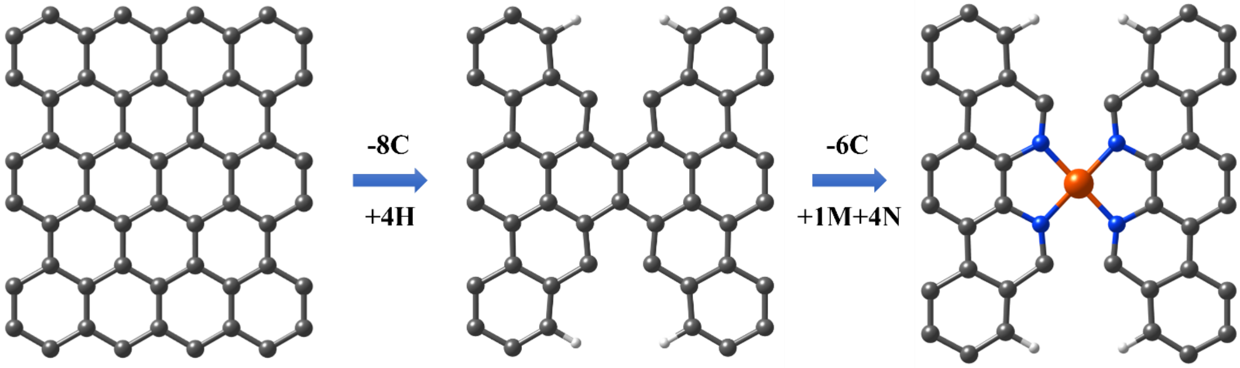

Figure 6.4. Schematic for the formation of edge-to-edge MN_4 site. The gray, blue, white and orange balls represent C, N, H, and metal atoms, respectively.

Because of the formation of pores, especially the dangling C atoms on the edge of pores, the edge-to-edge MN_xC_y sites were expected to be less stable than the fully embedded MN_xC_y

sites. The calculated values of formation energy E_{form} for all possible edge-to-edge MN_xC_y sites with various numbers of doped N atom are all positive, which indicates the formation of such edge-to-edge active site should be thermodynamically unfavored (**Table 6.2**). However, it should be noted that the first step of pore formation in the edge-to-edge active site formation procedure could lead to a huge increase of system energy. In the second step, the formation of active site moiety results in a decrease of system energy in all edge-to-edge active site models. Hence, once only the proper pore structure is formed in graphene, the formation of edge-to-edge MN_xC_y sites can be thermodynamically favored. The stability trend in various edge-to-edge MN_xC_y sites is the same as the fully embedded sites, for which the increasing number of doped N atoms in the active site moiety would stabilize the active site structure.

Table 6.2. Calculated active site formation energy (eV) of edge-to-edge MN_xC_y (M = Fe, Co, and Ni) sites.

Configuration	Fe	Co	Ni
$MN_{1+0}C_3$	8.77	8.28	8.24
$MN_{1+1}C_{2\text{-sym}}$	7.55	6.81	6.34
$MN_{1+1}C_{2\text{-opp}}$	7.78	7.01	6.47
$MN_{2+0}C_2$	7.66	6.87	6.47
$MN_{2+1}C_1$	6.71	5.75	5.67
MN_{2+2}	5.74	4.79	4.82

From the results of formation energy calculations for both fully embedded and edge-to-edge MN_xC_y sites, it can be concluded that the stability of MN_xC_y sites significantly depends on the chemical environment of active site which involves local carbon structure and active site configuration. The MN_xC_y sites with fully embedded structures were predicted to be much more stable than the ones with edge-to-edge structures, which indicates a much larger density of fully embedded MN_xC_y sites are expected in M-N-C catalysts. For both fully embedded and edge-to-edge MN_xC_y sites, the increasing number of doped N atoms that coordinated with the central metal atom in the active site would always result in a more stable configuration. Specifically, the MN_4 sites were predicted to be the most stable configuration in all Fe-N-C, Co-N-C, and Ni-N-C catalysts, which means these active sites are the ones that most likely to be found in corresponding M-N-C catalysts. In addition, for the fully embedded MN_xC_y sites, the double vacancy active sites were normally more stable than the single vacancy active site with a lower formation energy.

6.1.3 NRR on MN_xC_y sites

The electrochemical nitrogen reduction reaction (NRR) on MN_xC_y sites can be described in general as $\mathrm{N_2 + 6H^+ + 6e^- \rightleftarrows 2NH_3}$. As a very complicated process, the NRR pathway involves nine possible intermediate species, which are $*N_2$, $*NNH$, $*NNH_2$, $*NHNH$, $*NHNH_2$, $*NH_2NH_2$, $*N$, $*NH$ and $*NH_2$. The asterisk in each name denotes the adsorption on the MN_xC_y site. The primary task in investigating the NRR activity on MN_xC_y site is to identify the favorable NRR pathway on it. Three distinct types of pathways were defined for associative electrochemical NRR in previous studies, which are the distal, alternating and enzymatic pathways. [9, 25, 30, 53, 54] All the three pathways start with the adsorption of $*N_2$, which is a step that does not involve proton and electron transfer. For the distal and alternating pathways, the adsorption of $*N_2$ on the active site is preferred in an end-on configuration, whereas the side-on adsorption of $*N_2$ is favored for the enzymatic pathway. The distal pathway first goes through the hydrogenation of the distal N in adsorbed $*N_2$ to yield the first NH_3 molecule, and then the remained proximal N is hydrogenated to the second NH_3 molecule. In contrast, the reaction sequence for alternating and enzymatic goes through alternatively hydrogenating on two N atoms in the adsorbed $*N_2$ to produce two NH_3 molecules. Moreover, the hybrid pathway was also considered as potential NRR pathway in this thesis as it was proposed as favorable NRR pathway in our previous studies.[80, 159] In this section, the free energy calculations were performed for all possible adsorption configurations of nine NRR intermediate species on each MN_xC_y site to identify the favored pathway for NRR. Consequently, the NRR activity was predicted through the calculated free energy evolution diagram for each MN_xC_y site.

6.1.3.1 N_2 Adsorption on MN_xC_y Sites

The adsorption of $*N_2$ was first investigation for both fully embedded and edge-to-edge MN_xC_y sites as it is critical for the NRR to occur on these sites. Here, only the stable fully embedded MN_xC_y sites that identified in section 6.1.2 were investigated for NRR, as other thermodynamically unfavored sites are expected to form with an infinitesimal density in M-N-C catalysts which are neglectable. Although all the edge-to-edge MN_xC_y sites were found thermodynamically unfavored in M-N-C catalysts, the edge-to-edge FeN_{2+2}, CoN_{2+2} and NiN_{2+2} sites were also included as the existence of FeN_{2+2} sites in Fe-N-C catalysts was proved by previous experimental studies.[160, 161, 162] It should be noted that the formation of edge-to-edge MN_xC_y sites requires a pore with proper structure was already formed in graphene, which should lead to a very low density of such edge-to-edge MN_xC_y site in M-N-C catalysts.

Since the adsorption of $*N_2$ is not an electron-transfer step, it mainly depends on the properties of the catalysts. The calculated free energy changes of $*N_2$ adsorption (ΔG_{*N_2}) on the MN_xC_y sites was used to evaluate the ability of MN_xC_y sites to capture a N_2 molecule. The adsorption of $*N_2$ was investigated for all possible configurations on the MN_xC_y sites, while only the configuration of $*N_2$ adsorption with the lowest adsorption energy was considered the stable $*N_2$ adsorption. As shown in **Table 6.3**, most FeN_xC_y sites exhibit negative values for calculated ΔG_{*N_2}, which indicates a favored $*N_2$ adsorption on these FeN_xC_y sites. Although the value of ΔG_{*N_2} of $*N_2$ adsorption on the $FeN_2C_{2\text{-pen}}$ sites was found positive (0.06 eV), it is still very small avoiding an energy barrier for $*N_2$ adsorption to occur. The $*N_2$ adsorption on most CoN_xC_y sites were also found thermodynamically favored with negative values of ΔG_{*N_2}, except on the CoN_4 and CoN_{2+2} sites. These two CoN_xC_y sites both possess four pyridinic N atoms coordinated with the central Co atom, indicating such configuration in CoN_xC_y sites is not beneficial for $*N_2$ adsorption. In contrast to the favored $*N_2$ adsorption on most FeN_xC_y and CoN_xC_y sites, the $*N_2$ adsorption was found not unfavorable on most NiN_xC_y sites. The fully embedded NiN_3 site was found as the only NiN_xC_y site that has a negative value of ΔG_{*N_2}. The adsorption of $*N_2$ was found impossible on $NiN_2C_{2\text{-pen}}$, NiN_3C_1 and NiN_4 sites which agrees with the results in a previous study.[102] Large energy barriers were found for the on $NiN_2C_{2\text{-opp}}$, $NiN_2C_{2\text{-hex}}$ and NiN_{2+2} sites as shown in **Table 6.3**, which indicates the unfavorable $*N_2$ adsorption on these NiN_xC_y sites. Moreover, it can be also concluded that the $*N_2$ adsorption was found more favored on the fully embedded MN_xC_y sites with the central metal atom in a single vacancy site.

Table 6.3. Calculated free energy changes of $*N_2$ adsorption (eV) on MN_xC_y sites.

Configuration	Fe	Co	Ni
MN_2C_1	-0.89	-0.56	
$MN_2C_{2\text{-opp}}$	-0.07	-0.20	0.47
$MN_2C_{2\text{-hex}}$	-0.05	-0.20	0.47
$MN_2C_{2\text{-pen}}$	0.06	-0.20	
MN_3C_1	-0.09	-0.11	
MN_3	-0.86	-0.85	-0.80
MN_4	-0.06	0.36	
MN_{2+2}	-0.20	0.17	0.50

To provide an insight of the underlying mechanism for $*N_2$ adsorption, the electronic structure of these MN_xC_y sites was investigated using the charge distribution analysis. The charge distribution analysis was calculated by comparing the electron densities on central metal atom in the active site moiety with those on a corresponding isolated metal atom. For the FeN_xC_y sites that most beneficial for $*N_2$ adsorption, a density of electron accumulation or namely charge depletion (cyan cloud) was shown on the top site of the central Fe atom (**Figure 6.5**). The FeN_2C_1 and FeN_3 sites with the central Fe atom in a single vacancy site exhibit a non-planar configuration for the active site moiety as shown in **Figure 6.5a**,**e**. Such non-planar configuration results in a more polarized charge distribution with more electron accumulation on the top site of the central Fe atom. For CoN_xC_y sites that also favors $*N_2$ adsorption, the electron accumulation or charge depletion was also found on the top site of the central Co atom as shown in **Figure 6.6**. In contrast, the charge distribution analysis results of CoN_4 and CoN_{2+2} sites shown a large density of electron depletion or charge accumulation (yellow cloud) on the top site of the central Co atom. Similar results were also found for the charge distribution analysis on NiN_xC_y sites (**Figure 6.7**). Only the

NiN_3 site has the obvious electron accumulation on the top site of the central Ni atom which promotes the $*N_2$ adsorption. For other NiN_xC_y sites that exhibit unfavored or infeasible $*N_2$ adsorption, only a density of electron depletion was found on the top site of the central Ni atom.

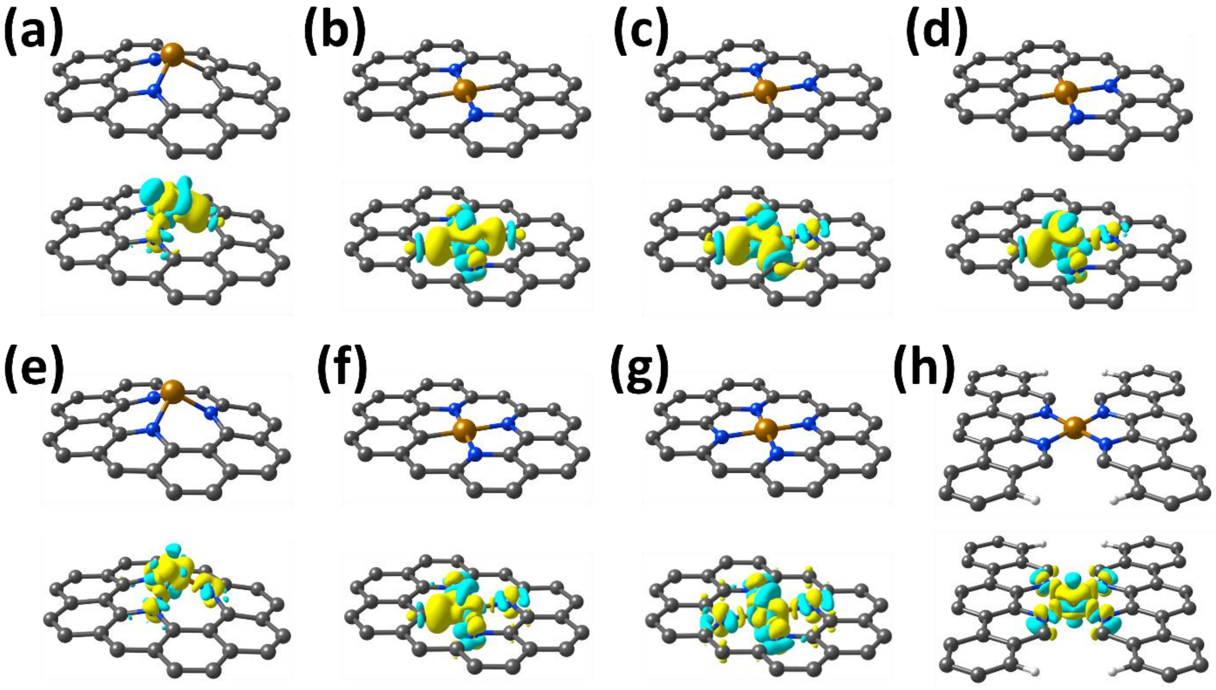

Figure 6.5. Atomic (upper panel) and electronic (lower panel) structures of fully embedded (a) FeN_2C_1, (b) $FeN_2C_{2\text{-opp}}$, (c) $FeN_2C_{2\text{-hex}}$, (d) $FeN_2C_{2\text{-pen}}$, (e) FeN_3, (f) FeN_3C_1, (g) FeN_4, and (h) FeN_{2+2} sites. The gray, blue, white, and golden balls represent C, N, H, and Fe atoms, respectively. The charge accumulation and depletion are shown as yellow and cyan clouds with the isosurface of 0.0075 e/Å^3.

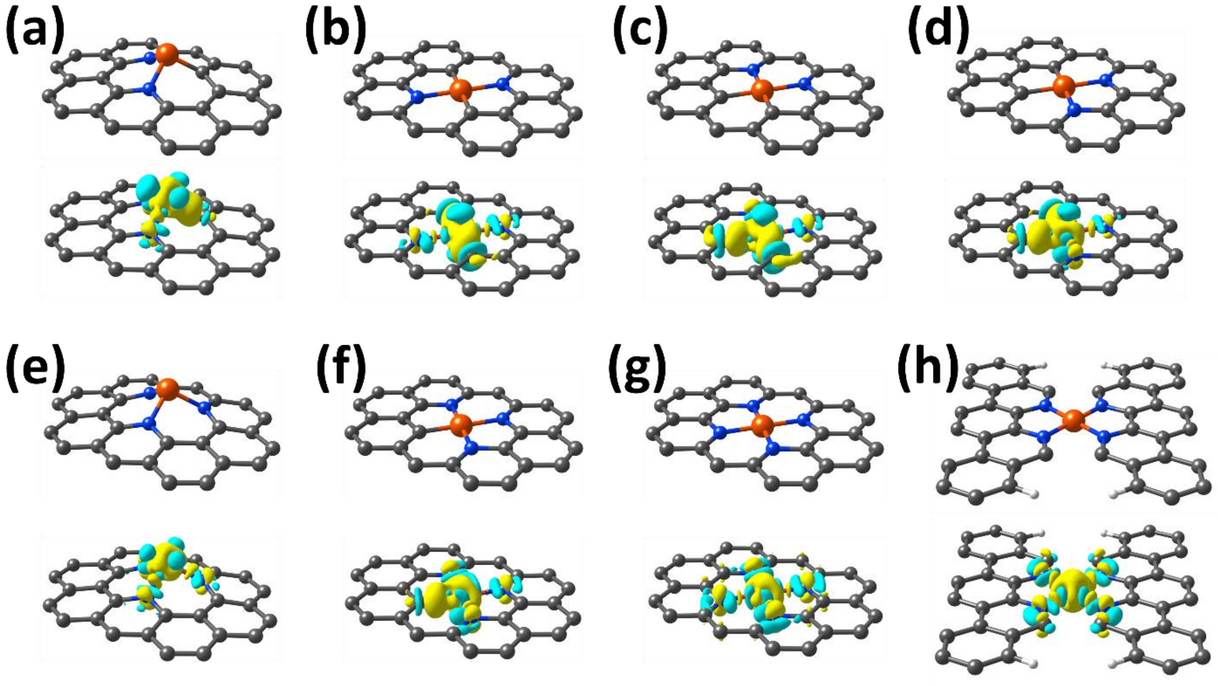

Figure 6.6. Atomic (upper panel) and electronic (lower panel) structures of fully embedded (a) CoN_2C_1, (b) $CoN_2C_{2\text{-opp}}$, (c) $CoN_2C_{2\text{-hex}}$, (d) $CoN_2C_{2\text{-pen}}$, (e) CoN_3, (f) CoN_3C_1, (g) CoN_4, and (h) CoN_{2+2} sites. The gray, blue, white, and orange balls represent C, N, H, and Co atoms, respectively. The charge accumulation and depletion are shown as yellow and cyan clouds with the isosurface of 0.0075 e/Å^3.

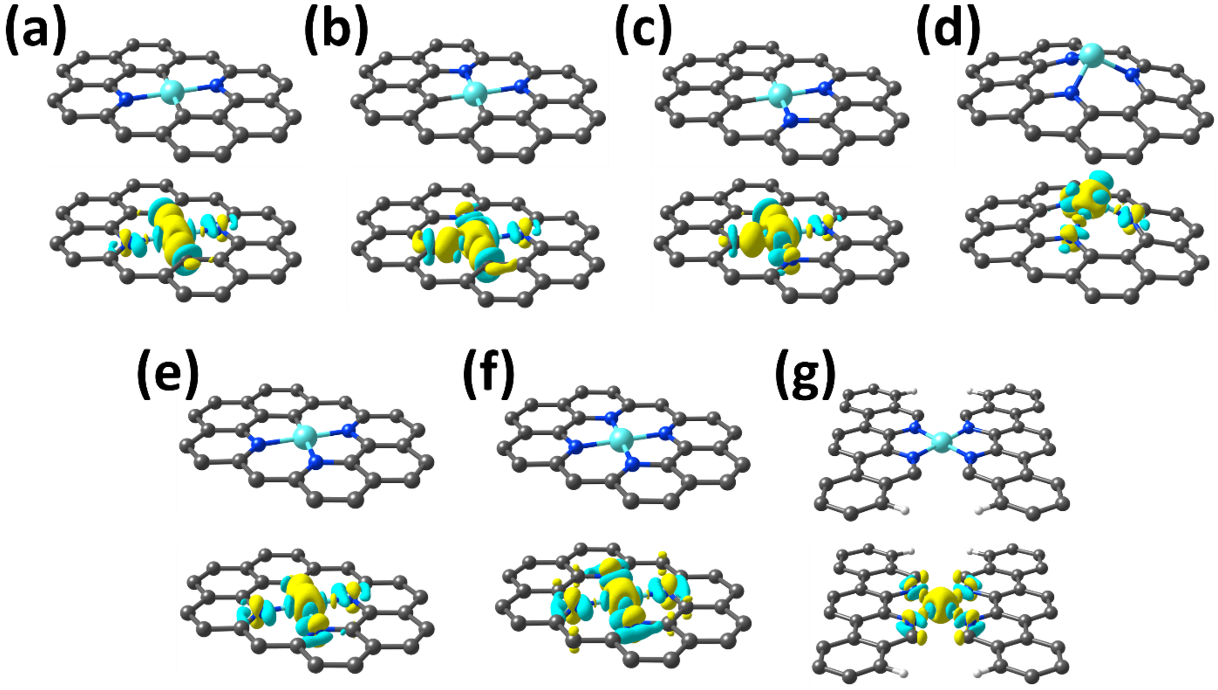

Figure 6.7. Atomic (upper panel) and electronic (lower panel) structures of fully embedded (a) $NiN_2C_{2\text{-}opp}$, (b) $NiN_2C_{2\text{-}hex}$, (c) $NiN_2C_{2\text{-}pen}$, (d) NiN_3, (e) NiN_3C_1, (f) NiN_4, and (g) NiN_{2+2} sites. The gray, blue, white, and cyan balls represent C, N, H, and Ni atoms, respectively. The charge accumulation and depletion are shown as yellow and cyan clouds with the isosurface of 0.0075 e/Å^3.

As the first step in NRR, the adsorption of $*N_2$ initiates the activation of inert N_2 molecule, which requires the weakening of the stable N≡N bond. Such activation process is closely relevant to the bonding nature between the central metal atom in NiN_xC_y site and adsorbed $*N_2$. The central transition metal atom (i.e., Fe, Co, and Ni) needs to provide empty 3*d* orbitals to accept the σ-orbital lone-pair electrons from N atoms in the N_2 molecule. Meanwhile, the *d*-orbital electrons from the central metal atom are transferred to the empty π*-orbital of N_2 through a back-donation process.[105, 163, 164] Hence, the electron accumulation on the top site of central metal atom can promote the back-donation process for $*N_2$ adsorption. Thus, NiN_xC_y sites that exhibit electron depletion on the top site of central atom lack the ability to provide electron for N≡N bond activation, which leads to the unfavored $*N_2$ adsorption or even repulse between the central metal atom and N_2 molecule.

6.1.3.2 NRR Activity of MN_xC_y Sites

The NRR activity of all stable MN_xC_y sites were predicted through the free energy calculations for the intermediate species on the active sites. The free energy of all possible adsorption configurations for each NRR intermediate specie was calculated to locate the most stable adsorption. Then stable intermediate species for each adsorption and hydrogenation step were used to predict the favorable NRR pathway on the MN_xC_y site. During the NRR pathway on MN_xC_y sites, there were several steps that caused positive free energy change requiring additional energy from applied electrode potential to overcome such barrier. The hydrogenation step, which involves the electron transfer process, exhibited the highest free energy increase was treated as the potential determining step (PDS) for NRR. Moreover, the reverse electrode potential that needed to overcome the free energy increase in the PDS on the MN_xC_y site was defined as the limiting potential for NRR ($U_{L(NRR)}$). Consequently, a more positive value for $U_{L(NRR)}$ means a better NRR activity. In previous theoretical studies, two possible steps were identified as PDS for NRR, which are the first hydrogenation step from $*N_2$ to $*NNH$, and the last hydrogenation step from $*NH_2$ to $*+NH_3$.[29, 102, 105] In this thesis, the PDS for NRR on all the investigated MN_xC_y sites were identified to be the first hydrogenation step from $*N_2$ to $*NNH$.

Table 6.4. Calculated limting potential for NRR (V) on MN_xC_y sites.

Configuration	Fe	Co	Ni
MN_2C_1	-0.96	-0.98	
$MN_2C_{2\text{-opp}}$	-0.75	-0.98	-1.58
$MN_2C_{2\text{-hex}}$	-0.89	-0.98	-1.64
$MN_2C_{2\text{-pen}}$	-0.76	-1.05	
MN_3C_1	-0.74	-1.37	
MN_3	-0.83	-1.00	-0.83
MN_4	-1.31	-1.05	
MN_{2+2}	-1.13	-1.40	-1.74

The calculated values for $U_{L(NRR)}$ of various MN_xC_y sites are shown in **Table 6.4**. The $FeN_2C_{2\text{-opp}}$, $FeN_2C_{2\text{-pen}}$, and FeN_3C_1 sites have the values of $U_{L(NRR)}$ around -0.75 V, which are more positive than those of other FeN_xC_y sites, indicating the best NRR activity of these three sites in Fe-N-C catalysts. The calculated values of $U_{L(NRR)}$ for FeN_xC_y sites here are generally in agreement with previous results.[151] For active sites in the Co-N-C catalyst, the CoN_2C_1, $CoN_2C_{2\text{-opp}}$, and $CoN_2C_{2\text{-hex}}$ sites have the almost identical value of $U_{L(NRR)}$, which indicates the same NRR activity of these three active CoN_xC_y sites. However, even the most active CoN_xC_y site exhibits a very negative value (~ -1.00 V) for $U_{L(NRR)}$, which would lead to a poor NRR activity of Co-N-C catalysts. Most NiN_xC_y sites shown in **Table 6.4** exhibit very negative value of $U_{L(NRR)}$ except the NiN_3 site, which shows a value of -0.83 V for $U_{L(NRR)}$. Hence, it can be predicted that only the Ni-N-C catalyst that holds enough NiN_3 sites would be active for NRR. For each configuration of MN_xC_y site, the active site that involves a Fe atom as the central metal atom in the moiety would has the most positive value of $U_{L(NRR)}$ and the best NRR activity, while the only exception is the

MN_4 site. Furthermore, as all the edge-to-edge FeN_{2+2}, CoN_{2+2}, and NiN_{2+2} sites show very negative value of $U_{L(NRR)}$, these sites were predicted to be not active for NRR.

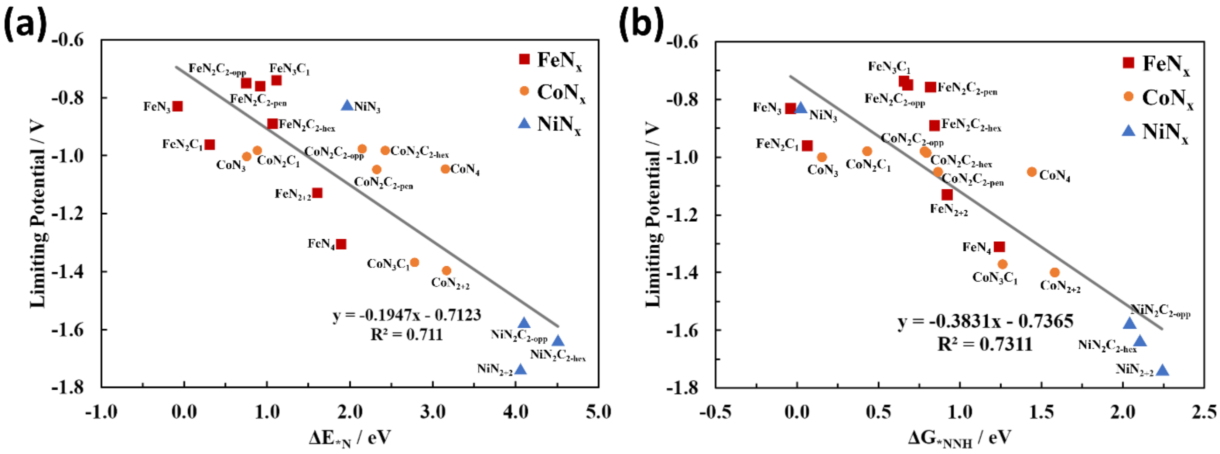

Figure 6.8. (a) The scaling relation between predicted limiting potential for NRR and the adsorption energy of *N. (b) The scaling relation between predicted limiting potential for NRR and the free energy change in *NNH adsorption.

As elaborated in previous studies, some descriptors were suggested for the NRR activity, including the adsorption energy of *N[29, 38, 92], and the free energy change for *NNH adsorption[102, 151]. First, the correlation between the adsorption energy of *N (ΔE_{*N}) and limiting potential for NRR ($U_{L(NRR)}$) was examined and shown in **Figure 6.8a**. The adsorption energy of *N is a good indicator for the capability of active sites to binding with all the NRR intermediate species.[92] The limiting potential for NRR of each MN_xC_y site was plot as the data point against ΔE_{*N}, in which a linear relation was found between $U_{L(NRR)}$ and ΔE_{*N} for all active site configurations. Such linear relation indicates the stronger adsorption *N on the MN_xC_y site, the better NRR activity of the same site. Moreover, the correlation between the free energy change for *NNH adsorption (ΔG_{*NNH}) and $U_{L(NRR)}$ was also examined and shown in **Figure 6.8b**. Since all the MN_xC_y sites hold the hydrogenation step from $*N_2$ to *NNH, the free energy of *NNH adsorption would be critical for the NRR activity. A linear relation between ΔG_{*NNH} and $U_{L(NRR)}$ was found for all the MN_xC_y sites, which indicates the stronger binding of *NNH on the MN_xC_y site would result in a better NRR activity of the same site. In addition, the data points of FeN_xC_y sites (red cubic) are mostly found at the upper left corner in both plots of **Figure 6.8**, which also indicates FeN_xC_y sites generally have better NRR activity than both CoN_xC_y (orange circle) and NiN_xC_y (blue triangle) sites.

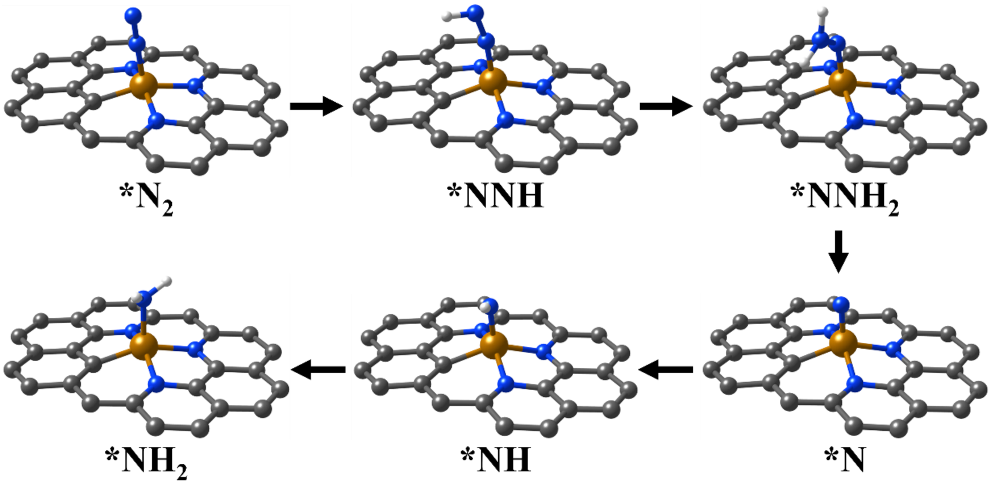

Figure 6.9. Atomic structures of intermediate species along the favorable NRR pathway on the FeN_3C_1 site. In the figure, the gray, blue, white, and golden balls represent C, N, H and Fe atoms, respectively.

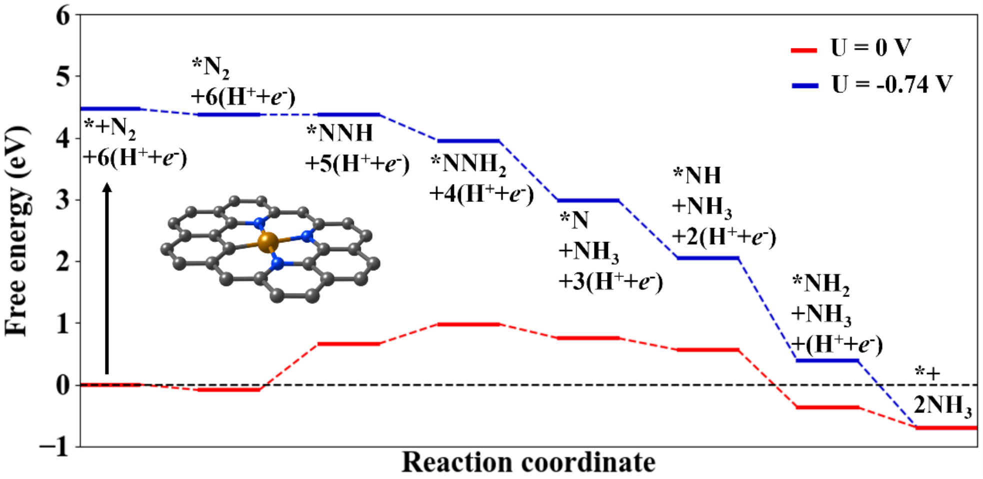

Figure 6.10. Predicted free energy evolution of NRR on the FeN_3C_1 site without applied potential (red line) and under limiting potential (blue line).

To gain an insight of NRR pathway on MN_xC_y sites, the free energy evolution diagrams were predicted for the FeN_3C_1, $CoN_2C_{2\text{-opp}}$, and NiN_3 sites, which are the most active sites for Fe-N-C, Co-N-C, and Ni-N-C catalysts, respectively. First, the stable adsorption of intermediate species was investigated on the FeN_3C_1 site. The favored pathway for NRR on the FeN_3C_1 site was predicted to be a distal one (**Figure 6.9**). The distal N atom in the end-on adsorbed $*N_2$ was hydrogenated first by three H atoms to yield the first NH_3 molecule. Then the remained proximal N atom reacted with another three H atoms to produce the second NH_3 molecule. The bond length between two N atoms increased from 1.14 Å in the adsorbed $*N_2$ to 1.30 Å in $*NNH_2$, which clearly shows the weakening and activation of the inert N≡N bond. The predicted free energy evolution of NRR on the FeN_3C_1 site was shown in **Figure 6.10**. From the free energy evolution under 0 V applied potential (red line), it can be noticed that only the two hydrogenation steps before the N-N bond cleavage exhibit positive free energy change. The step from $*N_2$ to *NNH possesses the highest free energy increase as the PDS, while such energy barrier was removed when NRR occurs under applied electrode potential (blue line).

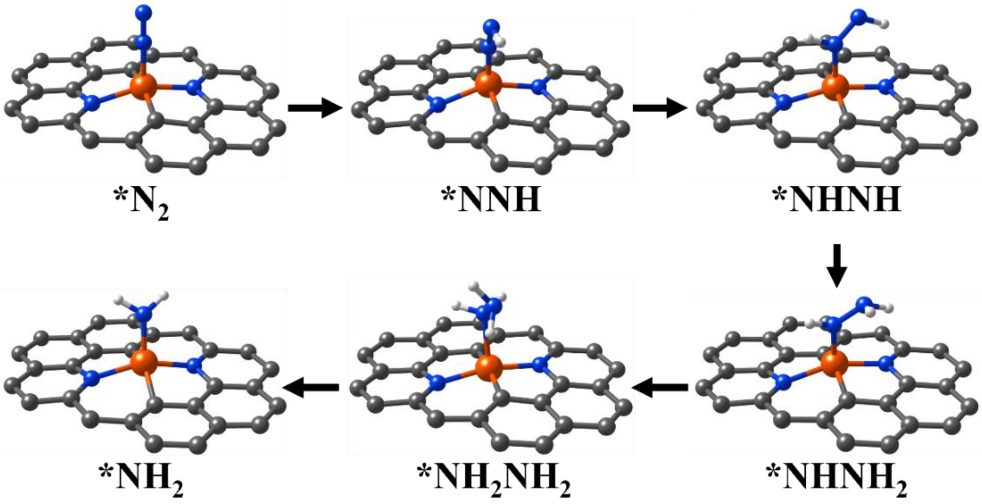

Figure 6.11. Atomic structures of intermediate species along the favorable NRR pathway on the $CoN_2C_{2\text{-opp}}$ site. In the figure, the gray, blue, white, and orange balls represent C, N, H and Co atoms, respectively.

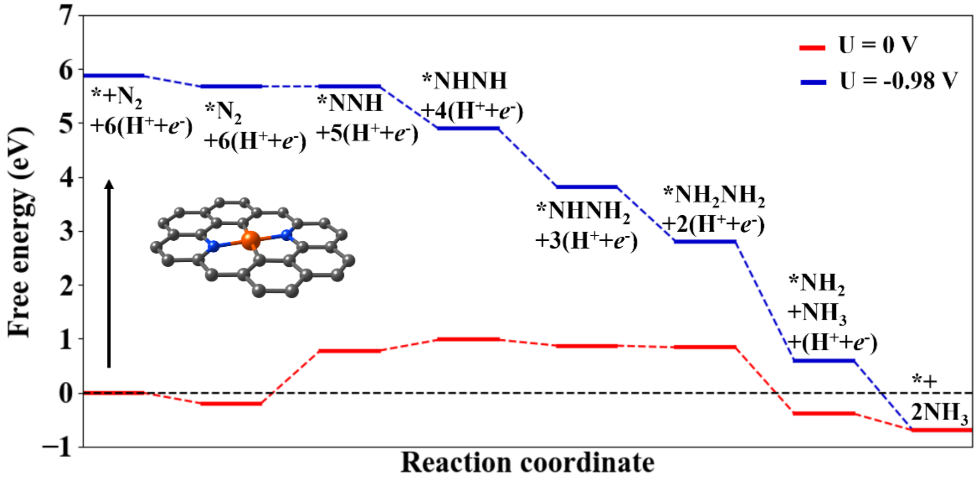

Figure 6.12. Predicted free energy evolution of NRR on the $CoN_2C_{2\text{-opp}}$ site without applied potential (red line) and under limiting potential (blue line).

The investigation of stable adsorption configurations of NRR intermediate species on the $CoN_2C_{2\text{-opp}}$ site was also performed to identify its favorable reaction pathway. As shown in **Figure 6.11**, an alternating pathway was found as the most likely NRR pathway for the $CoN_2C_{2\text{-opp}}$ site. Two N atoms in the end-on adsorbed $^*N_2$ were hydrogenated alternatively until the yielding of two NH_3 molecules. The bond between two N atoms was elongated from 1.14 Å in $^*N_2$ to 1.45 Å in $^*NH_2NH_2$ before cleavage. The longer distance of N-N bond before cleavage on the $CoN_2C_{2\text{-opp}}$ site than that on the FeN_3C_1 site indicates the adsorbed $^*N_2$ on the $CoN_2C_{2\text{-opp}}$ site needed further activation to cleavage, for which more hydrogenation steps were needed before the N-N bond cleavage. The first two hydrogenation steps of NRR on the $CoN_2C_{2\text{-opp}}$ site were found to have positive free energy change, while the subsequent hydrogenation steps were all found exergonic (**Figure 6.12**). Under the limiting potential, all the steps during the alternating NRR pathway changed to be thermodynamically favored.

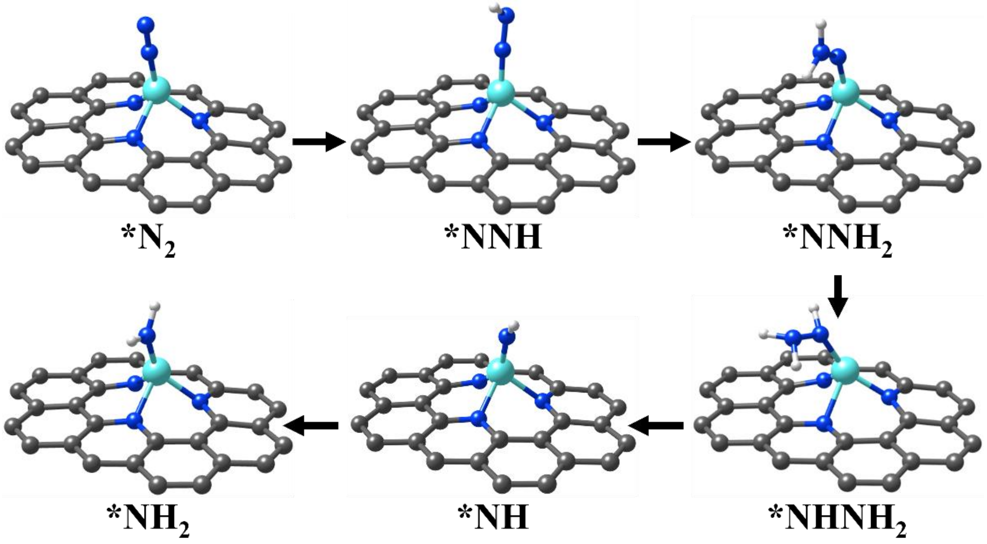

Figure 6.13. Atomic structures of intermediate species along the favorable NRR pathway on the NiN_3 site. In the figure, the gray, blue, white, and cyan balls represent C, N, H and Ni atoms, respectively.

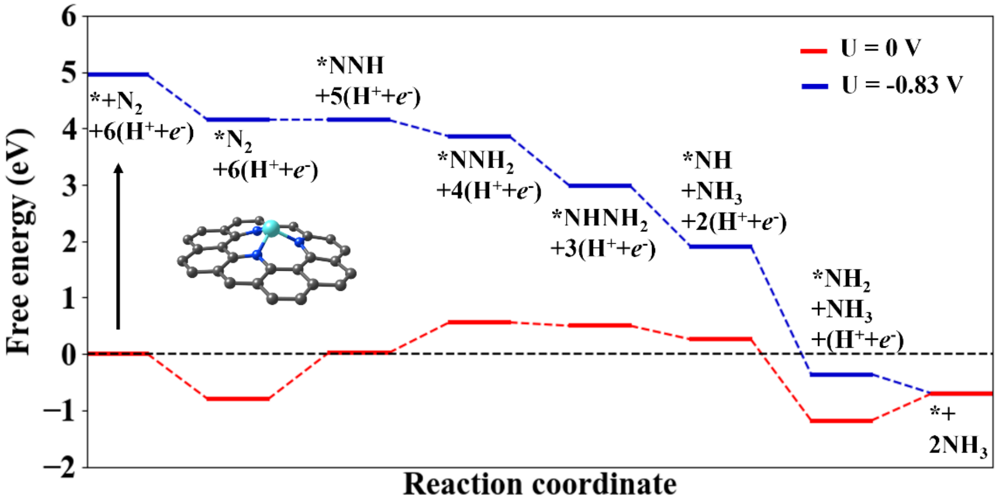

Figure 6.14. Predicted free energy evolution of NRR on the NiN$_3$ site without applied potential (red line) and under limiting potential (blue line).

The most likely NRR pathway on the NiN$_3$ site was found to be a hybrid one, which is different from that on the FeN$_3$C$_1$ and CoN$_2$C$_{2\text{-opp}}$ sites (**Figure 6.13**). The distal N atom in the end-on adsorbed N$_2$ molecule was first hydrogenated by two H atoms to become *NNH$_2$ that tilt along the Ni-N bond in the NiN$_3$ site. The third H atom adsorbed on top of the proximal N atom to form the adsorbed specie *NHNH$_2$. Then the fourth hydrogenation step occurred on the distal N atom and led to the first NH$_3$ molecule desorption. Subsequently, after the N-N bond cleavage, the remained *NH fragment was hydrogenated by extra two H atoms to produce the second NH$_3$ molecule. From the DFT predicted energy evolution shown in **Figure 6.14**, the red line that represents the free energy evolution under 0 V electrode potential shows both the first two and last one hydrogenation steps result in free energy increase during the NRR pathway. Specifically, two trapping intermediate states, which are the *N$_2$ and *NH$_2$ adsorption, were found for NRR on the NiN$_3$ site. Both trapping states required relatively large energy for further hydrogenation, in which the first one is the PDS that shows a higher energy barrier. Furthermore, the calculated NRR limiting potential of NiN_3 site is -0.83 V, which was found in good agreement with the experimental optimal potential of -0.8 V for NRR from a previous study.[80] Under the limiting potential, the whole pathway of NRR on the NiN_3 site becomes thermodynamically favored.

6.1.3.3 NRR Selectivity of MN_xC_y Sites

The hydrogen evolution reaction (HER) is an unavoidable competing reaction to the electrochemical NRR on M-N-C catalysts.[51, 92] Besides other factors in electrochemical reduction of nitrogen to yield ammonia (e.g., the reactor configuration, electrolyte choice, and reaction conditions), the spontaneous properties of NRR catalysts are also essential for selective electrochemical NRR. Electrons in 3*d* orbitals of the central metal can also promote the adsorption of H atoms on the MN_xC_y site, which will lead to a strong competition between NRR and HER on M-N-C catalysts.[165, 166] A proper configuration of the active site is needed to only promote the activity of NRR but suppress the HER.

In this section, the NRR selectivity of all stable MN_xC_y sites was examined by comparing the adsorption strength of critical intermediate species for NRR and HER, and the activity of NRR and HER on MN_xC_y sites. The HER pathway on MN_xC_y sites involves the adsorption of *H and the subsequent desorption of a H_2 molecule. The free energy change in the step of *H adsorption ΔG_{*H} is identified as a descriptor to measure the HER activity.[29, 90, 105] As elaborated in previous studies, electrocatalysts that have the value of ΔG_{*H} that close to 0 will be considered very active for HER.[167] The calculated values of ΔG_{*H} of MN_xC_y sites are shown in **Table 6.5**. The FeN_2C_1 site was found to be the only FeN_xC_y site that has a value of ΔG_{*H} that very close to 0, which indicates the HER would be very favored to occur on this site. The CoN_2C_1, $CoN_2C_{2\text{-opp}}$, $MN_2C_{2\text{-hex}}$, CoN_3C_1, and CoN_3 sites were predicted to have the calculated ΔG_{*H} very close to 0, in which the $CoN_2C_{2\text{-opp}}$ site was also predicted to be active for NRR. The NiN_3 site, which is the only site that was predicted to be active for NRR in Ni-N-C catalysts, was also found to be active for HER with a value of ΔG_{*H} very close to 0. Hence, to obtain the actual NRR selectivity of MN_xC_y sites, further investigations are needed to compare the activity of NRR and HER on the same site.

Table 6.5. Calculated free energy change of *H adsorption (eV) on MN_xC_y sites.

Configuration	**Fe**	**Co**	**Ni**
MN_2C_1	-0.02	0.02	
$MN_2C_{2\text{-opp}}$	0.32	-0.01	0.83
$MN_2C_{2\text{-hex}}$	0.24	-0.10	0.29
$MN_2C_{2\text{-pen}}$	0.17	-0.15	
MN_3C_1	0.31	0.09	
MN_3	-0.41	-0.07	-0.05
MN_4	0.24	0.20	
MN_{2+2}	0.13	0.51	1.24

The first method used here is to compare the free energy change in adsorption step of $*N_2$ and *H ($\Delta G_{*N_2} - \Delta G_{*H}$) on the same MN_xC_y site. It is understandable that if an active site is preferred to be occupied by $*N_2$ adsorption over the *H adsorption, the HER would be suppressed by NRR. Such method was also used in previous studies to investigate the selectivity of NRR electrocatalysts. [79, 90, 100, 102, 105, 168] The MN_xC_y sites that exhibit negative values of $\Delta G_{*N_2} - \Delta G_{*H}$ would also exhibit selectivity toward NRR with suppressed HER. The calculated $\Delta G_{*N_2} - \Delta G_{*H}$ for all MN_xC_y sites are summarized in **Table 6.6**, in which almost all the MN_xC_y sites have negative values for $\Delta G_{*N_2} - \Delta G_{*H}$, except the CoN_4 and $NiN_2C_{2\text{-hex}}$ sites. In general, the FeN_xC_y site has a more negative value for $\Delta G_{*N_2} - \Delta G_{*H}$ as compared to the CoN_xC_y and NiN_xC_y sites with the same configuration, which indicates better NRR selectivity of Fe-N-C catalysts. Specifically, the FeN_2C_1 site was predicted to have the best properties for promoting $*N_2$ adsorption over *H adsorption.

Table 6.6. Calculated free energy change difference between $*N_2$ and *H adsorption (eV) on MN_xC_y sites.

Configuration	Fe	Co	Ni
MN_2C_1	-0.87	-0.58	
$MN_2C_{2\text{-opp}}$	-0.39	-0.20	-0.36
$MN_2C_{2\text{-hex}}$	-0.29	-0.10	0.18
$MN_2C_{2\text{-pen}}$	-0.11	-0.05	
MN_3C_1	-0.40	-0.20	
MN_3	-0.45	-0.78	-0.75
MN_4	-0.30	0.16	
MN_{2+2}	-0.33	-0.34	-0.74

Moreover, the second method used here for determining the NRR selectivity of MN_xC_y sites is comparing the limiting potential of NRR and HER on the same site ($U_{L(NRR)}$-$U_{L(HER)}$). Since the calculated limiting potential of NRR and HER represents the activity of these two competing reactions on the MN_xC_y site, a positive value of $U_{L(NRR)}$-$U_{L(HER)}$ would be equivalent to a good NRR selectivity of this site as the HER is thermodynamically unfavored. Such method was also used in several previous studies to investigate the NRR selectivity of electrocatalysts.[29, 92, 151] As shown in **Table 6.7**, all the calculated values for $U_{L(NRR)}$-$U_{L(HER)}$ are negative, which indicates the limiting potential of HER is constantly less negative than the limiting potential of NRR. Thus, HER was predicted to be more thermodynamically favored than NRR on all the MN_xC_y sites. Similar results were also found in previous theoretical studies for NRR on M-N-C catalysts.[100, 102] The least negative values for $U_{L(NRR)}$-$U_{L(HER)}$ were predicted for the $FeN_2C_{2\text{-opp}}$ and FeN_3C_1 sites, which implies these two active sites have the best NRR selectivity among all the studied MN_xC_y sites.

Table 6.7. Calculated limitng potential difference between NRR and HER (V) on MN_xC_y sites.

Configuration	Fe	Co	Ni
MN_2C_1	-0.97	-0.97	
$MN_2C_{2\text{-opp}}$	-0.43	-0.98	-0.74
$MN_2C_{2\text{-hex}}$	-0.65	-1.08	-1.35
$MN_2C_{2\text{-pen}}$	-0.59	-1.20	
MN_3C_1	-0.44	-1.29	
MN_3	-1.24	-1.07	-0.87
MN_4	-1.07	-0.88	
MN_{2+2}	-1.00	-0.89	-0.50

Therefore, for a good selectivity toward NRR on the MN_xC_y site, the first restriction would be that the HER should not be too easy to occur, which means the free energy change in the step of *H adsorption should not be very close to 0 eV. Then the adsorption of *H needs to be suppressed by $*N_2$ adsorption to avoid the active site been occupied by HER. Furthermore, the activity difference between NRR and HER should not be significant. Thus, the FeN_3C_1 site which was predicted to have the best NRR activity among all the MN_xC_y sites, also exhibits a good NRR selectivity toward NRR.

6.2 NRR on Fe-N-C Catalysts: Strain Effects and Electrochemical Stability

This chapter is modified from the published journal paper: **Shan W**, Wang G. Enhancing Catalytic Properties of Iron-and Nitrogen-Doped Carbon for Nitrogen Reduction through Structural Distortion: A Density Functional Theory Study. *The Journal of Physical Chemistry C* 2021, **125**(29)**:** 16004-16012.[159]

6.2.1 Strained Active Sites in Distorted Fe-N-C catalysts

The process for synthesizing M-N-C catalysts always involves a high-temperature treatment, which is essential for the activation of MN_xC_y sites.[77, 79, 80, 150] There have been many studies showing an abnormal structural distortion in the graphene membrane because of its negative thermal expansion coefficient.[169, 170, 171, 172] Such structural distortion changes the graphene layer into a non-planar configuration under an elevated temperature. The configuration of MN_xC_y active site moiety that embedded in a graphene layer would also be change, which can lead to different adsorption conditions for intermediate species and change of catalytic properties. In a previous study on NRR on Ni-N-C catalysts, the catalytic performance of catalysts is also found related to the temperature of pyrolysis as the optimal performance was obtained on the sample obtained from pyrolysis conditions of 700 ˚C.[80] In addition, our previous studies on the ORR and CO2RR on Fe-N-C catalysts also show that the strain effect that arises from the structure distortion in graphene has been demonstrated to be beneficial for their catalytic activity.[173, 174] The Fe-N bonds in the active sites in Fe-N-C catalysts that pyrolyzed under high temperature were demonstrated to be shortened by ~2%, for which active sites in such catalysts should be compressively strained. However, all the active sites modeled in previous theoretical studies on M-N-C catalysts only assumed a planar graphene layer with fully relaxed configuration. In this section, the effects of compressive strain from a structural distorted graphene layer to the NRR activity and selectivity was investigated for Fe-N-C catalysts.

To date, the Fe-N-C catalyst is one of the most studied NRR electrocatalysts. Both FeN_4[90, 100, 150, 175] and FeN_3[52, 77] sites that embedded in a graphene layer were reported to be active for NRR in previous studies. Hence, efforts in this dissertation were concentrated on investigating the effect of structural distortion on the NRR activity and selectivity of the well-studied FeN_4 and FeN_3 sites. The FeN_4 site that consists of a central Fe atom in a double vacancy site and coordinated with four neighboring N atoms exhibits a planar configuration for the fully relaxed (i.e., unstrained) active site moiety (**Figure 6.15a**). In contrast, the FeN_3 site that consists of a central Fe atom in a single vacancy site and coordinated with three neighboring pyridinic N atoms exhibits a spontaneous non-planar configuration for the active site moiety (**Figure 6.15b**). The Fe atom in the unstrained FeN_3 site is predicted to be out of the graphene layer by 0.32 Å.

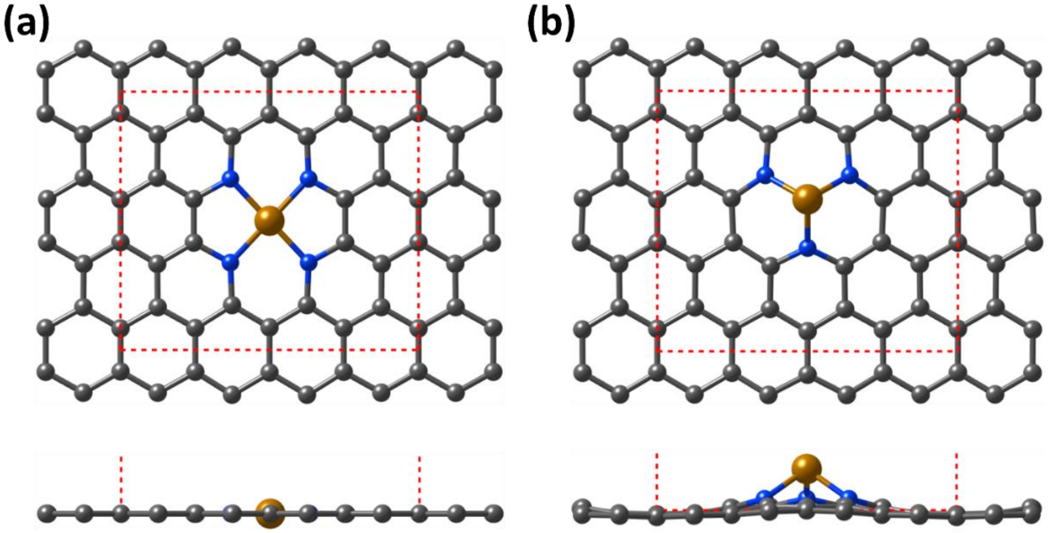

Figure 6.15. Top and side view of atomic structures of unstrained (a) FeN_4 and (b) FeN_3 sites. The unit cell used for DFT calculations on these active sites are marked with red rectangle. The gray, blue, and golden balls represent C, N, and Fe atoms, respectively.

The compressively strained FeN_4 and FeN_3 site models were constructed by contracting with a biaxial compression to the make them have a similarly curved graphene layer. The comparison of unstrained and strained FeN_4 site models is shown in **Figure 6.16**. The compressive strain changed the initial planar graphene layer into non-planar with a wrinkle configuration in the graphene layer as shown in the **Figure 6.16b**. The formed wrinkle in the graphene layer of the strained FeN_4 site model exhibited an off-plane height of 1.27 Å. The central Fe atom is out of the graphene layer by a displacement of 0.28 Å in the strained FeN_4 site. As a result of compressive strain, the length of the Fe-N bonds is shortened by 2.0% in the strained FeN_4 site than those in the corresponding unstrained site. Specifically, the predicted Fe-N bond length (1.85 Å) in the strained FeN_4 site agrees with previous EXAFS measurement results for Fe-N-C catalysts pyrolyzed under high temperature.[173, 174] Moreover, the electronic structures of the FeN_4 sites with and without compressive strain were compared in **Figure 6.16**. The calculated charge distributions on the unstrained FeN_4 site shows a symmetric charge depletion on both top sites of the central Fe atom. In contrast, the charge distribution analysis results for the strained FeN_4 site exhibit an asymmetric distribution of electrons on the central Fe atom with more electrons accumulated to the bulged side to form a more polarized charge distribution on the central Fe atom. Such electronic structure change results in a stabler $^*N_2$ adsorption on the strained FeN_4 site with a 0.20 eV lower adsorption energy.

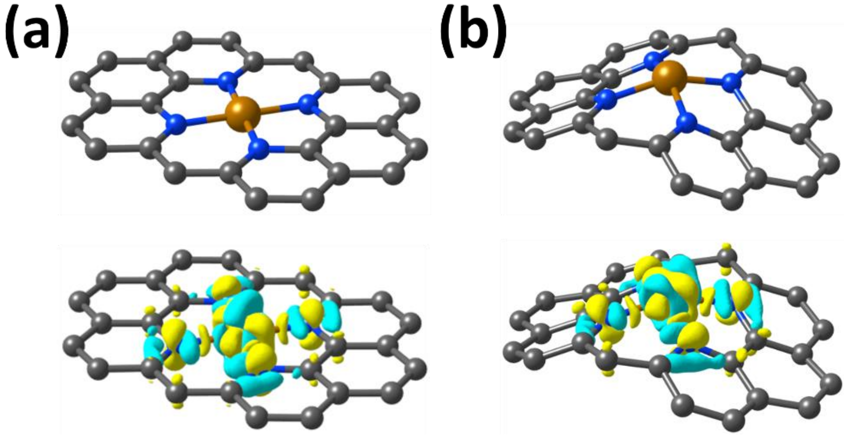

Figure 6.16. The atomic structures (upper panel) and charge distribution (lower panel) of (a) unstrained and (b) strained FeN_4 sites. The charge accumulation and depletion on each active site were shown respectively by the yellow and cyan clouds with an isosurface of 0.0075 e/Å^3. The gray, blue, and golden balls represent C, N, and Fe atoms, respectively.

A change from planar configuration to a non-planar one in the graphene layer was also found in the comparison for atomic structures of FeN_3 sites with and without strain (**Figure 6.17**). The wrinkles contained in the strained FeN_3 site was found to have an off-plane height of 1.29 Å. The central Fe atom is out of the graphene layer by a displacement 1.48 Å in the strained FeN_3

site, which is 1.16 Å higher than that in the unstrained FeN_3 site. The length of the Fe-N bonds was shortened by 0.5% in the strained FeN_3 site than that in the corresponding unstrained site. It is due to the unstrained FeN_3 site moiety was already found non-planar, hence the compressive strain applied on the FeN_3 site would have much smaller effects on the length of Fe-N bonds. The electronic structure analysis results of the unstrained FeN_3 site (**Figure 6.17a**) show a density of charge depletion on top of the Fe atom, which was separated from the charge accumulation surrounding the central Fe atom. The structural distortion in the compressively strained FeN_3 site resulted in more separated charge depletion on the top site of the Fe atom as compared to the unstrained one (**Figure 6.17b**). The compressive strain in the FeN_3 site only caused different densities for charge distribution on the central Fe atom, whereas both the shape and density of charge distribution were changed by the compressive strain in the FeN_4 site.

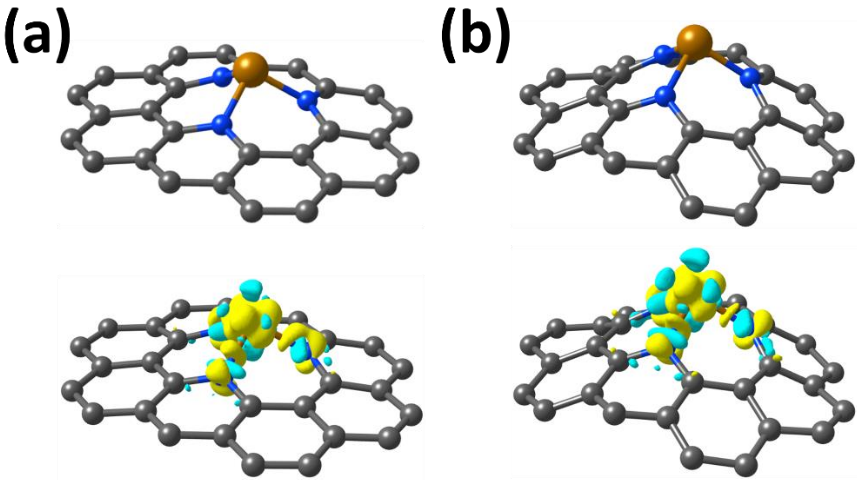

Figure 6.17. The atomic structures (upper panel) and charge distribution (lower panel) of (a) unstrained and (b) strained FeN_3 sites. The charge accumulation and depletion on each active site were shown respectively by the yellow and cyan clouds with an isosurface of 0.0075 e/$Å^3$. The gray, blue, and golden balls represent C, N, and Fe atoms, respectively.

6.2.2 Strain Effects on NRR Pathway and Activity of Fe-N-C catalyst

Since the configurations and electronic structures in the FeN_4 and FeN_3 site were both changed by the compressive strain, it could be expected that the NRR activity and pathway would also be altered. DFT calculations were performed first to predict the most stable adsorption configurations of NRR intermediate species on both FeN_4 and FeN_3 sites with and without strain, which would be help identifying the most likely reaction pathway for NRR. All the nine possible intermediate species of NRR on FeN_4 and FeN_3 sites, which are namely $*N_2$, $*NNH$, $*NNH_2$, $*NHNH$, $*NHNH_2$, $*NH_2NH_2$, $*N$, $*NH$ and $*NH_2$, were considered in free energy calculations. The free energy calculation results of all possible adsorption configurations of each intermediate specie were compared for locating the most stable one. Subsequently, the calculated free energy change of each intermediate specie was used to predict the free energy evolution of the favorable NRR pathways on both FeN_4 and FeN_3 sites with and without strain.

The computational results shown in **Table 6.8** exhibit that the NRR on the compressively strained FeN_4 site has a more positive limiting potential than the unstrained FeN_4 site, which indicates an enhanced NRR activity on the strained FeN_4 site. The predicted limiting potential for NRR on the unstrained FeN_4 site is -1.31 V, which is comparable with the value of -1.36 V from the literature.[100] The compressive strain on the FeN_4 site induced a positive change in $U_{L(NRR)}$ by 0.21 V, which implies that the strained FeN_4 site has better NRR activity than the unstrained one. As shown in **Figure 6.18**, the PDS of NRR on both unstrained and strained FeN_4 sites was found to be the first hydrogenation step from $*N_2$ to *NNH. In addition, the predicted NRR pathway on the unstrained FeN_4 site also shares the same PDS as the previous study.[100]

Table 6.8. Calculated limiting potential of NRR and the free energy change of *NNH adsorption on FeN_4 and FeN_3 sites.

	FeN_4		**FeN_3**	
	Unstrained	**Strained**	**Unstrained**	**Strained**
$U_{L(NRR)}$ (V)	-1.31	-1.10	-0.83	-0.80
ΔG_{*NNH} (eV)	1.25	0.84	-0.04	-0.13

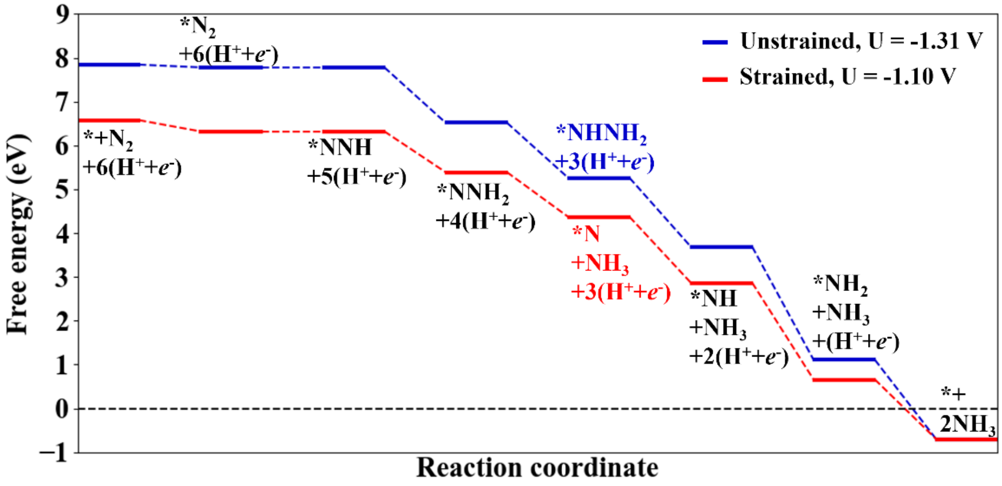

Figure 6.18. Predicted free energy evolution for NRR on the FeN_4 sites with and without strain under their limiting potential.

The compressive strain in the FeN_4 site was also predicted to lead to a change in NRR pathway (**Figure 6.19**). On the unstrained FeN_4 site, the most favorable NRR pathway was predicted to be a hybrid one **(Figure 6.19a)**. Following this pathway, the NRR starts with the N_2

molecule adsorption in an end-on configuration, and the distal N atom of the adsorbed N_2 is first hydrogenated by two H atoms and formed a tilt configuration for $^*NNH_2$ adsorption. Then the third H atom is reacted with the proximal N atom in $^*NNH_2$, and the fourth hydrogenation step leads to the dissociation of N-N bond to produce the first NH_3 molecule. Finally, the remained *NH fragment on top of the Fe atom is subsequently hydrogenated until the second NH_3 molecule desorbs from the active site. The bond length between two N atoms changed from 1.14 Å in $^*N_2$ to 1.40 Å in $^*NHNH_2$ before its cleavage, which shows a weakening and activation for the inert N≡N bond during the hydrogenation. However, the favorable NRR pathway on the compressively strained FeN_4 site was predicted to be a typical distal pathway **(Figure 6.19b)**. On the strained FeN_4 site, after the first two hydrogenation steps occur on the distal N atom, the third hydrogenation step is still on the distal N atom of the adsorbed N_2 and leads to the desorption of the first NH_3 molecule yielding. Subsequently, the remained *N on the active site is hydrogenated to become the second NH_3 molecule produced. The bond length between two N atoms changed from 1.14 Å in $^*N_2$ to 1.31 Å in $^*NNH_2$ before its cleavage. The less hydrogenation steps and shorter N-N bond length before cleavage on the strained FeN_4 site indicates a better spontaneous NRR activity.

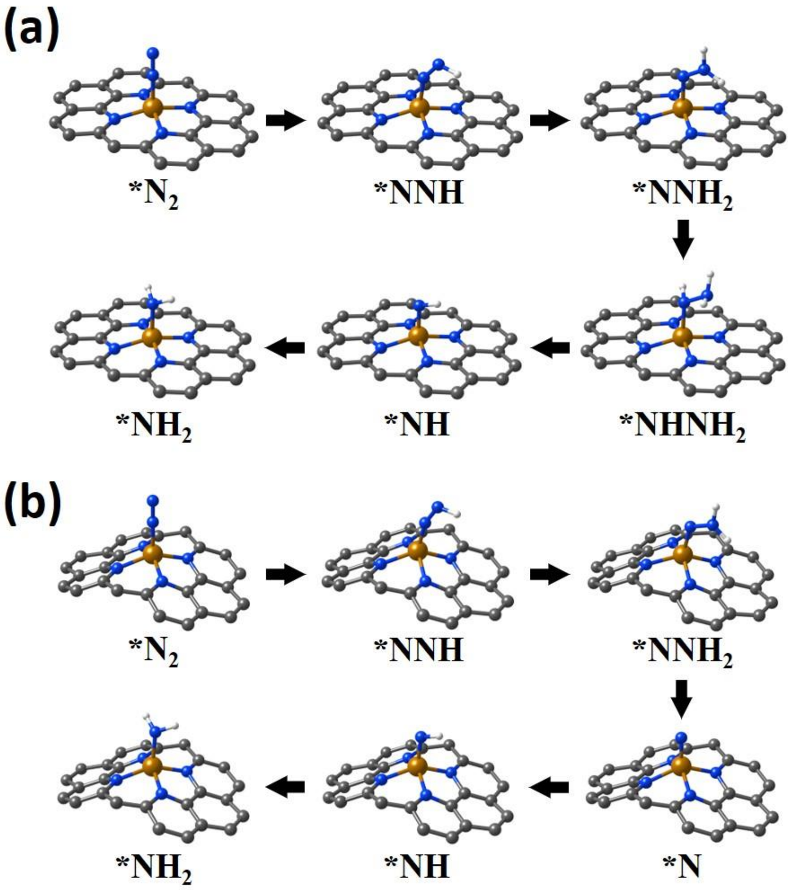

Figure 6.19. The atomic structures of intermediate species along the favorable NRR pathways on (a) unstrained and (b) strained FeN_4 sites. The gray, blue, white and golden balls represent C, N, H, and Fe atoms, respectively.

The predicted free energy evolution of NRR on the unstrained and strained FeN_3 sites is shown in **Figure 6.20**, which also reveals that the first hydrogenation step from $*N_2$ to *NNH is the PDS for NRR on both sites. As shown in **Table 6.8**, the $U_{L(NRR)}$ on the unstrained FeN_3 site is predicted to be -0.83 V, which is very close to a previously reported value of -0.84 V.[77] The predicted free energy evolution for NRR on FeN_3 sites indicates that the FeN_3 site with a compressive strain has a slightly better NRR activity than the unstrained one due to a more positive limiting potential of -0.80 V (**Table 6.8**).

The most favorable NRR pathway on the unstrained FeN_3 site was predicted to be a hybrid one, starting with the N_2 molecule adsorption in an end-on configuration (**Figure 6.21a**). The first H atom adsorbed on the distal N atom of $*N_2$ in the first hydrogenation step. In the second hydrogenation step, the adsorption configuration of the most stable intermediate species changed to a side-on *NHNH. Then, one of the N atoms of *NHNH was preferably hydrogenated by two H atoms to form the first NH_3 molecule. The remained *NH was hydrogenated by extra two H atoms into the second NH_3 molecule produced. The bond length between two N atoms was elongated from 1.14 Å in $*N_2$ to 1.43 Å in $*NHNH_2$ before its cleavage. With compressive strain on this FeN_3 site, the NRR pathway was predicted also to change to a typical distal one. As shown in **Figure 6.21b**, the NRR on the compressively strained FeN_3 site has the same adsorption configurations with the unstrained one in the first two steps, but an end-on $*NNH_2$ adsorption becomes more favored after the second hydrogenation step. The third hydrogenation step resulted in the first yielded NH_3 molecule. Finally, the remained *N on the active site is hydrogenated to become the second NH_3 molecule produced. The distance between two N atoms was elongated from 1.14 Å in $*N_2$ to 1.30 Å in $*NHNH_2$ before its cleavage on the strained FeN_3 site.

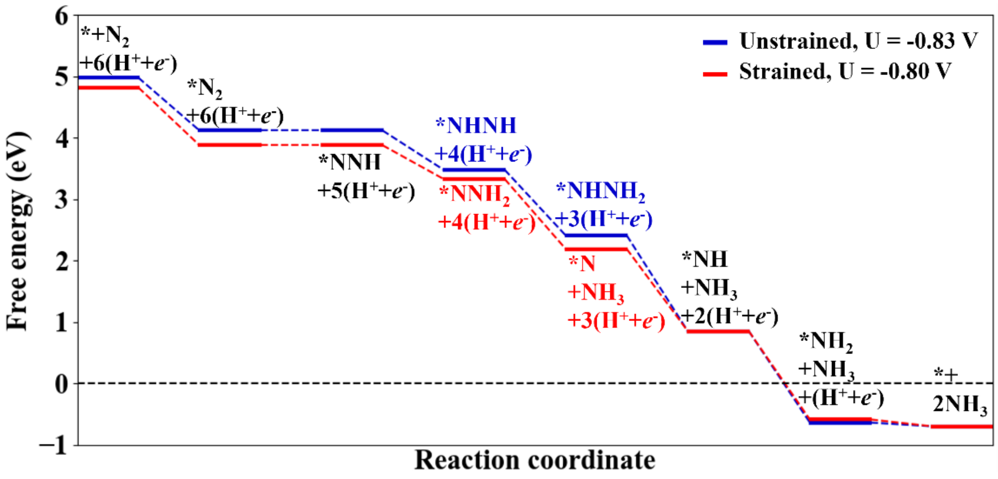

Figure 6.20. Predicted free energy evolution for NRR on the FeN$_3$ sites with and without strain under their limiting potential.

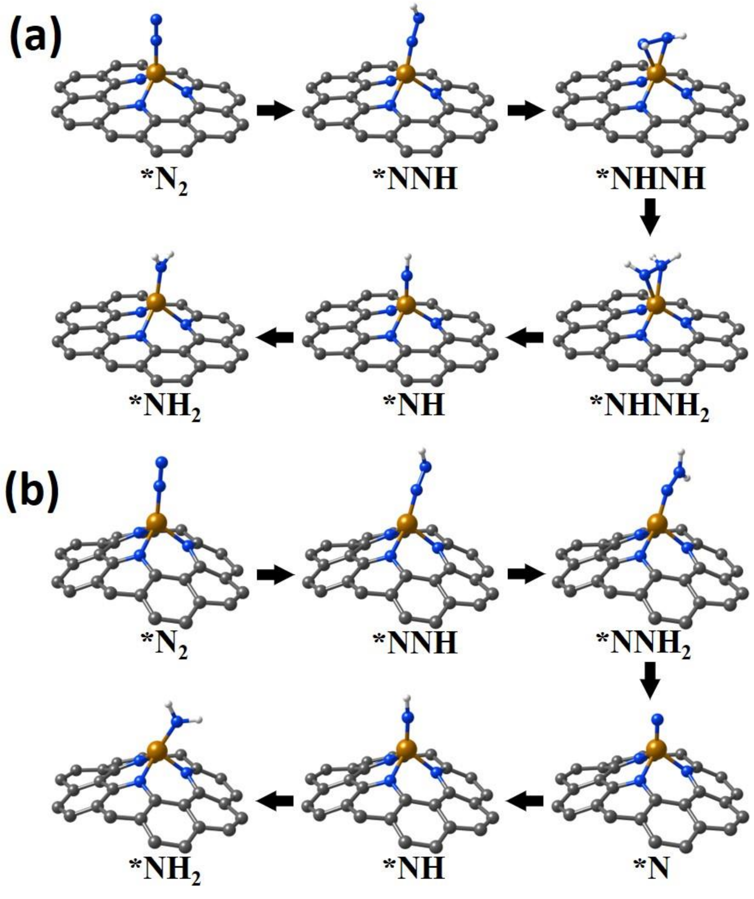

Figure 6.21. The atomic structures of intermediate species along the favorable NRR pathways on (a) unstrained and (b) strained FeN$_4$ sites. The gray, blue, white and golden balls represent C, N, H, and Fe atoms, respectively.

According to the predicted NRR limiting potentials (**Table 6.8**), the unstrained FeN_3 site shows a better NRR activity than the unstrained FeN_4 site with a more positive $U_{L(NRR)}$ by 0.48 V. The strained FeN_3 site also has a more positive $U_{L(NRR)}$ by 0.30 V than the strained FeN_4 site. Thus, it can be inferred that the FeN_3 sites are more active for NRR than the FeN_4 sites in Fe-N-C catalysts. The NRR activity on both FeN_4 and FeN_3 sites is predicted to be enhanced by compressive strain. Moreover, the results in **Table 6.8** demonstrate that compressive strain has an appreciable influence on the NRR activity on FeN_4 sites as the NRR limiting potential has a positive change of 0.21 V due to the structural distortion. In contrast, the NRR limiting potential on the strained FeN_3 site only changes to be more positive by 0.03 V as compared to the unstrained one.

To gain understanding of the compressive strain effect on NRR activity, the bonding analysis for the adsorption of *NNH on the active sites was performed. It has been pointed out that the intermediate species *NNH is a good descriptor for the NRR activity, as most NRR catalysts hold the step from $*N_2$ to *NNH as PDS.[46, 102, 105, 176] The linear relation between the free energy change for *NNH adsorption and the NRR limiting potential was also revealed in section 6.1.3.2 in this dissertation. Indeed, the calculated free energy change for the *NNH adsorption (**Table 6.8**) shows a direct correlation with the predicted NRR limiting potential of the unstrained and strained active sites. Namely, the compressively strained sites have lower energy for NNH adsorption and simultaneously exhibit more positive NRR limiting potentials than the corresponding unstrained sites.

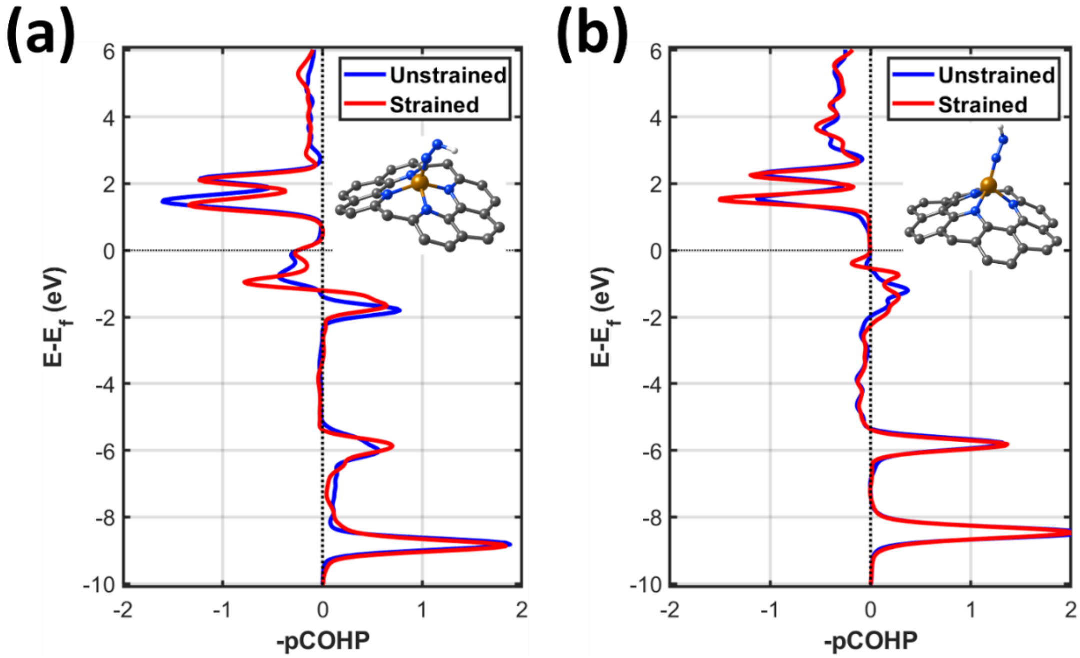

Figure 6.22. -pCOHP analysis results for *NNH adsorption on (a) FeN$_4$ and (b) FeN$_3$ sites.

Specifically, the bonding states between the central Fe atom and the proximal N in adsorbed *NNH was examined using the projected crystal orbital Hamilton population (pCOHP) analysis[177, 178, 179, 180, 181] (**Figure 6.22**), which was applied in previous NRR catalyst studies[46, 89, 151]. The bonding and antibonding states of Fe-N are depicted as the positive and negative parts of -pCOHP curves, respectively. The results show that most of the valence states (i.e., the part below the Fermi level, E$_F$) are bonding states, whereas a small density of antibonding states exist at the Fermi level for both strained and unstrained FeN$_4$ sites (**Figure 6.22a**). These antibonding states at the Fermi level indicates an unstable bonding between *NNH and Fe, which can also be confirmed by the positive free energy change of *NNH adsorption shown in **Table 6.8**. The integrated COHP (ICOHP) up to Fermi level of the strained FeN$_4$ site was predicted to be -2.03 eV, which is more negative than that of the unstrained FeN$_4$ site (-1.96 eV). As revealed in previous studies, a more negative ICOHP indicates a stronger covalent bonding.[46, 89, 151] Hence, the bond analysis further implies a stronger *NNH binding on the strained FeN_4 site. For unstrained and strained FeN_3 sites, the COHP analysis results show that most valence states appear as bonding, and no states are found at the Fermi level (**Figure 6.22b**). In contrast to the results of FeN_4 site, only a small difference is shown in -pCOHP curves between the unstrained and strained FeN_3 sites, suggesting a similar bonding strength between Fe and the proximal N of *NNH. Furthermore, the ICOHP of the strained FeN_3 site differs only by 0.01 eV as compared to that of the unstrained FeN_3 site, which also indicates a similar binding strength of *NNH on the unstrained and strained FeN_3 sites.

6.2.3 Strain Effects on NRR Selectivity of Fe-N-C catalyst

The influence of structural distortion on the selectivity towards NRR on the FeN_4 and FeN_3 sites was also examined. The competing HER is believed to be the primary factor affecting the selectivity of the catalysts for NRR.[51, 80, 92, 102] The activity of HER, which can be used to compare with the activity of NRR to obtain the NRR selectivity, was investigated by the free energy calculation for *H adsorption on the active sites. The values of calculated free energy change for the adsorption *H (ΔG_{*H}) on the unstrained and strained FeN_4 and FeN_3 sites are given in **Table 6.9**. The DFT calculations predicted that the H atom would be adsorbed on top of the central Fe in the FeN_4 and FeN_3 sites as shown in **Figure 6.23a,b**. The free energy evolution for HER on the FeN_4 and FeN_3 sites (**Figure 6.24a,b**) shows that the compressive strain would cause the free energy change of *H adsorption to be closer to 0 eV, which indicates the competing HER is promoted by compressive strain at these active sites[167]. ΔG_{*H} is predicted to decrease from 0.24

eV on the unstrained FeN_4 site to 0.16 eV on the strained one, while ΔG_{*H} only increases from -0.41 eV on the unstrained FeN_3 site to -0.38 eV on the strained one. It should be noted that the predicted free energy changes ΔG_{*H} for *H adsorption on the unstrained FeN_4 site (0.24 eV) and on the unstrained FeN_3 site (-0.41 eV) are consistent with previous predictions of 0.40 eV on FeN_4 and -0.53 eV on FeN_3.[77, 100]

Table 6.9. Calculated free energy changes as related to NRR selectivity on FeN_4 and FeN_3 sites.

	FeN_4		**FeN_3**	
	Unstrained	**Strained**	**Unstrained**	**Strained**
ΔG_{*H} (eV)	0.24	0.16	-0.41	-0.38
$\Delta G_{*N_2} - \Delta G_{*H}$ (eV)	-0.30	-0.42	-0.45	-0.56
$\Delta G_{*NNH} - \Delta G_{*H}$ (eV)	1.01	0.68	0.37	0.25
$U_{L(NRR)} - U_{L(HER)}$ (V)	-1.07	-0.94	-1.24	-1.18

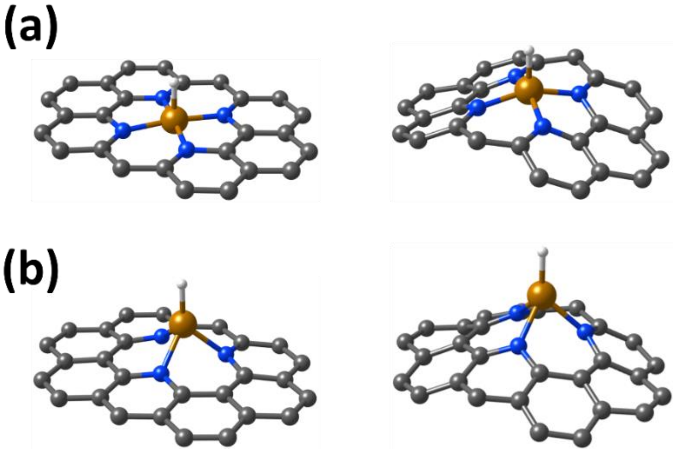

Figure 6.23. Atomic structures of *H adsorption on (a) FeN_4 and (b) FeN_3 sites with and without strain. The gray, blue, white and golden balls represent C, N, H, and Fe atoms, respectively.

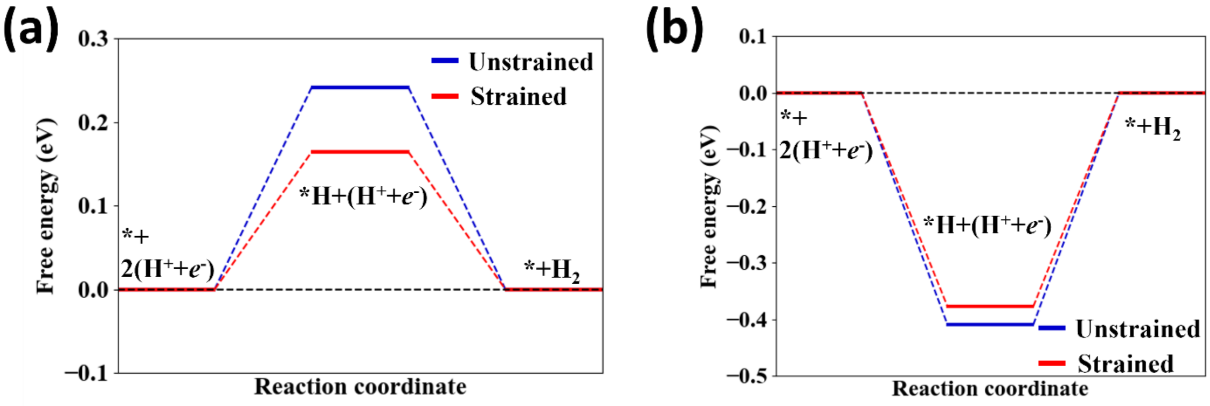

Figure 6.24. Predicted free energy evolution of HER on (a) FeN_4 and (b) FeN_3 active sites with and without strain.

The bonding analysis for the *H adsorption on FeN_4 and FeN_3 sites was also performed to understand the compressive strain effect on the HER activity. Most valence states (below E_F) of *H adsorption are bonding in nature on the strained and unstrained FeN_4 sites, while only a few antibonding states can be found at vicinity below the Fermi level (**Figure 6.25a**). The integrated pCOHP for the Fe-H bonding on the FeN_4 sites decreases from -1.21 eV on unstrained one to -1.25 eV on strained one, which suggests a stronger binding of *H adsorption on the strained FeN_4 sites. In contrast, antibonding states are only visible above the Fermi level for the Fe-H bonding on FeN_3 sites (**Figure 6.25b**). The -pCOHP curves of the strained and unstrained FeN_3 sites are almost identical in the valence bands, and the ICOHP on the strained FeN_3 site only increases less than 0.01 eV as compared to the one on the unstrained FeN_3 site, both implying a very similar binding strength of *H on FeN_3 sites with and without strain.

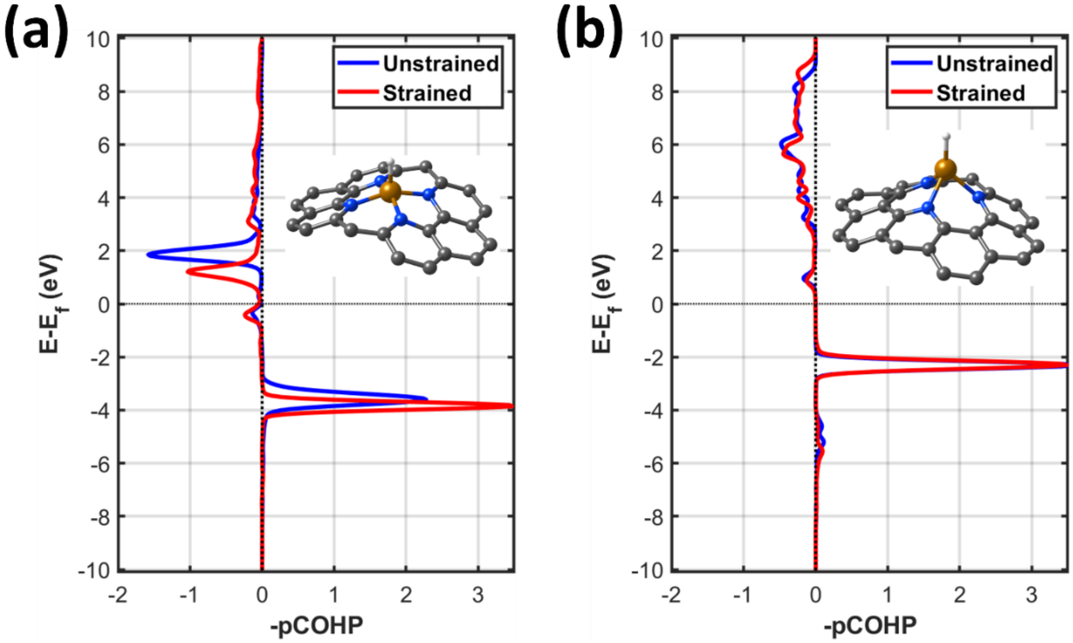

Figure 6.25. -pCOHP analysis results for *H adsorption on (a) FeN_4 and (b) FeN_3 sites.

Regarding the NRR selectivity of catalysts, several computational methods have been employed in previous studies. For example, comparing the adsorption energies of $*N_2$ and *H (i.e., $\Delta G_{*N_2} - \Delta G_{*H}$) on the same active site as a descriptor for the NRR selectivity.[79, 90, 100, 102, 105, 168] If an active site can be preferably occupied by $*N_2$ over *H, the competing HER will be effectively suppressed. Hence, the active sites with more negative value of $\Delta G_{*N_2} - \Delta G_{*H}$, should exhibit better selectivity for NRR over HER. The calculated results in **Table 6.9** indicate that the compressively strained FeN_4 and FeN_3 sites would have a better selectivity towards NRR than the unstrained ones. Some previous studies used the free energy difference between *NNH and *H adsorption (i.e., $\Delta G_{*NNH} - \Delta G_{*H}$) to gauge the NRR selectivity[101], because the hydrogenation step from $*N_2$ to *NNH is the PDS of NRR. Here, *NNH is the preferred adsorbed species over *H for selective NRR. The $\Delta G_{*NNH} - \Delta G_{*H}$ on the compressively strained FeN_4 and FeN_3 sites was predicted to have less-positive values as shown in **Table 6.9,** and thus a better NRR selectivity on the strained sites than on the unstrained ones. In addition, the limiting potential difference between NRR and HER ($U_{L(NRR)} - U_{L(HER)}$) was employed to describe the NRR selectivity.[29, 92, 151] For HER on the FeN_3 sites, which shows a negative free change of *H adsorption, the limiting potential here is defined as the largest electrode potential that can keep the process thermodynamically favorable. The negative value of limiting potential difference shown in **Table 6.9** indicates the HER always have less negative limiting potential than NRR on both FeN_4 and FeN_3 sites, which implies the HER is indeed competitive with the NRR. However, the compressive strain on both FeN_4 and FeN_3 sites leads to a less negative limiting potential difference between the NRR and HER, which indicates a smaller activity difference between NRR and HER on the strained active sites. Thus, the NRR selectivity is enhanced on the compressively strained FeN_4 and FeN_3 sites.

For the calculated values from all the methods listed in **Table 6.9**, the strained FeN_4 sites have a more negative $\Delta G_{*N_2} - \Delta G_{*H}$ by 0.12 eV, a more negative $\Delta G_{*NNH} - \Delta G_{*H}$ by 0.33 eV, and a less negative $U_{L(NRR)} - U_{L(HER)}$ by 0.13 V as compared to the unstrained FeN_4 sites, respectively. In contrast, the strained FeN_3 sites only have a more negative $\Delta G_{*N_2} - \Delta G_{*H}$ by 0.11 eV, a more negative $\Delta G_{*NNH} - \Delta G_{*H}$ by 0.12 eV, and a less negative $U_{L(NRR)} - U_{L(HER)}$ by 0.06 V as compared to the unstrained FeN_3 sites. Therefore, the structural distortion due to compressive strain would have a more pronounced influence on the NRR selectivity on FeN_4 sites than on FeN_3 sites.

6.2.4 Electrochemical Stability of FeN_3 and FeN_4 sites

In electrochemical reaction, a comprehensive understanding of the equilibrium phase in solution can be described as a function of applied potential against the pH value.[182, 183] Such phase stability plot, which is called Pourbaix diagram, can provide relative durability and degradation of intermediate phases during the reaction process.[184, 185, 186] In previous studies for ORR, the stability of intermediate species and active site was predicted using the Pourbaix diagram.[139, 187] Here, the stability of NRR intermediate species in the favored pathway on the FeN_4 and FeN_3 sites was determined by calculating the free energy change using the implicit solvation model and constant potential method.

To include the impact from the applied electrode potential U and the electrolyte pH value, the free energy for each intermediate specie was calculated using equation 5.10 shown in section 5.2 to plot the Pourbaix diagram. The free energy change of each adsorbed specie during the NRR pathway on FeN_4 and FeN_3 sites was calculated using the free energy of pristine active site (i.e., FeN_4 and FeN_3 sites) and final products (i.e., NH_3 molecules) as the reference. Taking the distal pathway for NRR as an example, the free energy change of the NRR intermediate species can be calculated as following

$$\Delta G_{*N_2} = \left(G_{*N_2} + 6G_{[H^+ + e^-]}\right) - \left(G_* + 2G_{NH_3}\right) \tag{6.1}$$

$$\Delta G_{*NNH} = \left(G_{*NNH} + 5G_{[H^+ + e^-]}\right) - \left(G_* + 2G_{NH_3}\right) \tag{6.2}$$

$$\Delta G_{*NNH_2} = \left(G_{*NNH_2} + 4G_{[H^+ + e^-]}\right) - \left(G_* + 2G_{NH_3}\right) \tag{6.3}$$

$$\Delta G_{*N} = \left(G_{*N} + 3G_{[H^+ + e^-]}\right) - \left(G_* + G_{NH_3}\right) \tag{6.4}$$

$$\Delta G_{*NH} = \left(G_{*NH} + 2G_{[H^+ + e^-]}\right) - \left(G_* + G_{NH_3}\right) \tag{6.5}$$

$$\Delta G_{*NH_2} = \left(\Delta G_{*NH_2} + G_{[H^+ + e^-]}\right) - \left(G_* + G_{NH_3}\right) \tag{6.6}$$

$$\Delta G_{*+2NH_3} = \left(G_* + 2G_{NH_3}\right) - \left(G_* + 2G_{NH_3}\right) \tag{6.7}$$

The solvation effect was included using the implicit solvation model as the permittivity of water of 78.4 and a Debye-length of 9.61 Å were used as input parameters for the linearized Poisson-Boltzmann equation. The adsorption of other intermediate species, which are hydrogen (*H) and hydroxyl (*OH), on FeN_3 and FeN_4 sites in the aqueous environment were also included, and the free energy change was calculated using their products as the reference

$$\Delta G_{*H} = \left(G_{*H} + G_{[H^+ + e^-]}\right) - \left(G_* + G_{H_2}\right) \tag{6.8}$$

$$\Delta G_{*OH} = \left(G_{*OH} + G_{[H^+ + e^-]}\right) - \left(G_* + G_{H_2O}\right) \tag{6.9}$$

Hence the competing relation between electrochemical NRR and side reactions (e.g., HER) in aqueous solution could be investigated by free energy comparing. Free energy change calculations were performed for all possible intermediate species by scanning the whole range of potential U and pH value to identify the stable one. Specifically, once an intermediate specie is predicted to be the stable one, its free energy should be lower than any other adjacent species during the pathway for the certain pair of U and pH value.

The Pourbaix diagrams that predicted from calculated free energy results for stable intermediate species on FeN_4 and FeN_3 sites are shown in **Figure 6.26**. The intermediate species in the aqueous solution is included here. The colored regions in the Pourbaix diagram represent the most stable intermediate species within the range of potential U and pH value. The boundaries between regions indicates the equilibrium state of the intermediate species on the two sides. In the predicted Pourbaix diagram for the FeN_4 site (**Figure 6.26a**), there are only three electrochemically stable intermediate species presented. The $*N_2$ and *H adsorption occupy the upper right and lower left regions in the constructed Pourbaix diagram which are shown as the two main intermediate species for electrochemical NRR on the FeN_4 site in aqueous solution. A small bar exists between the blue and yellow region which represents the stable *OH adsorption on the FeN_4 site. In the constructed Pourbaix diagram of stable intermediate species on the FeN_3 site (**Figure 6.26b**), the $*N_2$ and *H adsorption also occupy two separated regions in the diagram with a narrow bar in between for the stable *OH adsorption. Consequently, during the electrochemical NRR process on FeN_4 and FeN_3 sites in aqueous solution, the major competition was predicted to be the stable adsorption of $*N_2$ and *H on the active site which would lead to NRR and HER, respectively.

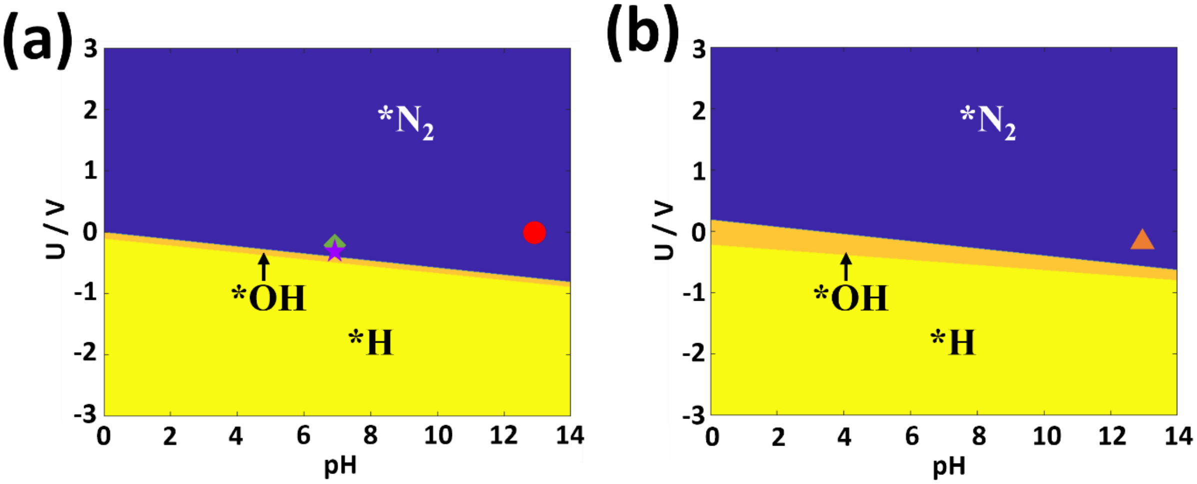

Figure 6.26. Predicted Pourbaix diagram for all intermediate species on (a) FeN_4 and (b) FeN_3 sites in aqueous solution. The optimal U and pH values from experimental studies are shown as star[150], rhombus[81], circle[99], and triangle[77] marks in the plots.

Since the stable adsorption of $*N_2$ is essential for NRR to occur on the active site, the potential U and pH value of the blue region shown in **Figure 6.26** was predicted to be the window for electrochemical NRR with suppressed HER in aqueous solution. To validate the predicted

Pourbaix diagram for electrochemical NRR in aqueous solution, the experimental observations from previous studies were compared with the predicted region for feasible NRR. The marks shown in **Figure 6.26a,b** are the experimental results of optimal potential U and pH values for NRR to obtain the highest FE and NH_3 yield rate. The star mark represents a study for NRR on the ISAS-Fe/NC catalysts with FeN_4 site which exhibited an optimal potential U and pH value of -0.40 V and 7, respectively.[150] The rhombus mark that close to the star mark represents a study for FeN_4 site with the optimal potential U and pH value of -0.30 V and 7, respectively.[81] In the predicted Pourbaix diagram for FeN_4 site (**Figure 6.26a)**, the boundary between $*N_2$ and *OH adsorption for pH = 7 was predicted to be -0.45 V. Hence, the electrochemical NRR was predicted to suppress HER in aqueous solution with applied electrode potential more positive than -0.45 V, which agrees with the experimental observed optimal conditions for NRR. The red circle is a study for NRR on FeN_4 sites with the optimal potential U and pH value of 0 V and 13, respectively.[99] In the predicted Pourbaix diagram shown in **Figure 6.26a**, the boundary for stable $*N_2$ adsorption for pH = 13 was predicted to be more positive than -0.79 V, which also agrees the experimental observation. The predicted boundary for $*N_2$ adsorption on FeN_3 site with pH = 13 was predicted to be higher than -0.57 V, which agrees with the experimental observed optimal potential U of -0.2 V and pH=13 for NRR shown as the triangle mark in **Figure 6.26b**.[77] Furthermore, although a higher potential than the boundary value between $*N_2$ and *OH adsorption would lead to a prevailing NRR, a too high applied potential would result in a too strong $*N_2$ adsorption which could in turn hinder NRR on the active site. It is also the reason for the observed optimal pairs of potential U and pH value were only found near the $*N_2$/*OH boundary. Therefore, the predicted Pourbaix diagram for stable intermediate species on FeN_4 and FeN_3 sites well demonstrated the experimental observed optimal condition for NRR on the Fe-N-C catalysts.

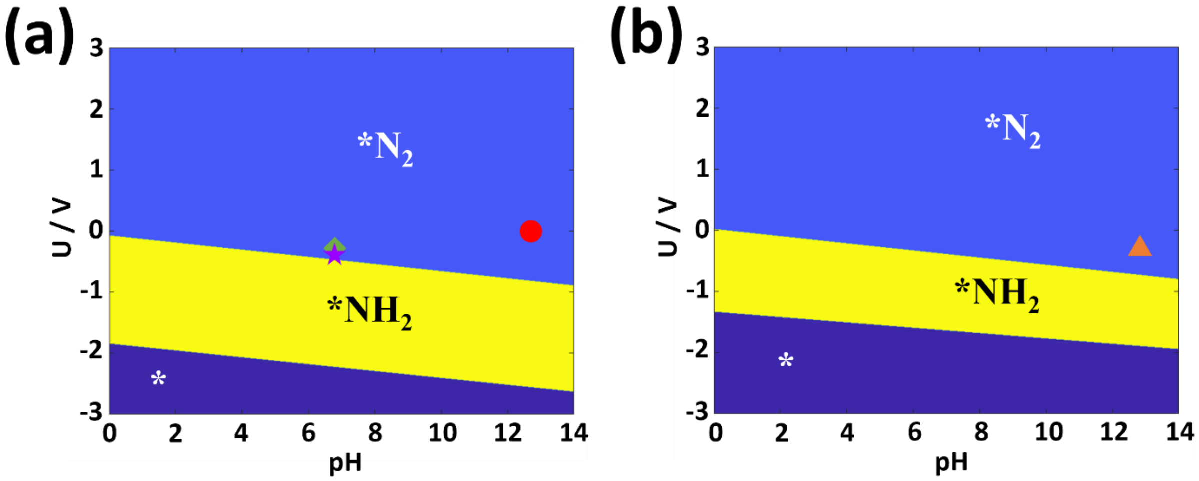

Figure 6.27. Predicted Pourbaix diagram for NRR intermediate species adsorption on (a) FeN_4 and (b) FeN_3 sites. The optimal U and pH values from experimental studies are shown as star[150], rhombus[81], circle[99], and triangle[77] marks in the plots.

Furthermore, the predicted Pourbaix diagram was also used to investigate the potential trap specie in the NRR pathway. Consequently, the adsorption of *H and *OH were excluded here. In the predicted Pourbaix diagram for NRR intermediate species only, three stable species were found which are the *N_2 adsorption, *NH_2 adsorption, and the clean surface *. In the region for stable *N_2 adsorption, there would be no trap state during the pathway once the NRR occurs on the active site. For the potential U and pH value in the *NH_2 region, the initial adsorption of *N_2 is not favored, and the reaction would be trapped at state of *NH_2 adsorption. The region of clean surface * in the Pourbaix diagram indicates no intermediate specie adsorption is favored in such range of potential U and pH value. As shown in **Figure 6.27**, all the optimal pairs of potential U and pH value for NRR that observed in experiments were also found in the region of stable *N_2 adsorption.

Hence, the Pourbaix diagram that was calculated using the implicit solvation model and constant potential method in this section well demonstrated the experimental observed optimal conditions for NRR on the FeN_4 and FeN_3 sites. Such computational method for constructing the Pourbaix diagram for electrochemical NRR is proved to be able to predict the electrochemical stability of Fe-N-C catalysts.

7.0 Conclusions and Prospects

In this dissertation, the electrochemical NRR activity and selectivity of M-N-C (M=Fe, Co, and Ni) catalysts were studied using the first-principles density functional theory (DFT) calculations. The correlation between chemical environment and NRR performance of MN_xC_y active sites were investigated. The influence of compressive strain on the NRR performance was investigated in Fe-N-C catalysts with structural distortion. The electrochemical stability of FeN_3 and FeN_4 sites was predicted for electrochemical NRR in aqueous solution. Specifically, forty-five types of FeN_xC_y, CoN_xC_y, and NiN_xC_y (x varies from 1 to 4, y varies from 1 to 3) active sites were modeled for investigating the effects of local structure and active site configuration of active site to the NRR activity and selectivity. Then, the NRR activity and selectivity of unstrained and strained Fe-N-C catalysts were calculated and compared to reveal the effects of structural distortion on NRR performance. Finally, the Pourbaix diagram was calculated by free energy calculations of NRR intermediate species to predict the electrochemical stability of FeN_4 and FeN_3 sites as a function of potential U and pH value and compared with experimental results to validate it.

In summary, the main outcomes of this dissertation can be concluded as follows:

1. For both fully embedded and edge-to-edge MN_xC_y sites, the increasing number of N atoms doped in the active site moiety results in a stabler active site in the graphene layer. Active sites with low formation energy are expected to show a high density in catalysts. The fully embedded FeN_4, CoN_4, and NiN_4 sites are the most stable active

site in Fe-N-C, Co-N-C, and Ni-N-C catalysts with lowest formation energy, respectively. The formation of edge-to-edge MN_xC_y sites requires a proper pore structure in graphene as the precondition, which leads to low density of such MN_xC_y sites in M-N-C catalysts.

2. The adsorption of $*N_2$ on the MN_xC_y site depends on the doped metal atom and configuration of active site moiety. $*N_2$ adsorption is thermodynamically favored on all FeN_xC_y and most CoN_xC_y sites, whereas it is not favorable on NiN_xC_y sites The NiN_3 site is the only configuration in Ni-N-C catalysts exhibits negative adsorption energy for $*N_2$. The fully embedded MN_xC_y sites with the central metal atom in a single vacancy site exhibit better properties for $*N_2$ adsorption than other active site configurations.

   The electron accumulation on top of the central metal atom is necessary for thermodynamically favorable $*N_2$ adsorption. Such electron accumulation promotes the binding strength of $*N_2$ by a strong transferring of *d*-orbital electrons to the empty π*-orbital of $*N_2$ which also activates the inert N≡N bond.
3. The FeN_xC_y sites exhibit better NRR activity and selectivity than both CoN_xC_y and NiN_xC_y sites. The FeN_3C_1 site has the best NRR activity with the most positive NRR limiting potential of -0.74 V, and the best selectivity among all the sites examined. The predicted NRR limiting potential of NiN_3 site shows the value of -0.83 V, which is in good agreement with the experimentally observed optimal potential of -0.80 V for NRR on Ni-N-C catalysts.
4. The structural distortion in Fe-N-C catalysts which is simulated by the compressive strain in FeN_4 and FeN_3 sites results in a non-planar configuration in graphene. The

NRR activity of compressively strained FeN_4 and FeN_3 sites are enhanced by the structural distortion. The NRR limiting potential of strained FeN_4 and FeN_3 sites exhibits positive change of 0.21 V and 0.03 V as compared to the unstrained ones, respectively. The stronger binding of *NNH on the strained active sites is revealed by chemical bonding analysis. The stronger binding of *NNH results in a lower free energy increase in the first hydrogenation step, which is also the potential determining step, and hence enhances the NRR activity. The compressive strain in Fe-N-C catalysts has more effects on NRR activity of FeN_4 sites than that of FeN_3 sites.

5. The NRR selectivity of FeN_4 and FeN_3 sites is also enhanced by the compressive strain, which is demonstrated by three different examine methods. A larger selectivity enhancement by compressive strain is also uncovered on FeN_4 sites than on FeN_3 sites.
6. The electrochemical stability of FeN_4 and FeN_3 sites for NRR in aqueous solution is predicted as a function of applied electrode potential and electrolyte pH value. The calculated Pourbaix diagram well explains the experimentally observed optimal condition for NRR. Thus, such computational method for predicting electrochemical stability of catalysts is validated.

Therefore, this study provides insights for the relation between chemical environment and catalytic performance of NRR active sites, the beneficial effect of structural distortion in M-N-C catalysts for NRR, and a computational approach to predict the electrochemical stability of M-N-C catalysts. It is expected that this study will also provide guidance to the rational design and synthesis of high-performance M-N-C catalysts for electrochemical NRR.

Many challenges are remained for better computational investigation and design for NRR electrocatalysts. The big discrepancy between DFT predicted results and experimentally observed results urges more accurate computational methods and procedures. Although we have shown that implicit solvation model and constant potential method can help shrink such gap, more efforts are needed. There are many choices, such as the DFT+U, hybrid functionals, and the microkinetic model, that can lead us to a more accurate computational result. For example, the DFT+U method was adopted in previous studies for ORR on Co-N-C catalysts[188] and CO2RR on Fe-N-C catalysts[189] to avoid the artificial energy incorrection arises from d-orbital electrons self-interaction in transition metal atom. Specifically, the comparison between RPBE and RPBE+U for CO2RR on Fe-N-C catalysts shows a better estimation for intermediate specie binding energy with the help of U correction.[189] In addition, the advantages of hybrid functionals in predicting more accurate binding energy and magnetic moment of *COOH and *CO on Fe-N-C catalysts were also demonstrated by the same study.[189] Especially, hybrid functionals were shown beneficial for the better prediction of desorption energy of *CO on Fe-N-C catalysts, which is always overestimated by PBE functionals. Therefore, it is expectable that the application of DFT+U and hybrid functionals for computational studies on NRR will also lead to more accurate results to reduce the discrepancy between theoretical predictions and experimental observations. However, these approaches require much more computational resources, for which a more advanced computer or program architecture will be significantly helpful. Furthermore, the better description of the interface structure between electrolyte and electrode, and the mixture of electrolyte ions will also promote the computational prediction for the electrochemical NRR performance of catalysts. The progresses of all these technologies are not only beneficial for the development of NRR catalysts, but also advantageous for the advances of the electrocatalysis field.

Bibliography

1. Smil V. Detonator of the population explosion. *Nature* 1999, **400**(6743)**:** 415.

2. Shipman MA, Symes MD. Recent progress towards the electrosynthesis of ammonia from sustainable resources. *Catalysis Today* 2017, **286:** 57-68.

3. Chen GF, Ren S, Zhang L, Cheng H, Luo Y, Zhu K, *et al.* Advances in electrocatalytic N_2 reduction—strategies to tackle the selectivity challenge. *Small Methods* 2019, **3**(6)**:** 1800337.

4. Giddey S, Badwal SPS, Kulkarni A. Review of electrochemical ammonia production technologies and materials. *International Journal of Hydrogen Energy* 2013, **38**(34)**:** 14576-14594.

5. Survey USG. NITROGEN (FIXED)—AMMONIA: U.S. Geological Survey; 2019.

6. Wilkinson I. Siemens green Ammonia. 1st NH3 European event; 2017.

7. Chen JG, Crooks RM, Seefeldt LC, Bren KL, Bullock RM, Darensbourg MY*, et al.* Beyond fossil fuel–driven nitrogen transformations. *Science* 2018, **360**(6391)**:** eaar6611.

8. Pool JA, Lobkovsky E, Chirik PJ. Hydrogenation and cleavage of dinitrogen to ammonia with a zirconium complex. *Nature* 2004, **427**(6974)**:** 527.

9. Cui X, Tang C, Zhang Q. A review of electrocatalytic reduction of dinitrogen to ammonia under ambient conditions. *Advanced Energy Materials* 2018, **8**(22)**:** 1800369.

10. Liu H. Ammonia synthesis catalyst 100 years: Practice, enlightenment and challenge. *Chinese journal of catalysis* 2014, **35**(10)**:** 1619-1640.

11. Rafiqul I, Weber C, Lehmann B, Voss A. Energy efficiency improvements in ammonia production—perspectives and uncertainties. *Energy* 2005, **30**(13)**:** 2487-2504.

12. Lide DR. *CRC handbook of chemistry and physics*, vol. 85. CRC press, 2004.

13. Nielsen A. Review of ammonia catalysis. *Catalysis Reviews* 1971, **4**(1)**:** 1-26.

14. Aika K-i, Hori H, Ozaki A. Activation of nitrogen by alkali metal promoted transition metal I. Ammonia synthesis over ruthenium promoted by alkali metal. *Journal of Catalysis* 1972, **27**(3)**:** 424-431.

15. Aika K-i, Christiansen L, Dybkjaer I, Hansen J, Nielsen PH, Nielsen A, *et al. Ammonia: catalysis and manufacture*. Springer Science & Business Media, 2012.

16. Vojvodic A, Medford AJ, Studt F, Abild-Pedersen F, Khan TS, Bligaard T, *et al.* Exploring the limits: a low-pressure, low-temperature Haber–Bosch process. *Chemical Physics Letters* 2014, **598:** 108-112.

17. Van der Ham CJ, Koper MT, Hetterscheid DG. Challenges in reduction of dinitrogen by proton and electron transfer. *Chemical Society Reviews* 2014, **43**(15)**:** 5183-5191.

18. Burgess BK, Lowe DJ. Mechanism of molybdenum nitrogenase. *Chemical reviews* 1996, **96**(7)**:** 2983-3012.

19. Seefeldt LC, Hoffman BM, Dean DR. Mechanism of Mo-dependent nitrogenase. *Annual review of biochemistry* 2009, **78:** 701-722.

20. Chatt J, Dilworth JR, Richards RL. Recent advances in the chemistry of nitrogen fixation. *Chemical reviews* 1978, **78**(6)**:** 589-625.

21. Yandulov DV, Schrock RR. Reduction of dinitrogen to ammonia at a well-protected reaction site in a molybdenum triamidoamine complex. *Journal of the American Chemical Society* 2002, **124**(22)**:** 6252-6253.

22. Yandulov DV, Schrock RR. Catalytic reduction of dinitrogen to ammonia at a single molybdenum center. *Science* 2003, **301**(5629)**:** 76-78.

23. Yandulov DV, Schrock RR. Studies relevant to catalytic reduction of dinitrogen to ammonia by molybdenum triamidoamine complexes. *Inorganic chemistry* 2005, **44**(4)**:** 1103-1117.

24. Lee Y, Mankad NP, Peters JC. Triggering N 2 uptake via redox-induced expulsion of coordinated NH 3 and N 2 silylation at trigonal bipyramidal iron. *Nature chemistry* 2010, **2**(7)**:** 558.

25. Schrock RR. Catalytic reduction of dinitrogen to ammonia at well-defined single metal sites. *Philosophical Transactions of the Royal Society A* 2005, **363**(1829)**:** 959-969.

26. Kitano M, Inoue Y, Yamazaki Y, Hayashi F, Kanbara S, Matsuishi S, *et al.* Ammonia synthesis using a stable electride as an electron donor and reversible hydrogen store. *Nature Chemistry* 2012, **4**(11)**:** 934.

27. Song P, Wang H, Kang L, Ran B, Song H, Wang R. Electrochemical nitrogen reduction to ammonia at ambient conditions on nitrogen and phosphorus co-doped porous carbon. *Chemical Communications* 2019, **55**(5)**:** 687-690.

28. Rod TH, Logadottir A, Nørskov JK. Ammonia synthesis at low temperatures. *The Journal of Chemical Physics* 2000, **112**(12)**:** 5343-5347.

29. Montoya JH, Tsai C, Vojvodic A, Nørskov JK. The challenge of electrochemical ammonia synthesis: A new perspective on the role of nitrogen scaling relations. *ChemSusChem* 2015, **8**(13)**:** 2180-2186.

30. Guo C, Ran J, Vasileff A, Qiao S-Z. Rational design of electrocatalysts and photo (electro) catalysts for nitrogen reduction to ammonia (NH_3) under ambient conditions. *Energy & Environmental Science* 2018, **11**(1)**:** 45-56.

31. Bao D, Zhang Q, Meng FL, Zhong HX, Shi MM, Zhang Y*, et al.* Electrochemical reduction of N_2 under ambient conditions for artificial N_2 fixation and renewable energy storage using N_2/NH_3 cycle. *Advanced Materials* 2017, **29**(3)**:** 1604799.

32. Lan R, Irvine JT, Tao S. Synthesis of ammonia directly from air and water at ambient temperature and pressure. *Scientific Reports* 2013, **3**(1)**:** 1-7.

33. Kordali V, Kyriacou G, Lambrou C. Electrochemical synthesis of ammonia at atmospheric pressure and low temperature in a solid polymer electrolyte cell. *Chemical Communications* 2000(17)**:** 1673-1674.

34. Sclafani A, Augugliaro V, Schiavello M. Dinitrogen electrochemical reduction to ammonia over Iron cathode in aqueous medium. *Journal of The Electrochemical Society* 1983, **130**(3)**:** 734-736.

35. Kim K, Yoo C-Y, Kim J-N, Yoon HC, Han J-I. Electrochemical synthesis of ammonia from water and nitrogen in ethylenediamine under ambient temperature and pressure. *Journal of the Electrochemical Society* 2016, **163**(14)**:** F1523-F1526.

36. Tsuneto A, Kudo A, Sakata T. Lithium-mediated electrochemical reduction of high pressure N2 to NH3. *Journal of Electroanalytical Chemistry* 1994, **367**(1-2)**:** 183-188.

37. Honkala K, Hellman A, Remediakis I, Logadottir A, Carlsson A, Dahl S*, et al.* Ammonia synthesis from first-principles calculations. *science* 2005, **307**(5709)**:** 555-558.

38. Skulason E, Bligaard T, Gudmundsdóttir S, Studt F, Rossmeisl J, Abild-Pedersen F*, et al.* A theoretical evaluation of possible transition metal electro-catalysts for N_2 reduction. *Physical Chemistry Chemical Physics* 2012, **14**(3)**:** 1235-1245.

39. Köleli F, Röpke T. Electrochemical hydrogenation of dinitrogen to ammonia on a polyaniline electrode. *Applied Catalysis B: Environmental* 2006, **62**(3-4)**:** 306-310.

40. Köleli F, Kayan DB. Low overpotential reduction of dinitrogen to ammonia in aqueous media. *Journal of Electroanalytical Chemistry* 2010, **638**(1)**:** 119-122.

41. Gong K, Du F, Xia Z, Durstock M, Dai L. Nitrogen-doped carbon nanotube arrays with high electrocatalytic activity for oxygen reduction. *science* 2009, **323**(5915)**:** 760-764.

42. Qu L, Liu Y, Baek J-B, Dai L. Nitrogen-doped graphene as efficient metal-free electrocatalyst for oxygen reduction in fuel cells. *ACS nano* 2010, **4**(3)**:** 1321-1326.

43. Song P, Kang L, Wang H, Guo R, Wang R. Nitrogen (N), Phosphorus (P)-Codoped Porous Carbon as a Metal-Free Electrocatalyst for N2 Reduction under Ambient Conditions. *ACS applied materials & interfaces* 2019, **11**(13)**:** 12408-12414.

44. Sorokin AB. Phthalocyanine metal complexes in catalysis. *Chemical reviews* 2013, **113**(10)**:** 8152-8191.

45. Seh ZW, Kibsgaard J, Dickens CF, Chorkendorff I, Nørskov JK, Jaramillo TF. Combining theory and experiment in electrocatalysis: Insights into materials design. *Science* 2017, **355**(6321)**:** eaad4998.

46. Liu X, Jiao Y, Zheng Y, Jaroniec M, Qiao S-Z. Building up a picture of the electrocatalytic nitrogen reduction activity of transition metal single-atom catalysts. *Journal of the American Chemical Society* 2019, **141**(24)**:** 9664-9672.

47. Lancaster KM, Roemelt M, Ettenhuber P, Hu Y, Ribbe MW, Neese F, *et al.* X-ray emission spectroscopy evidences a central carbon in the nitrogenase iron-molybdenum cofactor. *Science* 2011, **334**(6058)**:** 974-977.

48. Spatzal T, Aksoyoglu M, Zhang L, Andrade SL, Schleicher E, Weber S, *et al.* Evidence for interstitial carbon in nitrogenase FeMo cofactor. *Science* 2011, **334**(6058)**:** 940-940.

49. Nelson DL, Lehninger AL, Cox MM. *Lehninger principles of biochemistry*. Macmillan, 2008.

50. Wherland S, Burgess BK, Stiefel EI, Newton WE. Nitrogenase reactivity: effects of component ratio on electron flow and distribution during nitrogen fixation. *Biochemistry* 1981, **20**(18)**:** 5132-5140.

51. Singh AR, Rohr BA, Schwalbe JA, Cargnello M, Chan K, Jaramillo TF, *et al.* Electrochemical Ammonia Synthesis-The Selectivity Challenge. *ACS Catalysis* 2017, **7**(1)**:** 706-709.

52. Li X-F, Li Q-K, Cheng J, Liu L, Yan Q, Wu Y, *et al.* Conversion of dinitrogen to ammonia by FeN_3-embedded graphene. *Journal of the American Chemical Society* 2016, **138**(28)**:** 8706-8709.

53. Hinnemann B, Nørskov JK. Chemical activity of the nitrogenase FeMo cofactor with a central nitrogen ligand: density functional study. *Journal of the American Chemical Society* 2004, **126**(12)**:** 3920-3927.

54. Barney BM, Lukoyanov D, Yang T-C, Dean DR, Hoffman BM, Seefeldt LC. A methyldiazene (HN=N-CH_3)-derived species bound to the nitrogenase active-site FeMo cofactor: Implications for mechanism. *Proceedings of the National Academy of Sciences of the United States of America* 2006, **103**(46)**:** 17113-17118.

55. Knözinger H, Weitkamp J. Handbook of Heterogeneous Catalysis: Volume 3. Wiley-VCH; 1997.

56. Jacobsen CJ, Dahl S, Clausen BS, Bahn S, Logadottir A, Nørskov JK. Catalyst design by interpolation in the periodic table: bimetallic ammonia synthesis catalysts. *Journal of the American Chemical Society* 2001, **123**(34)**:** 8404-8405.

57. Bligaard T, Nørskov JK, Dahl S, Matthiesen J, Christensen CH, Sehested J. The Brønsted–Evans–Polanyi relation and the volcano curve in heterogeneous catalysis. *Journal of catalysis* 2004, **224**(1)**:** 206-217.

58. Schlögl R, Jennings J. Catalytic Ammonia Synthesis. *Fundamentals and Practice*. Plenum Press New York, 1991, pp 19-108.

59. Ozaki A. Catalystic Activation of Dinitrogen, Chap. 3. *Catalysis, science and technology* 1981, **1**.

60. Logadottir A, Rod TH, Nørskov JK, Hammer B, Dahl S, Jacobsen C. The Brønsted–Evans–Polanyi relation and the volcano plot for ammonia synthesis over transition metal catalysts. *Journal of Catalysis* 2001, **197**(2)**:** 229-231.

61. Furuya N, Yoshiba H. Electroreduction of nitrogen to ammonia on gas-diffusion electrodes loaded with inorganic catalyst. *Journal of Electroanalytical Chemistry and Interfacial Electrochemistry* 1990, **291**(1-2)**:** 269-272.

62. Diekhöner L, Mortensen H, Baurichter A, Luntz A. Laser assisted associative desorption of N_2 and CO from Ru (0001). *The Journal of Chemical Physics* 2001, **115**(7)**:** 3356-3373.

63. Lan R, Tao S. Electrochemical synthesis of ammonia directly from air and water using a $Li^+/H^+/NH_4^+$ mixed conducting electrolyte. *RSC Advances* 2013, **3**(39)**:** 18016-18021.

64. Li SJ, Bao D, Shi MM, Wulan BR, Yan JM, Jiang Q. Amorphizing of Au nanoparticles by CeOx–RGO hybrid support towards highly efficient electrocatalyst for N_2 reduction under ambient conditions. *Advanced Materials* 2017, **29**(33)**:** 1700001.

65. Shi MM, Bao D, Wulan BR, Li YH, Zhang YF, Yan JM, *et al.* Au sub-nanoclusters on TiO_2 toward highly efficient and selective electrocatalyst for N_2 conversion to NH_3 at ambient conditions. *Advanced Materials* 2017, **29**(17)**:** 1606550.

66. Kim K, Lee N, Yoo C-Y, Kim J-N, Yoon HC, Han J-I. Communication—electrochemical reduction of nitrogen to ammonia in 2-propanol under ambient temperature and pressure. *Journal of the Electrochemical Society* 2016, **163**(7)**:** F610-F612.

67. Yang D, Chen T, Wang Z. Electrochemical reduction of aqueous nitrogen (N_2) at a low overpotential on (110)-oriented Mo nanofilm. *Journal of Materials Chemistry A* 2017, **5**(36)**:** 18967-18971.

68. Han J, Ji X, Ren X, Cui G, Li L, Xie F, *et al.* MoO 3 nanosheets for efficient electrocatalytic N 2 fixation to NH 3. *Journal of Materials Chemistry A* 2018, **6**(27)**:** 12974-12977.

69. Zhang L, Ji X, Ren X, Luo Y, Shi X, Asiri AM, *et al.* Efficient electrochemical N2 reduction to NH3 on MoN nanosheets array under ambient conditions. *ACS Sustainable Chemistry & Engineering* 2018, **6**(8)**:** 9550-9554.

70. Zhang L, Ji X, Ren X, Ma Y, Shi X, Tian Z, *et al.* Electrochemical ammonia synthesis via nitrogen reduction reaction on a MoS_2 catalyst: theoretical and experimental studies. *Advanced Materials* 2018, **30**(28)**:** 1800191.

71. Lv C, Yan C, Chen G, Ding Y, Sun J, Zhou Y, *et al.* An Amorphous Noble-Metal-Free Electrocatalyst that Enables Nitrogen Fixation under Ambient Conditions. *Angewandte Chemie International Edition* 2018, **57**(21)**:** 6073-6076.

72. Yang X, Li K, Cheng D, Pang W-L, Lv J, Chen X, *et al.* Nitrogen-doped porous carbon: Highly efficient trifunctional electrocatalyst for oxygen reversible catalysis and nitrogen reduction reaction. *Journal of Materials Chemistry A* 2018, **6**(17)**:** 7762-7769.

73. Mukherjee S, Cullen DA, Karakalos S, Liu K, Zhang H, Zhao S, *et al.* Metal-organic framework-derived nitrogen-doped highly disordered carbon for electrochemical ammonia synthesis using N2 and H2O in alkaline electrolytes. *Nano Energy* 2018, **48:** 217-226.

74. Liu Y, Su Y, Quan X, Fan X, Chen S, Yu H, *et al.* Facile Ammonia Synthesis from Electrocatalytic N2 Reduction under Ambient Conditions on N-Doped Porous Carbon. *ACS Catalysis* 2018.

75. Furuya N, Yoshiba H. Electroreduction of nitrogen to ammonia on gas-diffusion electrodes modified by Fe-phthalocyanine. *Journal of Electroanalytical Chemistry and Interfacial Electrochemistry* 1989, **263**(1)**:** 171-174.

76. Furuya N, Yoshiba H. Electroreduction of nitrogen to ammonia on gas-diffusion electrodes modified by metal phthalocyanines. *Journal of electroanalytical chemistry and interfacial electrochemistry* 1989, **272**(1-2)**:** 263-266.

77. Wang Y, Cui X, Zhao J, Jia G, Gu L, Zhang Q, *et al.* Rational Design of Fe–N/C Hybrid for Enhanced Nitrogen Reduction Electrocatalysis under Ambient Conditions in Aqueous Solution. *ACS Catalysis* 2019, **9**(1)**:** 336-344.

78. Geng Z, Liu Y, Kong X, Li P, Li K, Liu Z, *et al.* Achieving a Record-High Yield Rate of 120.9 for N_2 Electrochemical Reduction over Ru Single-Atom Catalysts. *Advanced Materials* 2018, **30**(40)**:** 1803498.

79. Tao H, Choi C, Ding L-X, Jiang Z, Han Z, Jia M, *et al.* Nitrogen fixation by Ru single-atom electrocatalytic reduction. *Chem* 2019, **5**(1)**:** 204-214.

80. Mukherjee S, Yang X, Shan W, Samarakoon W, Karakalos S, Cullen DA, *et al.* Atomically dispersed single Ni site catalysts for nitrogen reduction toward electrochemical ammonia synthesis using N_2 and H_2O. *Small Methods* 2020, **4**(6)**:** 1900821.

81. Yang X, Sun S, Meng L, Li K, Mukherjee S, Chen X, *et al.* Molecular single iron site catalysts for electrochemical nitrogen fixation under ambient conditions. *Applied Catalysis B: Environmental* 2021, **285:** 119794.

82. Cong M, Chen X, Xia K, Ding X, Zhang L, Jin Y, *et al.* Selective nitrogen reduction to ammonia on iron porphyrin-based single-site metal–organic frameworks. *J Mater Chem A* 2021, **9**(8)**:** 4673-4678.

83. Li Y, Li J, Huang J, Chen J, Kong Y, Yang B, *et al.* Boosting Electroreduction Kinetics of Nitrogen to Ammonia via Tuning Electron Distribution of Single-Atomic Iron Sites. *Angewandte Chemie International Edition* 2021, **60**(16)**:** 9078-9085.

84. Qu X, Shen L, Mao Y, Lin J, Li Y, Li G, *et al.* Facile Preparation of Carbon Shells-Coated O-Doped Molybdenum Carbide Nanoparticles as High Selective Electrocatalysts for Nitrogen Reduction Reaction under Ambient Conditions. *ACS Applied Materials & Interfaces* 2019, **11**(35)**:** 31869-31877.

85. Wang H, Wang L, Wang Q, Ye S, Sun W, Shao Y, *et al.* Ambient electrosynthesis of ammonia: electrode porosity and composition engineering. *Angewandte Chemie International Edition* 2018, **57**(38)**:** 12360-12364.

86. Yu X, Han P, Wei Z, Huang L, Gu Z, Peng S, *et al.* Boron-doped graphene for electrocatalytic N2 reduction. *Joule* 2018, **2**(8)**:** 1610-1622.

87. Chen C, Yan D, Wang Y, Zhou Y, Zou Y, Li Y, *et al.* B□ N Pairs Enriched Defective Carbon Nanosheets for Ammonia Synthesis with High Efficiency. *Small* 2019, **15**(7)**:** 1805029.

88. Xia L, Yang J, Wang H, Zhao R, Chen H, Fang W, *et al.* Sulfur-doped graphene for efficient electrocatalytic N 2-to-NH 3 fixation. *Chemical communications* 2019, **55**(23)**:** 3371-3374.

89. Hao Y-C, Guo Y, Chen L-W, Shu M, Wang X-Y, Bu T-A, *et al.* Promoting nitrogen electroreduction to ammonia with bismuth nanocrystals and potassium cations in water. *Nature Catalysis* 2019, **2**(5)**:** 448-456.

90. Choi C, Back S, Kim N-Y, Lim J, Kim Y-H, Jung Y. Suppression of Hydrogen Evolution Reaction in Electrochemical N_2 Reduction Using Single-Atom Catalysts: A Computational Guideline. *ACS Catalysis* 2018, **8**(8)**:** 7517-7525.

91. Zhang L, Sharada SM, Singh AR, Rohr BA, Su Y, Qiao L, *et al.* A theoretical study of the effect of a non-aqueous proton donor on electrochemical ammonia synthesis. *Physical Chemistry Chemical Physics* 2018, **20**(7)**:** 4982-4989.

92. Singh AR, Rohr BA, Statt MJ, Schwalbe JA, Cargnello M, Nørskov JK. Strategies toward selective electrochemical ammonia synthesis. *ACS Catalysis* 2019, **9**(9)**:** 8316-8324.

93. Bouwkamp-Wijnoltz A, Visscher W, Van Veen J, Boellaard E, Van der Kraan A, Tang S. On active-site heterogeneity in pyrolyzed carbon-supported iron porphyrin catalysts for the electrochemical reduction of oxygen: an in situ mössbauer study. *The Journal of Physical Chemistry B* 2002, **106**(50)**:** 12993-13001.

94. Lefèvre M, Proietti E, Jaouen F, Dodelet J-P. Iron-based catalysts with improved oxygen reduction activity in polymer electrolyte fuel cells. *science* 2009, **324**(5923)**:** 71-74.

95. Calle-Vallejo F, Martinez JI, Rossmeisl J. Density functional studies of functionalized graphitic materials with late transition metals for oxygen reduction reactions. *Physical Chemistry Chemical Physics* 2011, **13**(34)**:** 15639-15643.

96. Yu L, Pan X, Cao X, Hu P, Bao X. Oxygen reduction reaction mechanism on nitrogen-doped graphene: A density functional theory study. *Journal of catalysis* 2011, **282**(1)**:** 183-190.

97. Kattel S, Wang G. Reaction pathway for oxygen reduction on FeN4 embedded graphene. *The journal of physical chemistry letters* 2014, **5**(3)**:** 452-456.

98. Liu K, Wu G, Wang G. Role of Local Carbon Structure Surrounding FeN4 Sites in Boosting the Catalytic Activity for Oxygen Reduction. *The Journal of Physical Chemistry C* 2017, **121**(21)**:** 11319-11324.

99. Wang M, Liu S, Qian T, Liu J, Zhou J, Ji H, *et al.* Over 56.55% Faradaic efficiency of ambient ammonia synthesis enabled by positively shifting the reaction potential. *Nature Communications* 2019, **10**(1)**:** 341.

100. Yang Y, Liu J, Wei Z, Wang S, Ma J. Transition metal-dinitrogen complex embedded graphene for nitrogen reduction reaction. *ChemCatChem* 2019, **11**(12)**:** 2821-2827.

101. Zhao W, Zhang L, Luo Q, Hu Z, Zhang W, Smith S, *et al.* Single $Mo_1(Cr_1)$ Atom on Nitrogen-Doped Graphene Enables Highly Selective Electroreduction of Nitrogen into Ammonia. *ACS Catalysis* 2019, **9**(4)**:** 3419-3425.

102. Guo Y, Wang G, Shen S, Wei G, Xia G, Zhang J. On scaling relations of single atom catalysts for electrochemical ammonia synthesis. *Applied Surface Science* 2021, **550:** 149283.

103. Guo X, Gu J, Hu X, Zhang S, Chen Z, Huang S. Coordination Tailoring Towards Efficient Single-Atom Catalysts for N2Fixation: A Case Study of Iron-Nitrogen-Carbon (Fe@ NC) Systems. *Catalysis Today* 2019.

104. Li H, Zhao Z, Cai Q, Yin L, Zhao J. Nitrogen electroreduction performance of transition metal dimers embedded into N-doped graphene: a theoretical prediction. *Journal of Materials Chemistry A* 2020, **8**(8)**:** 4533-4543.

105. Ling C, Ouyang Y, Li Q, Bai X, Mao X, Du A, *et al.* A General two-step strategy–based high-throughput screening of single atom catalysts for nitrogen fixation. *Small Methods* 2019, **3**(9)**:** 1800376.

106. Jiao D, Liu Y, Cai Q, Zhao J. Coordination tunes the activity and selectivity of the nitrogen reduction reaction on single-atom iron catalysts: a computational study. *Journal of Materials Chemistry A* 2021, **9**(2)**:** 1240-1251.

107. Ye K, Hu M, Li Q-K, Luo Y, Jiang J, Zhang G. Cooperative Single-Atom Active Centers for Attenuating the Linear Scaling Effect in the Nitrogen Reduction Reaction. *The Journal of Physical Chemistry Letters* 2021, **12**(22)**:** 5233-5240.

108. Born M, Oppenheimer R. Zur quantentheorie der molekeln. *Annalen der physik* 1927, **389**(20)**:** 457-484.

109. Hohenberg P, Kohn W. Inhomogeneous electron gas. *Physical Review* 1964, **136**(3B)**:** B864-B871.

110. Kohn W, Sham LJ. Self-consistent equations including exchange and correlation effects. *Physical Review* 1965, **140**(4A)**:** A1133-A1138.

111. Parr RG, Yang W. *Density-functional theory of atoms and molecules*, vol. 16. Oxford university press, 1989.

112. Ceperley DM, Alder BJ. Ground state of the electron gas by a stochastic method. *Physical review letters* 1980, **45**(7)**:** 566.

113. Jones RO, Gunnarsson O. The density functional formalism, its applications and prospects. *Reviews of Modern Physics* 1989, **61**(3)**:** 689.

114. Perdew JP, Zunger A. Self-interaction correction to density-functional approximations for many-electron systems. *Physical Review B* 1981, **23**(10)**:** 5048.

115. Perdew JP, Chevary J, Vosko S, Jackson KA, Pederson MR, Singh D, *et al.* Atoms, molecules, solids, and surfaces: Applications of the generalized gradient approximation for exchange and correlation. *Physical Review B* 1992, **46**(11)**:** 6671.

116. Becke AD. Density-functional exchange-energy approximation with correct asymptotic behavior. *Physical review A* 1988, **38**(6)**:** 3098.

117. Lee C, Yang W, Parr RG. Development of the Colle-Salvetti correlation-energy formula into a functional of the electron density. *Physical review B* 1988, **37**(2)**:** 785.

118. Perdew JP, Wang Y. Accurate and simple analytic representation of the electron-gas correlation energy. *Physical review B* 1992, **45**(23)**:** 13244.

119. Perdew JP, Burke K, Ernzerhof M. Generalized gradient approximation made simple. *Physical Review Letters* 1996, **77**(18)**:** 3865.

120. Perdew JP, Ruzsinszky A, Csonka GI, Vydrov OA, Scuseria GE, Constantin LA, *et al.* Restoring the density-gradient expansion for exchange in solids and surfaces. *Physical review letters* 2008, **100**(13)**:** 136406.

121. Kresse G, Hafner J. Ab initio molecular-dynamics simulation of the liquid-metal–amorphous-semiconductor transition in germanium. *Physical Review B* 1994, **49**(20)**:** 14251.

122. Kresse G, Furthmüller J. Efficient iterative schemes for ab initio total-energy calculations using a plane-wave basis set. *Physical Review B* 1996, **54**(16)**:** 11169.

123. Kresse G, Furthmüller J. Efficiency of ab-initio total energy calculations for metals and semiconductors using a plane-wave basis set. *Computational Materials Science* 1996, **6**(1)**:** 15-50.

124. Kresse G, Joubert D. From ultrasoft pseudopotentials to the projector augmented-wave method. *Physical Review B* 1999, **59**(3)**:** 1758.

125. Blöchl PE. Projector augmented-wave method. *Physical Review B* 1994, **50**(24)**:** 17953.

126. Tkatchenko A, Scheffler M. Accurate molecular van der Waals interactions from ground-state electron density and free-atom reference data. *Physical Review Letters* 2009, **102**(7)**:** 073005.

127. Bučko T, Lebègue S, Hafner J, Angyan JG. Tkatchenko-Scheffler van der Waals correction method with and without self-consistent screening applied to solids. *Physical Review B* 2013, **87**(6)**:** 064110.

128. Monkhorst HJ, Pack JD. Special points for Brillouin-zone integrations. *Physical Review B* 1976, **13**(12)**:** 5188.

129. Nørskov JK, Rossmeisl J, Logadottir A, Lindqvist L, Kitchin JR, Bligaard T*, et al.* Origin of the overpotential for oxygen reduction at a fuel-cell cathode. *The Journal of Physical Chemistry B* 2004, **108**(46)**:** 17886-17892.

130. Burton J. Vacancy-formation entropy in cubic metals. *Physical Review B* 1972, **5**(8)**:** 2948.

131. Hatcher R, Zeller R, Dederichs P. Formation entropy and the diffusion constant for vacancies in Cu and α-Fe. *Physical Review B* 1979, **19**(10)**:** 5083.

132. Allison T. JANAF Thermochemical Tables, NIST Standard Reference Database 13. National Institute of Standards and Technology; 1996.

133. Benedikt U, Schneider WB, Auer AA. Modelling electrified interfaces in quantum chemistry: constant charge vs. constant potential. *Physical Chemistry Chemical Physics* 2013, **15**(8)**:** 2712-2724.

134. Goodpaster JD, Bell AT, Head-Gordon M. Identification of possible pathways for C–C bond formation during electrochemical reduction of CO2: new theoretical insights from an improved electrochemical model. *The journal of physical chemistry letters* 2016, **7**(8)**:** 1471-1477.

135. Xiao H, Cheng T, Goddard III WA, Sundararaman R. Mechanistic explanation of the pH dependence and onset potentials for hydrocarbon products from electrochemical reduction of CO on Cu (111). *Journal of the American Chemical Society* 2016, **138**(2)**:** 483-486.

136. Xiao H, Cheng T, Goddard III WA. Atomistic mechanisms underlying selectivities in C1 and C2 products from electrochemical reduction of CO on Cu (111). *Journal of the American Chemical Society* 2017, **139**(1)**:** 130-136.

137. Sundararaman R, Goddard III WA, Arias TA. Grand canonical electronic density-functional theory: Algorithms and applications to electrochemistry. *The Journal of chemical physics* 2017, **146**(11)**:** 114104.

138. Steinmann SN, Sautet P. Assessing a first-principles model of an electrochemical interface by comparison with experiment. *The Journal of Physical Chemistry C* 2016, **120**(10)**:** 5619-5623.

139. Luo J-H, Hong Z-S, Chao T-H, Cheng M-J. Quantum Mechanical Screening of Metal-N4-Functionalized Graphenes for Electrochemical Anodic Oxidation of Light Alkanes to Oxygenates. *The Journal of Physical Chemistry C* 2019, **123**(31)**:** 19033-19044.

140. Chang K, Zhang H, Chen JG, Lu Q, Cheng M-J. Constant electrode potential quantum mechanical study of CO2 electrochemical reduction catalyzed by N-doped graphene. *Acs Catalysis* 2019, **9**(9)**:** 8197-8207.

141. Mathew K, Sundararaman R, Letchworth-Weaver K, Arias T, Hennig RG. Implicit solvation model for density-functional study of nanocrystal surfaces and reaction pathways. *The Journal of chemical physics* 2014, **140**(8)**:** 084106.

142. Mathew K, Kolluru VC, Mula S, Steinmann SN, Hennig RG. Implicit self-consistent electrolyte model in plane-wave density-functional theory. *The Journal of chemical physics* 2019, **151**(23)**:** 234101.

143. Chen M-F, Chao T-H, Shen M-H, Lu Q, Cheng M-J. Evaluating Potential Catalytic Active Sites on Nitrogen-Doped Graphene for the Oxygen Reduction Reaction: An Approach Based on Constant Electrode Potential Density Functional Theory Calculations. *The Journal of Physical Chemistry C* 2020, **124**(47)**:** 25675-25685.

144. Zhao X, Yin F, Liu N, Li G, Fan T, Chen B. Highly efficient metal–organic-framework catalysts for electrochemical synthesis of ammonia from N_2 (air) and water at low temperature and ambient pressure. *Journal of Materials Science* 2017, **52**(17)**:** 10175-10185.

145. Qin Q, Heil T, Antonietti M, Oschatz M. Single-Site Gold Catalysts on Hierarchical N-Doped Porous Noble Carbon for Enhanced Electrochemical Reduction of Nitrogen. *Small Methods* 2018, **2**(12)**:** 1800202.

146. Fei H, Dong J, Feng Y, Allen CS, Wan C, Volosskiy B, *et al.* General synthesis and definitive structural identification of MN4C4 single-atom catalysts with tunable electrocatalytic activities. *Nature Catalysis* 2018, **1**(1)**:** 63-72.

147. Xu H, Cheng D, Cao D, Zeng XC. A universal principle for a rational design of single-atom electrocatalysts. *Nature Catalysis* 2018, **1**(5)**:** 339-348.

148. Wang Y, Su H, He Y, Li L, Zhu S, Shen H, *et al.* Advanced Electrocatalysts with Single-Metal-Atom Active Sites. *Chemical Reviews* 2020, **120**(21)**:** 12217-12314.

149. Gao Y, Han Z, Hong S, Wu T, Li X, Qiu J, *et al.* ZIF-67-Derived Cobalt/Nitrogen-Doped Carbon Composites for Efficient Electrocatalytic N2 Reduction. *ACS Applied Energy Materials* 2019, **2**(8)**:** 6071-6077.

150. Lü F, Zhao S, Guo R, He J, Peng X, Bao H, *et al.* Nitrogen-coordinated single Fe sites for efficient electrocatalytic N_2 fixation in neutral media. *Nano Energy* 2019, **61:** 420-427.

151. Guo X, Gu J, Hu X, Zhang S, Chen Z, Huang S. Coordination tailoring towards efficient single-atom catalysts for N_2 fixation: A case study of iron-nitrogen-carbon (Fe@N-C) systems. *Catalysis Today* 2020, **350:** 91-99.

152. Charreteur F, Jaouen F, Ruggeri S, Dodelet J-P. Fe/N/C non-precious catalysts for PEM fuel cells: Influence of the structural parameters of pristine commercial carbon blacks on their activity for oxygen reduction. *Electrochimica acta* 2008, **53**(6)**:** 2925-2938.

153. Pan F, Zhang H, Liu K, Cullen DA, More KL, Wang M, *et al.* Unveiling Active Sites of CO2 Reduction on Nitrogen Coordinated and Atomically Dispersed Iron and Cobalt Catalysts. *ACS Catalysis* 2018.

154. Pan F, Zhang H, Liu Z, Cullen D, Liu K, More K, *et al.* Atomic-level active sites of efficient imidazolate framework-derived nickel catalysts for CO 2 reduction. *Journal of Materials Chemistry A* 2019, **7**(46)**:** 26231-26237.

155. Shen H, Gracia-Espino E, Ma J, Tang H, Mamat X, Wagberg T, *et al.* Atomically FeN2 moieties dispersed on mesoporous carbon: A new atomic catalyst for efficient oxygen reduction catalysis. *Nano Energy* 2017, **35:** 9-16.

156. Wang X, Chen Z, Zhao X, Yao T, Chen W, You R, *et al.* Regulation of Coordination Number over Single Co Sites: Triggering the Efficient Electroreduction of CO2. *Angewandte Chemie International Edition* 2018, **57**(7)**:** 1944-1948.

157. Gong Y-N, Jiao L, Qian Y, Pan C-Y, Zheng L, Cai X, *et al.* Regulating the Coordination Environment of MOF-Templated Single-Atom Nickel Electrocatalysts for Boosting CO2 Reduction. *Angewandte Chemie International Edition* 2020, **59**(7)**:** 2705-2709.

158. He Y, Li Y, Zhang J, Wang S, Huang D, Yang G, *et al.* Low-temperature strategy toward Ni-NC@Ni core-shell nanostructure with Single-Ni sites for efficient CO2 electroreduction. *Nano Energy* 2020, **77:** 105010.

159. Shan W, Wang G. Enhancing Catalytic Properties of Iron-and Nitrogen-Doped Carbon for Nitrogen Reduction through Structural Distortion: A Density Functional Theory Study. *The Journal of Physical Chemistry C* 2021, **125**(29)**:** 16004-16012.

160. Zhang H, Hwang S, Wang M, Feng Z, Karakalos S, Luo L*, et al.* Single Atomic Iron Catalysts for Oxygen Reduction in Acidic Media: Particle Size Control and Thermal Activation. *Journal of the American Chemical Society* 2017, **139**(40)**:** 14143-14149.

161. Zhang H, Chung HT, Cullen DA, Wagner S, Kramm UI, More KL*, et al.* High-performance fuel cell cathodes exclusively containing atomically dispersed iron active sites. *Energy & Environmental Science* 2019, **12**(8)**:** 2548-2558.

162. Kramm UI, Herranz J, Larouche N, Arruda TM, Lefèvre M, Jaouen F*, et al.* Structure of the catalytic sites in Fe/N/C-catalysts for O2-reduction in PEM fuel cells. *Physical Chemistry Chemical Physics* 2012, **14**(33)**:** 11673-11688.

163. Légaré M-A, Bélanger-Chabot G, Dewhurst RD, Welz E, Krummenacher I, Engels B*, et al.* Nitrogen fixation and reduction at boron. *Science* 2018, **359**(6378)**:** 896-900.

164. Yin H, Dou Y, Chen S, Zhu Z, Liu P, Zhao H. 2D Electrocatalysts for Converting Earth-Abundant Simple Molecules into Value-Added Commodity Chemicals: Recent Progress and Perspectives. *Advanced Materials* 2019.

165. Jiao Y, Zheng Y, Davey K, Qiao S-Z. Activity origin and catalyst design principles for electrocatalytic hydrogen evolution on heteroatom-doped graphene. *Nature Energy* 2016, **1**(10)**:** 16130.

166. Zhang L-H, Yu F, Shiju NR. Carbon-Based Catalysts for Selective Electrochemical Nitrogen-to-Ammonia Conversion. *ACS Sustainable Chemistry & Engineering* 2021.

167. Liu C, Li Q, Wu C, Zhang J, Jin Y, MacFarlane DR*, et al.* Single-boron catalysts for nitrogen reduction reaction. *Journal of the American Chemical Society* 2019, **141**(7)**:** 2884-2888.

168. Li Q, He L, Sun C, Zhang X. Computational study of MoN_2 monolayer as electrochemical catalysts for nitrogen reduction. *The Journal of Physical Chemistry C* 2017, **121**(49)**:** 27563-27568.

169. Mounet N, Marzari N. First-principles determination of the structural, vibrational and thermodynamic properties of diamond, graphite, and derivatives. *Physical Review B* 2005, **71**(20)**:** 205214.

170. Bao W, Miao F, Chen Z, Zhang H, Jang W, Dames C*, et al.* Controlled ripple texturing of suspended graphene and ultrathin graphite membranes. *Nature Nanotechnology* 2009, **4**(9)**:** 562.

171. Pozzo M, Alfe D, Lacovig P, Hofmann P, Lizzit S, Baraldi A. Thermal expansion of supported and freestanding graphene: lattice constant versus interatomic distance. *Physical Review Letters* 2011, **106**(13)**:** 135501.

172. Yoon D, Son Y-W, Cheong H. Negative thermal expansion coefficient of graphene measured by Raman spectroscopy. *Nano Letters* 2011, **11**(8)**:** 3227-3231.

173. Li J, Zhang H, Samarakoon W, Shan W, Cullen DA, Karakalos S*, et al.* Thermally driven structure and performance evolution of atomically dispersed FeN_4 sites for oxygen reduction. *Angewandte Chemie International Edition* 2019, **58**(52)**:** 18971-18980.

174. Mohd Adli N, Shan W, Hwang S, Samarakoon W, Karakalos S, Li Y*, et al.* Engineering Atomically Dispersed FeN_4 Active Sites for CO_2 Electroreduction. *Angewandte Chemie International Edition* 2021, **133**(2)**:** 1035-1045.

175. Zhang R, Jiao L, Yang W, Wan G, Jiang H-L. Single-atom catalysts templated by metal–organic frameworks for electrochemical nitrogen reduction. *Journal of Materials Chemistry A* 2019, **7**(46)**:** 26371-26377.

176. Ma Z, Cui Z, Xiao C, Dai W, Lv Y, Li Q*, et al.* Theoretical screening of efficient single-atom catalysts for nitrogen fixation based on a defective BN monolayer. *Nanoscale* 2020, **12**(3)**:** 1541-1550.

177. Dronskowski R, Blöchl PE. Crystal orbital Hamilton populations (COHP): energy-resolved visualization of chemical bonding in solids based on density-functional calculations. *The Journal of Physical Chemistry* 1993, **97**(33)**:** 8617-8624.

178. Deringer VL, Tchougréeff AL, Dronskowski R. Crystal orbital Hamilton population (COHP) analysis as projected from plane-wave basis sets. *The Journal of Physical Chemistry A* 2011, **115**(21)**:** 5461-5466.

179. Maintz S, Deringer VL, Tchougréeff AL, Dronskowski R. Analytic projection from plane-wave and PAW wavefunctions and application to chemical-bonding analysis in solids. *Journal of Computational Chemistry* 2013, **34**(29)**:** 2557-2567.

180. Nelson R, Ertural C, George J, Deringer VL, Hautier G, Dronskowski R. LOBSTER: Local orbital projections, atomic charges, and chemical-bonding analysis from projector-augmented-wave-based density-functional theory. *Journal of Computational Chemistry* 2020, **41**(21)**:** 1931-1940.

181. Maintz S, Deringer VL, Tchougréeff AL, Dronskowski R. LOBSTER: A tool to extract chemical bonding from plane-wave based DFT. *Journal of Computational Chemistry* 2016, **37**(11)**:** 1030-1035.

182. Pourbaix M. *Atlas of electrochemical equilibria in aqueous solution*, vol. 307, 1974.

183. Zeng Z, Chan MK, Zhao Z-J, Kubal J, Fan D, Greeley J. Towards first principles-based prediction of highly accurate electrochemical Pourbaix diagrams. *The Journal of Physical Chemistry C* 2015, **119**(32)**:** 18177-18187.

184. Hansen HA, Rossmeisl J, Nørskov JK. Surface Pourbaix diagrams and oxygen reduction activity of Pt, Ag and Ni (111) surfaces studied by DFT. *Physical Chemistry Chemical Physics* 2008, **10**(25)**:** 3722-3730.

185. Persson KA, Waldwick B, Lazic P, Ceder G. Prediction of solid-aqueous equilibria: Scheme to combine first-principles calculations of solids with experimental aqueous states. *Physical Review B* 2012, **85**(23)**:** 235438.

186. Bajdich M, García-Mota M, Vojvodic A, Nørskov JK, Bell AT. Theoretical investigation of the activity of cobalt oxides for the electrochemical oxidation of water. *Journal of the American chemical Society* 2013, **135**(36)**:** 13521-13530.

187. Fazio G, Ferrighi L, Di Valentin C. Boron-doped graphene as active electrocatalyst for oxygen reduction reaction at a fuel-cell cathode. *Journal of catalysis* 2014, **318:** 203-210.

188. Duan Z, Henkelman G. Surface Charge and Electrostatic Spin Crossover Effects in CoN4 Electrocatalysts. *ACS Catalysis* 2020, **10**(20)**:** 12148-12155.

189. Vijay S, Gauthier JA, Heenen HH, Bukas VJ, Kristoffersen HH, Chan K. Dipole-field interactions determine the CO2 reduction activity of 2D Fe-NC single atom catalysts. *ACS Catalysis* 2020.